Dissertation Submitted to

The Combined Faculties for the Natural Sciences and for Mathematics

Of the Ruperto-Carola University of Heidelberg, Germany

For the degree of

Doctor of Natural Sciences

Presented by

MSc. Noha Waly

born in Cairo, Egypt

Oral examination: 11. 02. 2011

Optimization of core-shell nanoparticle layers for optical biosensing

Prof. (apl.)Dr. Reiner Dahint
University of Heidelberg

Prof. Dr. Joachim P. Spatz
University of Heidelberg

Acknowledgement

First of all, I would like to express my deepest gratitude and admiration to my supervisor, Prof. Dr. Reiner Dahint, for his excellent guidance, patience and his encouragement in helping me to accomplish this research. Without his valuable discussions and objective criticism I would not have been able to complete this task.

I greatly appreciate Prof. Dr. Joachim Spatz for accepting my thesis and being one of the examiners, and here I also need to highlight Prof. Dr. Peter Hess´s support and help which will never be forgotten.

I would like to thank Herrn Georg Albert for his efforts in preparing the substrates needed for the experiments. Without his sincere engagement this work would have not gone one step forward.

Special gratitude to all my colleagues in our group, they were very supportive, cooperative and helpful. Fanny, Andrea, Haci and Anna were very cooperative, friendly and I will always remember their productive help.

I want to thank from the bottom of my heart, both of my parents, my sister and brother for their prayers. I am especially and deeply grateful to my husband and daughter for their patience and encouragement, to whom I dedicate my future to.

Finally, with all respect, I believe it is obligatory to mention that I am in debt with gratitude to my country Egypt for all its support that it gave me.

Abstract

In this work we constructed and optimized a label-free biosensor which is based on a combination of surface plasmon resonance and reflectometric interference. Both techniques have been utilized for label-free biosensing for more than two decades as the corresponding extinction spectra undergo a wavelength shift upon molecule binding.

In the present study it has been demonstrated that a combination of both effects can significantly improve sensitivity. The developed biosensor consists of dielectric spheres of 400-500 nm diameters, deposited on a flat solid substrate and coated with gold nanoparticles. The spectrum of such structure exhibits multiple extinction peaks resulting from the interference of beams reflected between the flat substrate and the surface of the dielectric spheres. These peaks are enhanced by the presence of gold on top of the spheres due to coherent oscillation of the free electrons of the metal, i.e. plasmon excitation. In a systematic study, the optical properties of the sensing element have been optimized, and its sensitivity towards molecule binding has been tested by fibrinogen adsorption for the different sensor geometries developed. In the wavelength regime from 400-900 nm two dominant peaks are observed. It was shown, that the sensitivity of the peak between 600 and 900 nm exhibits the higher sensitivity compared to the peak between 400 and 600 nm.

Different deposition techniques for the dielectric spheres have been tested to find the most reproducible one with closed packed coverage. Here, a technique, in which the dielectric spheres are first floated on a liquid subphase and then transferred to the solid support in a Langmuir-Blodgett like approach, yielded improved lateral homogeneity of the optical response and higher sensitivity than film of randomly deposited spheres.

Two kinds of metallization have been studied (i) deposition of metal nanoparticles from solution (seeding) followed by an enlargement of the nanoparticles (plating), and (ii) evaporation of a metal thin film on the top of the spheres by physical vapor deposition (PVD). The resulting optical response and morphology were characterized by UV-Vis spectroscopy and scanning electron microscopy (SEM).

For gold metal deposition from gold solution we found out that the sensitivity decreases with increasing plating time and is highest for purely seeded surfaces.

For gold films deposited by PVD we identified an optimum gold thin film thickness of 50 nm to provide enhanced sensitivity. Effects of metal composition (gold and silver) on the optical properties and sensitivity have been investigated, showing significantly higher sensitivity for silver than for gold nanoparticle coatings of the same coverage in range from 400-600 nm.

We also observed that the sensitivity is improved by the presence of a dielectric layer of silicon oxide/dioxide in between the substrate and the gold-coated spheres. Independent of the type of substrate used (i.e. metalized or not), an optimum layer thickness of 40 nm was found.

As an application in the field of biomedical analysis, we investigated the performance of the optimized biosensor in the label-free detection of antibody–antigen reactions.

Zusammenfassung

In dieser Arbeit wird ein Label-freier Biosensor, der auf einer Kombination von Oberflächen-Plasmon-Resonanz und Interferenz auf reflektometrischer Basis aufgebaut ist. Beide Techniken werden für Label-freie Biosensorik seit mehr als zwei Jahrzehnte genutzt weil sich die entsprechenden Exstinktionsspektren einer Wellenlängenverschiebung aufgrund molekularer Bindungen unterziehen.

In der vorliegenden Studie wurde nachgewiesen, dass eine Kombination beider Effekte deutlich die Empfindlichkeit verbessern kann. Die entwickelten Biosensor besteht aus dielektrischen Sphären von 400-500 nm Durchmesser, abgeschieden auf einem flachen und festen Substrat beschichtet mit Gold-Nanopartikeln. Das Spektrum solcher Struktur weist mehrere Exstinktionsspitzen auf, die aus der Interferenz von Lichtstrahlen zwischen dem flachen Substrat und der Oberfläche der dielektrischen Kugeln resultieren. Diese Spitzen werden durch das Vorhandensein von Gold auf den Sphären verbessert, indem kohärente Schwingung der freien Elektronen des Metalls, das heißt Plasmonenanregung, entsteht. In einer systematischen Studie wurden die optischen Eigenschaften des Sensors optimiert, und ihre Empfindlichkeit gegenüber Molekülbindung wurde durch Fibrinogen Adsorption für Sensoren unterschiedlicher Geometrie getestet. Im Wellenlängenbereich von 400 bis 900 nm wurden zwei dominante Peaks beobachtet.

Es wurde gezeigt, dass die Empfindlichkeit der Spitze zwischen 600 und 900 nm die höhere Empfindlichkeit im Verglich zum Peak zwischen 400 und 600 nm zeigt.
Verschiedene Techniken für die Abscheidung dielektrischer Kugeln wurden getestet, um die am besten reproduzierbare geschlossene Oberflächenbedeckung zu finden.

Hier wird eine Technik verwendet, bei der die dielektrische Kugeln zunächst auf einer Flüssigkeit aufschwimmen werden und dann an den festen Träger wie in einem Langmuir-Blodgett Ansatz übertragen werden. Es ergab sich eine verbesserte laterale Homogenität der optischen Reaktion und höhere Empfindlichkeit als bei einem Film zufällig hinterlegter Sphären.
Zwei Arten von Metallisierung wurden untersucht (i) Auftragung von Metall-Nanopartikeln aus der Lösung (Impfung) gefolgt von einer Vergrößerung der Nanopartikel (Beschichtung), und (ii) Verdampfung eines Metall-Dünn Film auf der Spitze der Kugeln durch physikalische Gasphasenabscheidung (PVD). Die daraus resultierende optische Antwort und Morphologie wurden durch UV-Vis-Spektroskopie und Rasterelektronenmikroskopie (REM) charakterisiert.

Für Gold Metallabscheidung aus einer Goldlösung fanden wir heraus, dass die Empfindlichkeit mit zunehmender Plating-Zeit abnimmt und am höchsten für nur geimpfte Oberflächen. Für Gold abgeschiedenen Schichten durch PVD identifizierten wir für die optimale Gold Dünnschicht Dicke von 50 nm die höchste Empfindlichkeit.

Auswirkungen der Metall-Zusammensetzung (Gold und Silber) sind auf die optischen Eigenschaften und die Empfindlichkeit untersucht worden und zeigten deutlich höhere Sensitivität für Silber als für Gold-Nanopartikel Beschichtungen der gleichen Bedeckung im Bereich von 400-600 nm.
Wir beobachteten auch, dass die Empfindlichkeit durch die Anwesenheit von einer dielektrischen Schicht zwischen dem Substrat und der Gold-beschichteten Kugeln verbessert wird. Unabhängig von der Art des verwendeten Substrats (dh metallisierten oder nicht), eine optimale Schichtdicke von 40 nm gefunden wurde.

Als eine Anwendung im Bereich der biomedizinischen Analyse untersuchten wir die Leistungsfähigkeit des optimierten Biosensors im Label-freien Nachweis von Antikörper-Antigen-Reaktion.

Contents

Chapter 1

1- Introduction

The past decade has seen significant advances in the synthesis and fabrication of sensitive label-free biosensors which are highly desired for applications in high-throughput drug discovery and disease diagnostics [1]. A variety of label-free optical transduction methods have been developed, which fall primarily into two categories: optical interferometric methods (such as grating couplers [1-3], interferometers [4], and evanescent wave devices [5],[6]) and surface plasmon methods (involving thin metal layers such as gold and silver films [7],[8] or colloids [9]).

In general, optical biosensors are designed to translate changes in the propagation speed of light through a medium that contains biological material into a quantifiable signal proportional to the amount of biological material present on the sensor surface. The design goal for all optical biosensors is to provide a transducer with some externally measurable characteristic that is modified by changes in dielectric permittivity on its surface [10]. Optical biosensors are constructed from various types of optical resonators in which the transducer surface is illuminated with a broad range of wavelengths (or incident angles) and only a narrow range of incident wavelengths (or angles) is reflected back or transmitted through.

For these types of resonant optical biosensors, the detection instrument measures changes of the optical properties in the range of wavelengths that occur as a result of biomolecular binding on the resonator surface.

Over the last two decades, surface plasmon resonance (SPR) sensor instrumentation has made great advances and become a central tool for the study of biomolecular interactions and is widely applied in the detection of chemical and biological analytes [11].

In order to achieve high performance, numerous SPR sensor platforms and data processing methods have been developed [12].

In particular localized surface plasmon resonance (LSPR) of noble metal nanoparticles is one of the most interesting label-free optical biosensors.

It is based on the dependence of the scattering/absorption properties of the metal nanostructures on changes in the dielectric properties of the local environment of the nanoparticles including substrate, solvent, and adsorbates.

This dependence arises from the surface resonance condition $\varepsilon = k\varepsilon_m$, where k is a shape factor and equal to 2 in case of a sphere, as we will see later. An increase in the dielectric constant ε_m (or refractive index $n=\varepsilon_m^{\frac{1}{2}}$) of the surrounding medium is therefore reflected as a red shift in the LSPR band. Thus, by following the shift in the LSPR wavelength in response to adsorbate-induced changes in the local dielectric environment of the nanoparticle, a nanoscale chemical or biosensor can be developed. Thus, for high sensitivity we need large changes in the LSPR wavelength in response to relatively small changes in the medium refractive index.

Many theoretical and experimental studies [13-14] have been made on metal nanoparticles with different geometry to find the best configuration to enhance the sensitivity, which make the plasmon resonance response an attractive area of research.

At the same time spectral reflectometric interference spectroscopy (RIfs) has been used for direct optical detection of biomolecular interactions [4, 15]. Here, the spectral positions of the Fabry-Perot fringes shift to longer wavelengths as a function of the refractive index of the material filling the pores of porous silicon [16-17]. The RIfS transducer measures changes in the optical thickness (product of the thickness d and refractive index n) of a thin film. By immobilizing small organic probe molecules on the transducer surface specific recognition layer is obtained. The specific binding of an analyte with binding sites for the immobilized probe molecule leads to a localized and discrete change in optical thickness [18-19].

RIfs are based on the interference of light beams, which are reflected at interfaces with different refractive indices.

The interference pattern is related to the optical thickness this term should be defined of the film [20] by the equation

$$m\Lambda = 2nd \qquad 1.1$$

m is the spectral order and Λ the wavelength of light, d is the thickness of the film.

Binding of analyte to the surface results in a change in the refractive index n of the layer medium and can be detected as shift in the interference pattern.

The basic design of the sensing element is shown in the fig 1.1. RIfS, like surface plasmon resonance, is a label-free technique, which allows the time-resolved observation of interactions among the binding partners without the use of fluorescence or radioactive labels.

a b

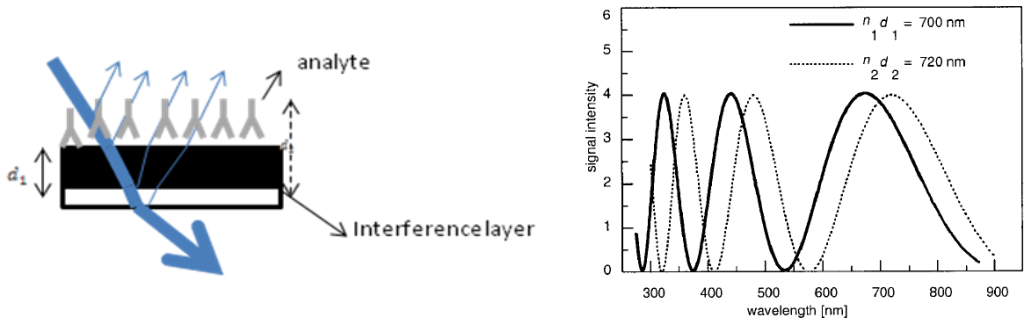

figure 1. 1*a) Schemeof the biosensor and the detection method: white light is reflected from the different interfaces b) The reflected beams create an interference pattern from which the optical thickness of the thin bioorganic layer can be determined. The effective optical thickness before and after binding is* $(n_1.d_1)$ *and* $(n_2.d_2)$*, respectively [21].*

In our work, we developed an advanced set-up which utilizes the coupling of localized surface plasmons with the interference bands of thin multilayer films [19, 22]. For optimum layer thickness, coupling is maximized, resulting in enhanced sensitivity towards molecule adsorption. [22]. Instead of using porous materials [23-24] we constructed a hexagonal monolayer of silica (or polystyrene) spheres closely packed on a substrate so that the distance between the spheres is small enough to avoid light-scattering effects and to increase the sharpness of the reflected beam.

The diameter of the spheres is close to the wavelength of light, as such thickness satisfies the coherence condition for the reflected beams to interfere [25]. Gold nanoparticles of random shape were deposited on the monolayer of spheres. Coupling of the plasmon bands with interference bands enhanced the changes in the wavelength of the localized surface plasmon bands if the surface is exposed to media of different refractive indices, leading to increased sensor sensitivity.

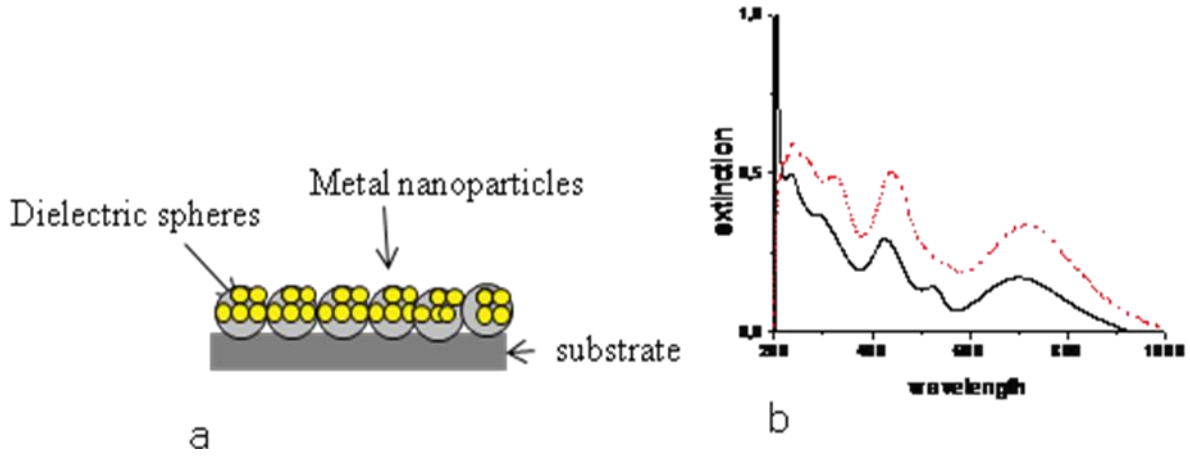

Figure 1. 2 a- Structure of our sensor: silica spheres are deposited on a silicon wafer (100) and covered with gold nanoparticles of 3-5 nanometer size b- UV spectra of the dielectric spheres before (solid black line) and after (red dots) gold deposition

The spectrum of such structures is the result of the interference of beams reflected from the dielectric sphere. The interference patterns are enhanced due to the presence of gold nanoparticles on the top of the spheres due to coherent oscillation of the free electrons: this increases the intensity of the peaks as well as narrows them [23].

Fig 1.2 b shows the UV-Vis spectra of the sensor in comparison to the case of dielectric spheres without gold nanoparticles on top. While in the latter case the peaks are broad and more rounded, the metal-coated substrate shows a strong coupling between LSPR and interference bands which results in an optical pattern that yields high sensitivity to adsorption of analytes and can be utilized as a biosensor.

In addition to the band coupling effect, the structure of two-dimensional hexagonally close-packed spheres bearing nearly half- covered metal shells with nanoscale gaps in between provides significant enhancement to the electric field [26-28].

The expulsion of the electric field from the interior of the nanoparticles gives rise to intense field enhancement in the junction between the core-shell nanoparticles at such long wavelength. From fig 1.2 we can identify multiple peaks from which the two at the highest wavelengths can be used for the detection of biological species [19, 29-31] at shorter and longer wavelength. However, we notice in case of gold-coated spheres that the sensitivity of the peak at the longest wavelength is always higher compared to that of the peak at shorter wavelength. This is expected due to the increase in the negativity of the real part of the dielectric constant at such long wavelengths.

The aim of this thesis is to develop a biosensor and to obtain an optimum condition with our system for high sensitivity as we define the sensitivity as the amount of shift occur in the peaks after changing the medium refractive index by an analyte.

First we optimize the coverage of the dielectric spheres to improve the reproducibility of the samples then we study the effect of increasing the coverage of the gold nanoparticles on the dielectric spheres on the spectrum and on the sensitivity to obtain the optimum coverage of the gold nanoparticles. We also study the effect of the composition of the metal as we replace the gold nanoparticles with silver with approximately the same coverage and compare between them.

We introduced a dielectric layer in between the core-shell nanoparticles and the substrate for two reasons: first to improve the reflectivity of the substrate (reflective coating), and second to reduce the effect of the substrate on the gold nanoparticles that deposit in between the pores of spheres which we believe it could decrease the sensitivity as reported in [32].

We also studied the effect of depositing a thin film of gold on the spheres instead of gold nanoparticles to distinguish between surface plasmon resonance and localized surface plasmon resonance and to study the effect of roughness coverage on the optical properties and the sensitivity of the probes.

We also examined the reflection spectra of plane dielectric thin films coated with gold nanoparticles (with the same coverage) of thickness close to the thickness of the dielectric spheres instead of the dielectric spheres to compare the position of resonance peaks and the sensitivity of the response. As an application for our surface biosensor we study the antibody-antigen interaction in real-time.

In all cases the reflection spectra is a result of the coupling between the surface plasmon (or localized surface plasmon) and the interference pattern generated by multiple reflection in thin film structures (dielectric spheres).

Despite the fact that there is a lack of theoretical understanding of such combination between the interferometric sensor and the plasmonic nanosensor, which is provided by the nanoparticle shell in our case, the overall features of such spectra can be understood from the complex Fresnel equations for reflection in thin film structures and the effective medium approach for the gold nanoparticles on the core surface.

The chapters of the thesis are arranged in the following way: **Chapter 2 discusses** fundamentals like reflection and transmission of light for a single interface and thin films, interference in thin multilayer films, Reflectometric Interference Spectroscopy (RIFS), surface plasmon resonance theory, the dielectric function of metals, metal nanoparticles, coupling between metal nanoparticles, surface plasmon resonance as a biosensing principle, effective medium theories, and describes the apparatus used. **Chapter 3** will include the experimental part describing the preparation steps for formation of hexagonal monolayer of silica/polystyrene spheres, the preparation of the gold colloid and its deposition and growth on the substrates. Moreover, it discusses the characterization methods employed for the samples. **Chapter 4** will include the results and discussion of the work, and

Chapter 5 will contain the conclusions.

Chapter 2

2- Fundamentals

2.1 Reflection and transmission of light at an interface

When a beam of light L (fig. 2.1) is incident at an angle ϑ_i at an interface separating two media of refractive indices $n_1$and n_0, it is refracted at an angle $\vartheta_t$into the second medium as determined by Snell's law $n_o \sin \vartheta_t = n_1 \sin \vartheta_i$.

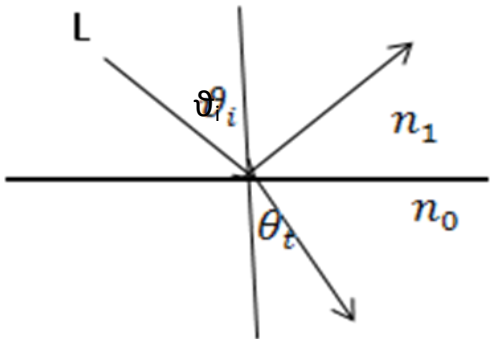

Figure 2. 1 *Reflectionand refraction of light at the interface between two media with refractive indices n_1 and n_0*

The ratios of reflected (r_1) and transmitted (t_1) field amplitudes with respect to the incident beam are given by the Fresnel equations [33],

$$r_{1p} = \frac{E_{r,p}}{E_{i,p}} = \frac{n_0 \cos \vartheta_i - n_1 \cos \vartheta_t}{n_0 \cos \vartheta_i + n_1 \cos \vartheta_t} \qquad 2.1$$

$$r_{1s} = \frac{E_{r,s}}{E_{i,s}} = \frac{n_1 \cos \vartheta_i - n_0 \cos \vartheta_t}{n_1 \cos \theta_i + n_0 \cos \vartheta_t} \qquad 2.2$$

$$t_{1p} = \frac{E_{t,p}}{E_{i,p}} = \frac{2n_1 \cos\vartheta_i}{n_0 \cos\vartheta_i + n_1 \cos\vartheta_t} \qquad 2.3$$

$$t_{1s} = \frac{E_{t,s}}{E_{i,s}} = \frac{2n_1 \cos\vartheta_i}{n_1 \cos\vartheta_i + n_0 \cos\vartheta_t} \qquad 2.4$$

These ratios are called Fresnel reflection and transmission (amplititude) coefficients for polarized components in which the electric vector lies parallel (p) and perpendicular (s) to the plane of incidence, respectively. $E_{i,j}$ denotes the p- or s-component of the E–vector of the incident (i), reflected (r) or transmitted (t) beam.

If no absorption takes place, the reflectivity (or reflectance) R of an interface is defined as the ratio of the reflected energy to the incident energy. Since the reflected and the incident beams are in the same medium,

$$R_{p,s} = \left(r_{p,s}\right)^2 \qquad 2.5$$

Similarly the transmissivity (or transmittance) T – defined as the ratio of the transmitted energy to the incident energy – is

$$T_{p,s} = \frac{n_0 \cos\vartheta_t}{n_1 \cos\vartheta_i}\left(t_{p,s}\right)^2 = 1 - R_{p,s} \qquad 2.6$$

as incident and reflected beam propagate in different media.

For normal incidence, these equations are simplified since the distinction between planes of different polarization vanishes.

For normal incident at an interface with refractive indices n_1 and n_2

$$R_p = R_s = \left(\frac{n_1 - n_0}{n_1 + n_0}\right)^2 \quad \text{and} \quad T_p = T_s = \frac{4n_0 n_1}{(n_1 + n_0)^2} \qquad 2.7$$

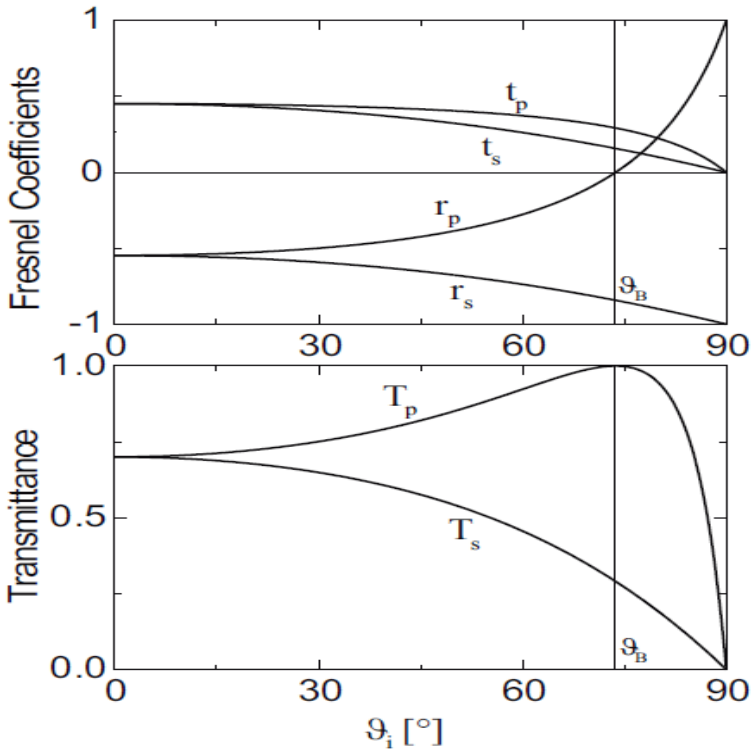

Figure 2.2: Fresnel coefficients (top) and transmittance (bottom) at the vacuum/Si interface (n_2 = 3.4 for p- and s-polarized light with $\tilde{\nu}$ = 2000 cm^{-1} in case of non-absorbing media (A = 0). ϑ_B marks the Brewster angle.

In case of an absorbing substrate, the refractive index n_0 is replaced by the complex quantity $n = n_0 - ik$ where n_0 is the real refractive index and k the absorption coefficient of the material. If absorption takes place, this leads to complex reflection and transmission coefficients in (2.1-2.4), and (2.5) and (2.6) must be modified to

$$R_{p,s} = r_{p,s} r_{p,s}^* \qquad 2.8$$

$$T_{p,s} = \frac{n_0 \cos\vartheta_t}{n_1 \cos\vartheta_i} t_{p,s} t_{p,s}^* = 1 - R_{p,s} - A_{p,s} \qquad 2.9$$

Where $A_{p,s}$ is the absorption coefficient,

Fig 2.2 shows the transmission and reflection coefficients as well as the transmittance of a vacuum/Si interface, assuming the case of no absorption. In case of perpendicular incidence, T_p and $T_s$are identical, as it is not possible to differentiate between p- and s-polarization. While $T_s$decreases monotonically with increasing ϑ_i, $T_p$reaches a maximum before both become zero at ϑ_i = 90°.

At the maximum, T_p= 1. This defines the so-called Brewster angle ϑ_B by

$$\tan \vartheta_B = \frac{n_0}{n_1}$$

2.2 Reflection and transmission by a single film

When a beam of light L is incident on a thin film of index n_2 and thickness d on substrate of index n_0 (fig. 2.3), the amplitude reflection and transmission coefficients are given by

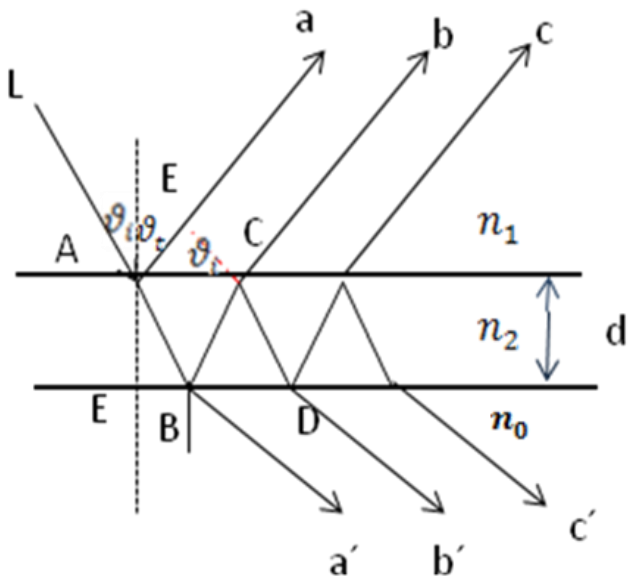

Figure 2.3 Reflection and transmission at the interfaces of a thin film between two semi-infinite media

$$R = \frac{r_2 + r_1 \exp(-2i\delta_1)}{1 + r_2 r_1 \exp(-2i\delta_1)} \qquad 2.10$$

And

$$T = \frac{t_1 t_2 \exp(-i\delta_1)}{1 + r_2 r_1 \exp(-2i\delta_1)} \qquad 2.11$$

Where r_1 r_2 t_1 and t_2 are the Fresnel coefficients at the n_1/n_2 and n_2/n_0 interfaces, $\delta_1 = (2\pi/\Lambda) n_1 d \cos\vartheta_i$ is the phase thickness of the film, and Λ is the wavelength. These equations apply for s and p polarization, the reflectivity and transmissivity are given by

$$\mathbf{R} = RR^* = \frac{r_1^2 + r_2^2 + 2r_1 r_2 \cos 2\delta_1}{1 + r_1^2 r_2^2 + 2r_1 r_2 \cos 2\delta_1} \qquad 2.12$$

$$T = \frac{n_0}{n_2} TT^* = \frac{n_0}{n_2} \frac{t_1^2 t_2^2}{1 + 2r_1 r_2 \cos 2\delta_1 + r_1^2 r_2^2} \qquad 2.13$$

These general expressions can be written in terms of the refractive indices can be found in [34]. The normal incidence reflectance exhibits Oscillatory variation as illustrated in fig 2.4. by the Plot of the Reflectance vs. the film thickness normalized by the wavelength of light.

The reflectance at the position of the maxima and minima is as follows

$$R_{max} = \left(\frac{n_2 - n_0}{n_2 - n_0}\right)^2 \qquad \text{at } \Lambda_{max} = \frac{2n_1 t}{m}$$

and

$$R_{min} = \left(\frac{n_1^2 - n_0 n_2}{n_1^2 + n_0 n_2}\right)^2 \qquad \text{at } \Lambda_{max} = \frac{2n_1 t}{m}$$

m is an integer. Following these equations we can either enhance (reflection coating) or diminish (antireflection coating) R by suitable choice of the film index. Further, the oscillatory behavior of R can be used to monitor the thickness of the film.

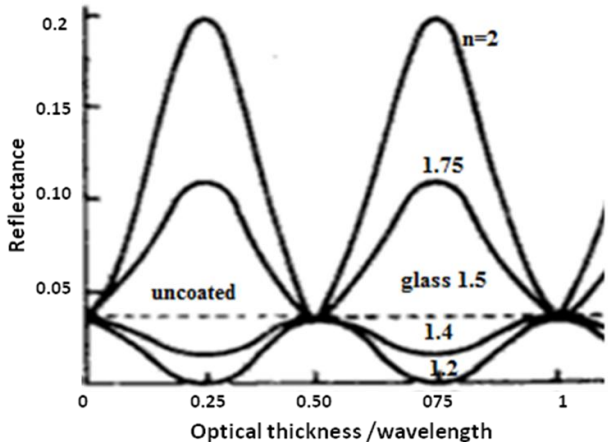

Figure 2.4 Theoretical variation of reflectance R for light incident from air onto a coated glass substrate, as a function of normalized thickness for coatings of various refractive indices.

2.2.1 Interference in thin films

If the thickness of the film is a few hundred nanometers (corresponding to the wavelength of light) these partial beams will interfere if the coherence conditions are fulfilled [33, 35]. As shown in figure 2.3, the incident beam L is split into a finite number of parallel reflected (a, b, c) and refracted (a´, b´, c´) rays. Considering only two reflected beams a and b, the geometrical path difference Δ between them is related to the phase difference by the equation

$$\delta = 2\left(\frac{2\pi}{\lambda}\right)\Delta$$

$$\Delta = 2dn_2 \cos\vartheta_i$$

$$= 2d\sqrt{n_2^2 - n_1^2 \sin^2 \vartheta_t} \qquad 2.\ 14$$

If the optical paths differ by a multiple of λ, the reflected waves add. If the paths cause a phase difference π, reflected waves cancel out**.**

For normal incidence we have for constructive interference

$$\Delta = 2dn_2 \qquad 2.\ 15$$

An interference pattern is generated by the superposition of the two reflected partial beams at parallel interfaces 0.5 to some 10 μm apart within the coherence length of the incident light. This spectral reflection depends on the refractive indices of the film and its surrounding, wavelength, and angle of incidence.

2.3 Reflectometric interference Spectroscopy (RIFS)

Spectral interferometer measures the interference pattern caused by the superposition of two reflected partial beams at parallel interfaces. As shown in figure 2.5, the superposition of these two interfering beams can be influenced by adsorption of molecules at the layer surface. Any difference in the refractive index will introduce additional effects to the Fresnel reflectivity and, thus, affect the intensity of the reflected partial beams.

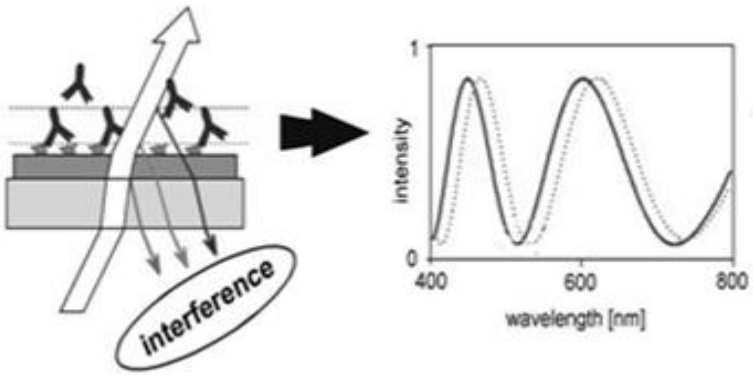

Figure 2.5 Scheme of the RIfS detection principle. The left part shows the superposition of the reflected light beams. The right part shows the corresponding change of the characteristic interference spectrum and the resulting binding curve.

If the refractive index of the adsorbed layer is different from that of the thin film, an additional interface is created, affecting the number and intensity of the reflected partial beams and, thereby, causing a shift in the interference pattern.

For normal incidence, the reflectance *R* is given by: [16, 36-37]

$$R = R_1 + R_2 + 2\sqrt{R_1 R_2}\cos 4\pi nd/\Lambda \qquad 2.16$$

where R_1, R_2, denote the Fresnel reflectance at the two interfaces, d is the physical thickness of the film, *n* its refractive index in the captions of fig. 2.5 you used n_1d_1 and n_2d_2, and Λ the wavelength of incident light.

A typical interference pattern show the modulation of reflectance with cos (d/Λ) given in the figure 2.5 (right). It also shows the change of the characteristic interference spectrum upon molecule binding. [37]

The optical thickness (nd) can be determined from the position of an extremum with a given order value *m* by

$$2nd = m\Lambda \qquad 2.17$$

RIfS uses the change in the optical properties in or at the top layer of a given layer system as detection principle **(**Fig 2.5). The binding of an analyte molecule or particle to the sensor surface causes a shift of the interference pattern in the wavelength domain.

2.4 Reflectometric Interference Spectroscopy (RIFS) as biosensor

Since the interferometric signal is obtained by interference of multiple reflected partial beams, it contains information about the thickness and refractive index of the thin layer. However, monochromatic measurements are unable to discriminate surface from volume effects or to obtain absolute values of optical path lengths. This is due to the fact that the refractive index is a volume-determined value influenced by pure volume changes as well as by changes in sample structure or interaction with molecules intruded into the film [16].

To overcome this principle disadvantage the interferences of the reflected intensities are measured at many wavelengths simultaneously. With m_1 being the order of wavelength Λ_1 can be calculated by

$$m_1 = \frac{\Lambda_2}{\Lambda_1 - \Lambda_2} \Delta m_{12}$$

Where Λ_1, Λ_2 are the wavelengths at two adjacent maxima, the optical path length *nd* at each extremum can obtained from equation 2.17, Spectral interferometer has been considered an interesting approach to detect sensitively and rapidly any changes of optical path lengths in thin polymer films caused by organic solvent vapors in air or water or by antigen-antibody interaction in immunochemical sensing [4, 15]. This interferometric approach is a direct optical method like surface plasmon resonance [38-39]. For probing surface interactions, the use of spectral interferometer is as advantageous as surface plasmon resonance (SPR). It is able to rapidly monitor any dynamic process, such as adsorption or degradation, at a wide range of biomedical relevant interfaces in real time without the need to label the adsorbate and without the need for complex sample preparation.

However one advantage of RIFS over the surface plasmon resonance method is its resistance to changes in temperature whereas the surface plasmon resonance method is sensitive to temperature variations as the refractive index is affected by changes in temperature: This is due to the fact that the refractive index n is dependent on the density as given by the Clausis-Mossotti equation and the density are dependent on the thermal expansion.

Thus, the refractive index will decrease with increasing temperature. Due to thermal expansion of the layer, the physical thickness d will increase with increasing temperature. These two contrary temperature-dependent effects result in a rather low influence of temperature on the optical thickness (product of refractive index and physical thickness) making refrectometry a suitable tool for sensitivity measurements.

Surface plasmon resonance theory overview

2.5 Surface plasmon polaritons

When light is incident on a smooth metal surface, its interaction with the free electrons of the metal surface generates electromagnetic waves that decay exponentially into the metal. These evanescent waves cannot transmit energy through the medium so that the light is reflected back into the surrounding medium giving the surface its shiny appearance of metal. However under certain circumstances, the light becomes trapped at the surface and generates surface waves known as surface plasmon polaritons

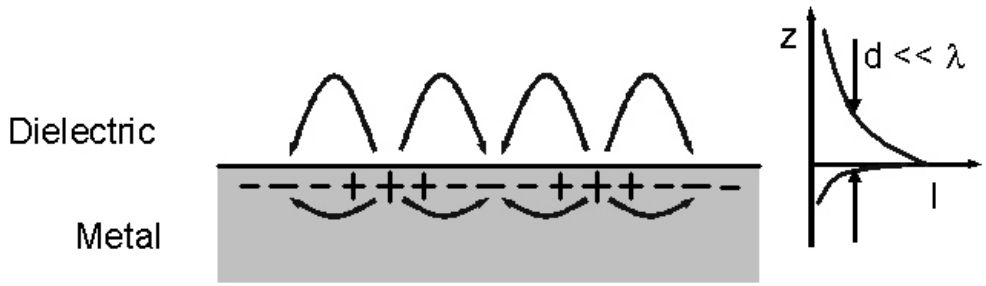

Figure 2.6. The TM-polarized electromagnetic field is coupled to the free electrons of the metal near the surface, and oscillates coherently with the charge density.

Surface plasmon polaritons, or SPPs, are coupled oscillations of free electrons and electromagnetic (EM) waves that are confined near metal-dielectric interfaces and propagate along the boundary between a dielectric and a metal. When propagating along a flat surface as shown in fig. 2.6, the EM field peaks at the interface and decays exponentially into the two adjacent media. SPP is a transverse-magnetic (TM) wave (magnetic vector is parallel to the plane of the interface) and is characterized by its propagation constant and electromagnetic field distribution. The propagation constant,k_x, can be expressed as

$$k_x = \frac{\omega}{c}\sqrt{\frac{\varepsilon_m \varepsilon_d}{\varepsilon_m + \varepsilon_d}} \qquad 2.\ 18$$

where ω is the angular frequency, *c* is the speed of light in vacuum, and ε_d and ε_m are dielectric functions of the metal and the dielectric, respectively [40-41],

The real part of ε_d is negative and its absolute value is smaller than ε_m . At optical wavelengths this condition is fulfilled for several metals of which gold is most commonly employed in SPR biosensors. The real and imaginary parts of the propagation constant describe spatial periodicity and attenuation of an SPP in the direction of propagation, respectively [41]. The optical response of a metal is described by its dielectric function with a negative real part, while that of the dielectric medium is given by a positive permittivity.

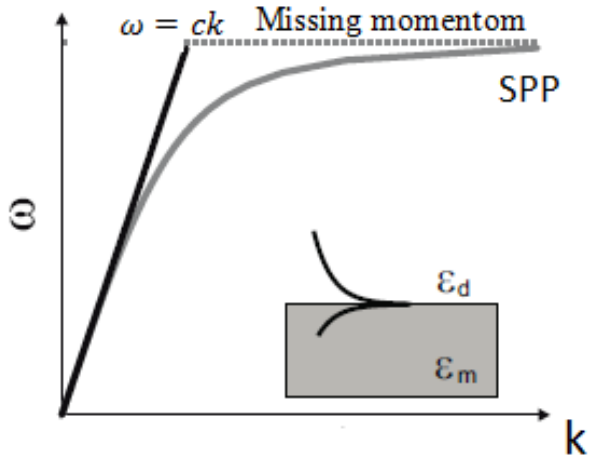

Figure 2.7 Dispersion relation for surface plasmon polaritons propagating at the interface between a dielectric and a metal. The light line in vacuum is drawn in black. Inset: Schematic of the electric field intensity associated with a SPP propagating at the interface between a dielectric and a metal.

Since the SPP modes are nonradiative electromagnetic modes, they cannot be excited directly by incident photons. As displayed in fig. 2.7 the dispersion relation of SPPs do not intersect the light line. Therefore, is not possible to directly excite a SPP by an incident propagating wave without increasing the momentum.

In order to excite them, a prism or a periodic corrugation (grating) is commonly used to provide the missing momentum.

In case of a grating light scattered from a periodic surface gains an extra momentum that alters the momentum matching condition will be described in next paragraph.

The prism coupling approach is not used in this work. A description can be found in [42].

2.5.1 Grating coupling

In order for the photon to couple to a SPP, the wave vector must be increased by interaction of the wave with the surface roughness of the metal film. Most commonly used configurations for SPP excitation by a periodic corrugation are based on diffraction gratings (Fig 2.8). If a light waves incident on a periodically distorted surface of a diffraction grating, a series of reflected waves is generated at different angles [43]. The components of the wave vector of these diffraction-generated light waves parallel to the interface are

$$k_x + mG = k_{xm}$$

where m is the diffraction order (integer), k_x is the component of the wave vector of the incident light along the grating surface, G is the wave vector of the grating, and k_{xm} is the wave vector of the diffracted light wave. In case of a shallow grating, the coupling condition may be expressed as

$$\sqrt{\varepsilon_d}\sin(\theta) + m\frac{\lambda}{\Delta} = \pm Re\left\{\sqrt{\frac{\varepsilon_m \varepsilon_d}{\varepsilon_m + \varepsilon_d}}\right\}$$

2.19

where θ is the angle of incidence of the light, Δ denotes the pitch of the grating ($\Delta = 2\pi/G$), ε_m and ε_d the dielectric function of the dielectric and the metal, respectively, and λ is the free space wavelength.

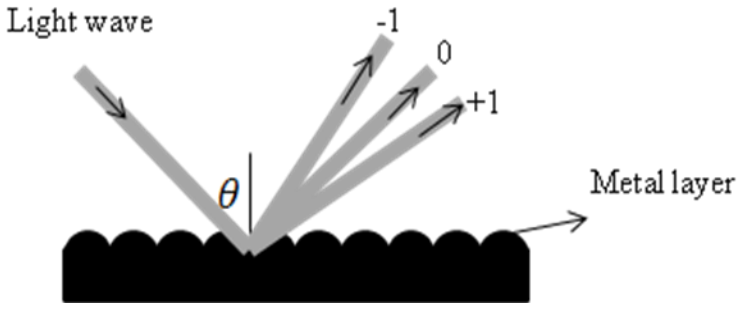

Figure 2. 8 Excitation of a surface plasmon polariton at the surface of a diffraction grating

2.6. Localized surface plasmons

Unlike the extended SPPs on flat interfaces, the localized modes can be excited directly by a plane wave, and they exhibit resonant behavior. These surface plasmon resonances (Localized Surface Plasmon Resonance, LSPR) describe the collective oscillations of free electrons that occur when light is incident on a noble metal nanoparticle or nanoshell. LSPR results in a strong optical extinction which can be tuned throughout the visible and near-infrared wavelengths by adjusting the particle's size and shape. The LSPR spectral extinction peak is sensitive to the surrounding media's refractive index, which allows LSPR-active nanostructures to act as transducers in label-free biosensors. That is, by observing spectral shifts in the resonance wavelength, one can directly measure molecular binding to a nanoparticle surface through minute changes in the particle's dielectric environment.

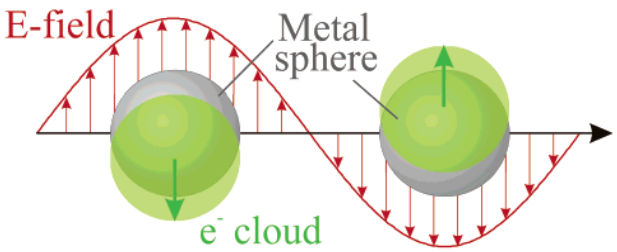

Figure 2.9 Localized surface plasmon excited in metal spheres showing the displacement of the conduction electron charge cloud relative to the nuclei.

When a small spherical metallic nanoparticle is irradiated by light, the oscillating electric field causes the conduction electrons to oscillate coherently. This is schematically pictured in Figure 2.9. When the electron cloud is displaced relative to the nuclei, a restoring force arises from Coulomb attraction between electrons and nuclei that results in an oscillation of the electron cloud relative to the nuclear framework. The oscillation frequency is determined by four factors: the density of electrons, the effective electron mass, and the shape and size of the charge distribution.

The collective oscillation of the electrons is called the dipole plasmon resonance of the particle (sometimes denoted “dipole particle plasmon resonance” to distinguish from plasmon excitation that can occur in bulk metal or on metal surfaces).

Higher modes of plasmon excitation can occur, such as the quadrupole mode where half of the electron cloud moves parallel to the applied field and half moves antiparallel [44].

2.7 Sensitivity comparison between surface Plasmon and localized surface Plasmon

The differences in sensitivity between the LSPR and SPR measurements can be understood from a simple analysis. Following Homola [45] where he derived The refractive index sensitivity by differentiating the Plasmon resonance position vector with respect to n (refractive index). Also one may derive the LSPR sensitivity to a refractive index change in the same spirit by assuming that a localized plasmon is characterized by a dipole polarizability resonance condition of the same form as that for a particle in the quasistatic limit [46]. The sensitivity is then obtained by differentiating the resonance condition with respect to *n*. The results for the SPR and LSPR bulk sensitivities are

$$\frac{\partial \lambda_{SPR}}{\partial n} = 2\,\varepsilon^{'}/n^{3}\,\frac{\partial \varepsilon^{'}}{\partial \lambda}$$

$$\frac{\partial \lambda_{lSPR}}{\partial n} = 2\,\varepsilon^{'}/n\,\frac{\partial \varepsilon^{'}}{\partial \lambda}$$

The dielectric function of metal $\varepsilon_d = \varepsilon^{'} + i\varepsilon^{''}$ where $\varepsilon^{'}, \varepsilon^{''}$ are the real and imaginary part of the dielectric function of metal

In general one of the exciting features of surface plasmons is their ability to confine light at a metal/dielectric interface, which can either be localized or propagate depending upon the dimensionality of the nanostructure material. This confinement of light at the interface results from the collective oscillation of the conduction electrons at the metal surface [47-48].

When these conduction electrons are excited by an external electromagnetic field, formation of a dipole in the nanoparticle is induced.

A compensating restoring force in the nanoparticle originating from positive excess charges of the lattice causes the conduction electrons to perform collective oscillations. The response of metal free electrons can be described by the dielectric function of the metal.

2.8 Dielectric function of metal

The description of optical properties of metals is often done with a model dating back to Paul Drude. This model assumes that the response of a metal particle is found by first considering the influence of external forces on one conduction electron alone. The macroscopic response is then obtained by multiplying the effect of the single electron by the total number of electrons.

Drude considered the conduction electrons in metals as quasi-free, i. e. there is no significant interaction between electrons among each other or between electrons and the metal ion cores. The response of a free electron of mass m_e and charge e to an external electric field $E = E_0 e^{-iwt}$ is given by [49]

$$m_e \frac{\partial^2 r}{\partial t^2} + m_e \gamma \frac{\partial r}{\partial t} = e E_0 e^{-iwt} \qquad 2.20$$

where γ denotes the damping constant. Equation 2.20 has been solved to yield the dipole moment and polarization. For simplicity, we consider a homogeneous isotropic medium under the influence of an external alternating electromagnetic field E. The polarization p connects to the dielectric function $\varepsilon(\omega)$ by the definition $\varepsilon = 1 + p/(\varepsilon_0 E)$, ε is related to the complex index of reflection by $n+ik = \sqrt{\varepsilon}$.

Introducing

$$p = n\alpha E$$

and

$$\varepsilon - 1 = \frac{1}{\varepsilon_0} n\alpha$$

where α is the polarizability, the dielectric function $\varepsilon(\omega) = \varepsilon_1(\omega) + i\varepsilon_2(\omega)$ of a system of n free electrons per unit volume can be written as

$$\varepsilon(\omega) = 1 - \frac{\omega_p^2}{\omega^2 + i\gamma\omega} = 1 - \frac{\omega_p^2}{\omega^2 + \gamma^2} + i\frac{\omega_p^2}{\omega(\omega^2 + \gamma^2)} \qquad 2.21$$

Where $\omega_p = \left(\frac{4\pi n_e e^2}{m^*}\right)^{\frac{1}{2}}$ is the bulk plasma frequency.

The real and imaginary parts of ε are

$$\varepsilon_1(\omega) = 1 - \frac{\omega_p^2}{\omega^2}, \quad \varepsilon_2(\omega) = 1 - \frac{\omega_p^2}{\omega^3}\gamma \qquad 2.22$$

For the high frequency region of the spectrum, a high frequency term ε_∞ [50] is added to the Drude contribution for accurately describing the response of metal electrons to the electromagnetic field:

$$\varepsilon = \varepsilon_\infty - \frac{\omega_p^2}{\omega^2 + i\gamma\omega} \qquad 2.23$$

For real metals, bound electrons contribute to the dielectric function. Thus, when describing the optical properties in the visible range, ε_∞ = const. is substituted by a term accounting for interband transitions, it is common to express the dielectric function $\varepsilon(\omega)$ in term of the electric susceptibility x to give $\varepsilon(\omega) = 1 + x^D(\omega)$, so that the complex dielectric function including all optical properties of a real metal in the visible range is given by [49] it is common to express the dielectric function $\varepsilon(\omega)$ in term of the electric susceptibility x

$$\varepsilon(\omega) = 1 + x^{IB}(\omega) + x^D(\omega) \qquad 2.24$$

$x^D(\omega)$ is the polarization of free electrons according to Drude, and $x^{IB}(\omega)$ is the contribution due to interband transitions (excitation of d and s electrons).

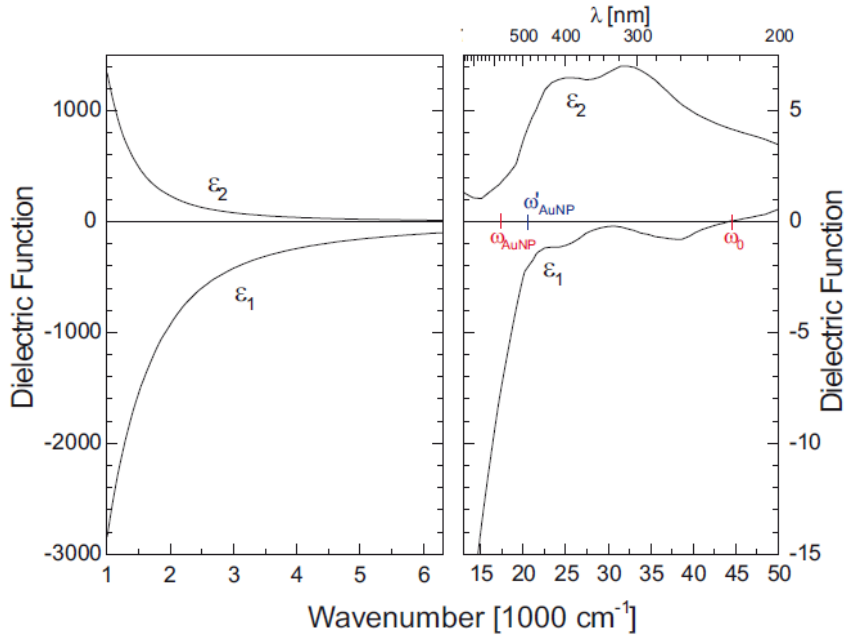

Figure 2. 10 Dielectric function of bulk Au in the mid IR (left) and the UV/VIS range (right, different scale).[51-52]

Fig 2.10 shows the dielectric function of gold. As also for other metals the dielectric function of gold is characterized by a negative ε_1 and a positive ε_2 with decreasing value approaching near IR. In the visible region ε_1 becomes zero at frequency ω_0 and turns positive for $\omega > \omega_0$. On the other hand, ε_2 increases strongly in the visible range, as this range dominated by interband transitions. In the region $\omega < \omega_0$, light is almost completely unable to penetrate the metal and is reflected to a very high degree. In this region metals have the typical high reflectivity due to the large number of free charge carriers. For $\omega > \omega_0$ ε_1 is approaching unity. Interband transitions also give contributions, but cannot significantly influence ε_1 which means that the reflectivity decreases and the metal becomes transparent (UV transparency of metals). The increase of absorption due to interband transitions and the decreasing reflection in the violet range are the reason for the typical yellow shine of bulk Au.

2.9 Metal nanoparticles

To explain the origin of red color of gold nanoparticle solutions, Mie 1908 [53] solved Maxwell's equation for an electromagnetic light wave interacting with small spheres having the same macroscopic, frequency dependent dielectric constant as the bulk metal. The solution of this electrodynamics calculation with appropriate boundary conditions for a spherical object leads to a series of multipole oscillations for the extinction cross-section of the nanoparticles. The derivation of it can be found in [49, 53]. For nanoparticles with diameter d = 2r much smaller than the wavelength of light, i.e. $2r \ll \lambda$, only the dipole oscillation contributes significantly to the extinction cross-section. In this case, Mie theory yields [54]

$$\alpha = (1+k)\varepsilon_0 V \frac{\varepsilon - \varepsilon_m}{\varepsilon + k\varepsilon_m} \qquad 2.25$$

Where V is the particle volume, ε_m is the medium dielectric constant, k is a shape factor that incorporates the dependence of the polarizability on the geometry of the surface that defines the electron oscillations. $k = 2$ For spheres, where the resonance condition is fulfilled when $\varepsilon(\omega) = -2\varepsilon_m$. For other shapes (e.g. triangles, rod-shaped particles) the value of k can be much higher [55]. Thus the resonance properties of the nanoparticles depend on the shape and the surrounding medium because they polarize each other and the charge density has to adjust not only to the incident field but also to the fields caused by polarization. Equation 2.25 explains the absorption spectra of small metallic nanoparticles in a qualitative as well as a quantitative manner. However, for larger nanoparticles the spectral response is modified due to retardation effect and the excitation of higher-order modes. The larger the particles become, the more important are the higher-order modes as the light can no longer polarize the nanoparticles homogeneously. This leads to a red shift of the dipolar resonance as well as to a broadening of the band width of the peak.[47] [49], as the conduction electrons do not all move in phase anymore. Additionally, radiative losses[56] begin to significantly contribute to plasmon damping, dominating the total damping of Au and Ag nanoparticles for particle sizes in excess of 100 nm.

The depolarization field and radiation damping effect can be regarded as lowest-order corrections to the quasistatic theory, leading to additional real and imaginary parts of the denominator of the polarizability.

On the other hand, for particles with a diameter smaller than the free-electron scattering length, scattering processes at the particle surface are thought to begin to contribute to the total damping.[49]

These additional damping mechanisms for large and small particles lead to respective decreases in the total enhancement of the exciting field via a decrease of the plasmon dephasing time[49].

Modern fabrication methods allow for the synthesis of metal nanoparticles with a variety of shapes using both colloidal synthesis methods and top-down nanofabrication techniques such as electron-beam lithography. Such way, they open the field for research on the effect of size and shape on the optical properties of metal nanoparticles of different shape. One of the most interesting shapes is the metal nanoshell.

2.9.1 Metal nanoshells

Metal nanoshells are new type of nanoparticles composed of a dielectric core, such as silica, coated with metallic layer, usually metal colloid. The plasmonic properties of such structures are determined by the dimension of the inner and outer radii of the metallic shell and the dielectric constant of the constituting material. They are straight forward to theoretically model and easy to fabricate. They can be tuned to absorb or scatter light at specific wavelengths in the visible and near-infrared (NIR) region of spectrum. The concentric spherical geometry of the nanoshell enables its plasmon resonance to be easily predicted by Mie theory, which is extended for such structures by considering them a concentric sphere of different material. However, Mie theory fails to explain why the position of the peak can be tuned by adjusting the core/shell ratio. In order to account for the origin of this tunability, one must consider the plasmon hybridization picture. In this hybridization picture, the plasmon resonance of the metal shell is the result of the electromagnetic coupling between the inner surface cavity plasmon and the outer surface sphere plasmon.[57-58].

The strength of interaction depends on the thickness of the gold shell, and hence the core shell ratio. The frequency of the bonding (ω_-) and anti-bonding (ω_+) plasmon modes decomposed as spherical harmonic of order l are given by [58]

$$\omega_{l_{\pm}}^2 = \frac{\omega_p^2}{2}\left[1 \pm \frac{1}{2l+1}\sqrt{1 + 4l(l+1)\left(\frac{r_1}{r_2}\right)^{2l+1}}\right] \quad 2.26$$

Where ω_p is the bulk plasmon frequency r_1 and r_2 are the inner and the outer radii of the metal shell, respectively.

Although an increase in the core/shell ratio generates lower-frequency plasmon modes, which are the same as the ones obtained from a Drude dielectric function and classical Mie scattering in the dipole limit, this model clearly elucidates, the microscopic origin of the metal shell tunability

2.9.2 Silver and gold nanoparticles

Despite the fact that gold and silver have similar bulk plasma frequencies (in the UV) due to their similar electronic densities (i.e. $N = 5.90 \times 10^{22}\ /cm^3$ for gold and $N = 5.86 \times 10^{22}\ /cm^3$ for silver) the onset of $d \rightarrow sp$ inter –band transition is different in the two metals resulting in different LSPR positions. In case of gold, the onset of the inter-band transition around 1.7 ev not only red-shifts the collective free electron resonance to the observed position [50] at 520nm but also strongly damps the plasmon resonance band resulting in its increased broadening and absorptive dissipation compared to silver (fig.2.11). The narrow sharp peak in case of Ag yields better resolution in sensing applications.

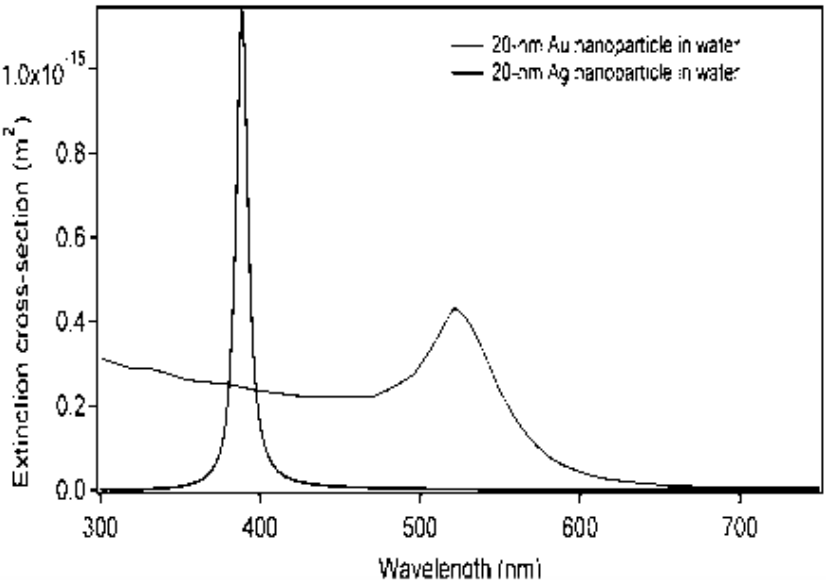

Figure 2. 11 The extinction spectrum (from Mie theory) of a 20-nm silver nanosphere showing LSPR around 380 nm and that of a 20-nm gold nanosphere with an LSPR at 520 nm. [54]

2.9.3 Coupling between metal nanoparticles

When two metal nanoparticles are brought in proximity to each other, the electric field of one particle can interact with the other [59-60] causing significant differences between the extinction spectra of metallic NPs in dispersed and aggregated states. The coupling process between neighboring metallic NPs has been experimentally observed for systems consisting of pairs,[48, 59, 61] linear chains,[62-63] and planar arrays [64] of nanodiscs. In an ordered array of nanoparticles each nanoparticle acts as an electric dipole. Two types of electromagnetic interaction between particles can be distinguished, depending on the spacing between the adjacent nanoparticles [47].

For particle spacing on the order of the exciting wavelength, far-field interactions with d^{-1} dependence dominate. The existence of such interactions has been studied by quantifying their influence on both the spectral peak position and the plasmon damping characteristics [65].

For particle spacing much smaller than the wavelength of light, near field coupling between particles in ordered arrays dominates with distance dependence with exponential decay [62, 66].

This results in a red shift (for light polarized parallel to the interparticle axis) in the plasmon resonance, which increases with decreasing interparticle separation, and decays approximately exponentially with increasing particle separation[48] as shown in the fig. 2.12. Such decay is independent of the shape of the particles.

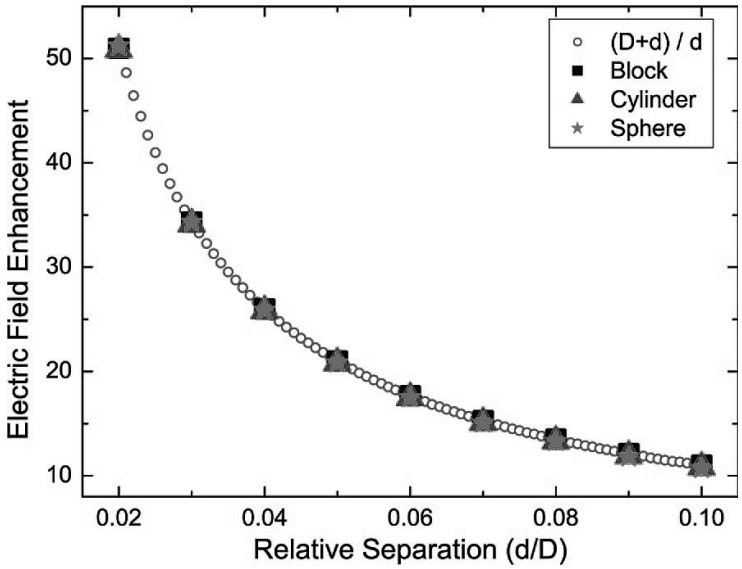

Figure 2. 12 Electric Field Enhancement for sphere, cylinder, and block arrays, respectively as a function of the gap/diameter ratio [28]

The plasmon coupling between metal nanoparticles assembled in pairs or 1-D chains has been shown, mainly through simulations, to result in a huge enhancement in the electric field at the junction between the nanoparticles, especially at small gaps.[67-69]. The field enhancement at the junction is further increased in the case of coupling between sharp tips (with highly concentrated fields), as found for nanotriangles interacting tip-to-tip [70]and nanorods interacting end-to-end [71]. Such near field coupling between nanoparticles in ordered arrays can lead to "hot spots" (between the particles) of extremely large field enhancement, which enable such structure to be used in single-molecule spectroscopy[72].

As well improve the sensitivity of the nanoparticles to the local environment as these enhanced fields are localized at the surface of the nanostructure. This fact has been employed in sensing applications [73-74].

2.9.4 Substrate effect on the metal nanoparticles

Most of the nanoparticles in practical applications are supported on a substrate. However, the interaction between the metal nanoparticle and supporting material affects physical properties of the nanoparticles. The presence of substrate has two major effects on the metal nanoparticles. First, the symmetry of the system is broken. Second, the wetting effects give rise to intricate cluster shape [49].

The first effect is treated by replacing the spherical particle on the substrate by a spherical particle in a matrix with an average dielectric function value between the vacuum value and that of the supporting substrate. This is a qualitative approximation as the substrate itself is observed to be polarized during the excitation of the particle which is described by introducing a mirror image dipole effect. The mirror image dipole effect results in red shift of the resonance peaks of the plasmon resonance of metal nanoparticles on metal substrates. These resonance peaks blue shift with increasing nanoparticles-substrate separation. The fact that a spacer layer usually red shifts the plasmon resonance of the metal nanoparticles has nothing to do with the metal particles-film separation, but depends only on the permittivity of the spacer layer. However, the role of the spacer layer in the experiments is always complicated but can be rationalized qualitatively.

As a general fact, the presence of a substrate decreases the sensitivity of the metal nanoparticles[75] and the presence of dielectric spacer with optimum thickness of high refractive index improves the sensitivity.

2.10 Surface plasmon resonance as biosensor

Plasmon resonance based biosensors have been accomplished in different ways. In the past, SP mode propagation on functionalized thin metal films was exploited.[7, 76] Changes in the environment due to binding of molecules to functionalized films can be monitored as changes in the angle of incidence required for surface plasmon excitation in an evanescent coupling geometry. Recently, metal nanostructures with different shapes and dimensions and nanopatterned surfaces have also been used as nanoscale SPR sensors.[13, 77] Here, the surface plasmon peak of the metal nanoparticle is greatly influenced by the local dielectric environment.

This fact has been employed in sensing applications [78] where the plasmon peak position has been directly related to the refractive index of the surrounding medium (n) based on the equation [79]

$$\Lambda^2 = \Lambda_p^2(\varepsilon^\infty + 2\varepsilon_m) \qquad 2.27$$

Where, $\Lambda_p = \frac{(2\pi c)^2}{\omega_p^2}$ is the bulk plasmon wavelength, ε^∞ is the high-frequency dielectric constant due to interband and core transitions, and ε_m is the dielectric constant of the medium (the refractive index of the medium is directly related to the dielectric constant $n=(\varepsilon_m)^{\frac{1}{2}}$).

From this equation we can see the dependence of the peak positions of the metal nanostructures on their local dielectric environment, typically revealed through a shift in their position as a function of changing the chemical and physical environment of the nanoparticles. In the case of extremely low analyte concentrations, e. g., sensing of pollutants or biological agents as DNA, extremely high analyte sensitivity is required. This would require a large shift in the SPR wavelength peak in response to relatively small changes in the medium refractive index. The dependence of the SPR sensitivity on the metal type and the nanoparticle shape has been discussed by Lee and El-Sayed [14]. Choosing a metal with a steeper wavelength dependence of the real part of the dielectric constant is expected to result in a higher SPR sensitivity. However, the choice of metals is limited to Ag and Au, both of which have a similar wavelength dispersion of the real part of the dielectric constant[14].

Many theoretical and experimental studies [74, 80-81] have been made on metal nanoparticles with different geometry to find the best configuration to enhance the sensitivity of the plasmon resonance response to the changes in the refractive index of the surroundings.
An interesting non-spherical shape offering high SPR sensitivity to the local dielectric environment is the triangular nanoparticle structure[13] , which can be fabricated in a homogeneous array on a substrate by the nanosphere lithography (NSL) method utilized by the van Duyne group[82].

It has been shown that the SPR extinction band of an array of Ag nanotriangles with in-plane width of 100 nm and out-of-plane height of 50 nm yields a sensitivity of 200 nm/unit refractive index change in the solvent medium [77]. When an alkanethiol monolayer is self-assembled onto the nanoprisms, a shift of 3 nm per methylene unit of the alkanethiol is observed [77].

This high sensitivity to the surrounding medium and ligand environment has been exploited for biosensing [13]. Adsorbate-induced shift in the SPR band is primarily caused by the local dielectric environment changes due to the adsorbing molecules. The shift itself is not specific to the chemical or biological species being adsorbed. However, the specificity desired for biosensing applications is achieved by employing surface ligands with the ability to specifically bind the analyte molecules and eliminating nonspecific surface adsorption [83]. Van Duyne and coworkers [13] demonstrated this using the well-established streptavidin–biotin system. The triangular nanoparticles were coated with a monolayer of alkanethiol molecules with terminal carboxylic acid groups that could be used to attach biotin by common coupling chemistry.

Nanoshell structures also show high sensitivity. It has recently been reported [84-85] that the sensitivity is closely related to geometrical parameters, namely, the relative ratio of the shell thickness to the core radius. In general, core-shell particles with thinner metal shells exhibit plasmon resonances in the near-infrared (near-IR) region along with high sensitivity. Also some attempt was made to enhance the sensitivity by arranging nanoshells in an array so that they interact with each other. Immobilized on a substrate they were used as chips for analyte detection.

Recently, an advanced combination of plasmonic metal nanoparticles and interference in a thin-film multilayer was utilized. By monitoring the relative reflectance value of the plasmon band of Interference Localized Surface Plasmon Resonance (iLSPR) substrates, biotin-avidin binding events were monitored in real time with a detection limit of 1 μg/mL [22]

2.11 Effective medium theory, the Maxwell-Garnett theory

In general, Mie theory is only valid for very low concentrations of the nanoparticles in a solvent or a solid matrix [49]. It is assumed that the individual particles are non-interacting and separated from one another. Therefore, the electric field created around one particle by the excitation of a surface plasmon resonance is not felt by the other surrounding particles. If the interparticle distances become smaller than the particle dimension or if aggregation occurs, the plasmon resonance red shifts and often a second absorption peak at a longer wavelength is observed [49, 86-88]. In case of particle aggregation and for composite materials such as densely packed nanoparticles in a transparent host medium here f_m is not much smaller than one which is required for eq. 2.25 to be valid!, the effective-medium theories are better suited to explain their optical absorption spectra.

Maxwell-Garnett theory is an effective-medium theory that considers an ensemble of small metal particles embedded in a surrounding medium. The individual polarizabilities of the particles are summarized, and the local-field effects of the particles are taken into account. The Maxwell-Garnett theory is based on the Clausius-Massotti equation and it assumes that it is justified to describe the composite material containing metal nanoparticles embedded in an inert host medium by an effective complex dielectric constant ε_c, such that [49, 89-90]

$$\frac{\varepsilon_c - \varepsilon_m}{\varepsilon_c + k\varepsilon_m} = f_m \frac{\varepsilon - \varepsilon_m}{\varepsilon + k\varepsilon_m} \qquad 2.28$$

ε and ε_m are the dielectric constants of the metal nanoparticles and the host medium, respectively.

In contrast to Mie theory, ε_m is also a complex function depending on the frequency of the light. f_m is the volume fraction of the metal nanoparticles in the composite material, where $f_m \ll 1$, and k is the screening parameter depending on the shape of the nanoparticles.

It has the value of two for spheres and one for nanorods. With the knowledge of ε and ε_m from literature and an estimation of f_m from the sample preparation procedure, the dielectric constant ε_c of the composite material, composed of the nanoparticles and the host, can be computed using equation 2.28.

2.11.1 Bruggeman model

Our system is more complicated than just nanoparticles that interact in solution. We have nanoparticles immobilized on substrate so that interactions between particles and the substrate exist [91] and $f_m \ll 1$ is not fulfilled any more. An effective medium model for such systems is the Bruggeman model, in which the effective dielectric constant follows from

$$(1 - f_m)\frac{\varepsilon_m - \varepsilon_c}{\varepsilon_m + (D-1)\varepsilon_c} = f_m \frac{\varepsilon - \varepsilon_c}{\varepsilon + (D-1)\varepsilon_c} \qquad 2.29$$

Here, D is the effective dimension of the film. This equation is known as the Bruggeman formula and for D=3 can explain the optical properties of gold nanoparticles immobilized on a substrate [92]. In the literature a lot of different effective medium models can be found.

Usually, each model is based on different assumptions about the shape, orientation and number of basic unit cells and assumes different kinds of interaction. Therefore, each model has its own range of applicability. For example, Yamaguchi et al.[93] Introduced an effective medium model that was optimized for the description of a thin metal film consisting of ellipsoidal particles:

$$\varepsilon_c = 1 + f_m \frac{\varepsilon - \varepsilon_m}{1 + q\frac{\varepsilon - \varepsilon_m}{\varepsilon_m}} \qquad 2.30$$

Where, q is the depolarization factor that considers the non-spherical shape of the particles.
In [94] a model is found describing the extinction spectra of colloidal dispersion of gold nanoparticles in the visible range. Here, the dielectric function of gold is described as an extended Drude model with an additional Lorentzian term.
The authors show that this leads to a good fit of the experimental values of the dielectric function obtained by Johnson and Christy [51]

2.12 Antibody-antigen interactions

Antibodies (also: immunoglobulin, Ig) are proteins that are produced by an animal or human as a reaction to the presence of an external substance (antigen). Their function is to disarm antigens and thus to protect the animal or human against infections and diseases. The basic structure of an antibody molecule is Y-shaped (fig 2.13) consisting of two identical heavy chains and two identical light chains connected by disulfide bonds. Antibodies of type G (IgG), most commonly found in human serum, consist of one of these basic units and have a molecular weight of about 150.000 g/mole. Antibodies have an especially high affinity to the antigen that has stimulated their expression. The antigen is identified by a special group, the antigenic determinant (epitope). This group couples with a binding site of the antibodies according to the key-lock principle. The basic structure of an antibody has two binding sites; therefore two identical epitopes can be bound. If these two epitopes belong to different antigens, they are cross linked [95-96]. Polysaccharides, nucleic acids and proteins (and therefore antibodies themselves) can act as antigens. Immune response is usually only generated if the size of the antigen exceeds about 10.000 g/mole.

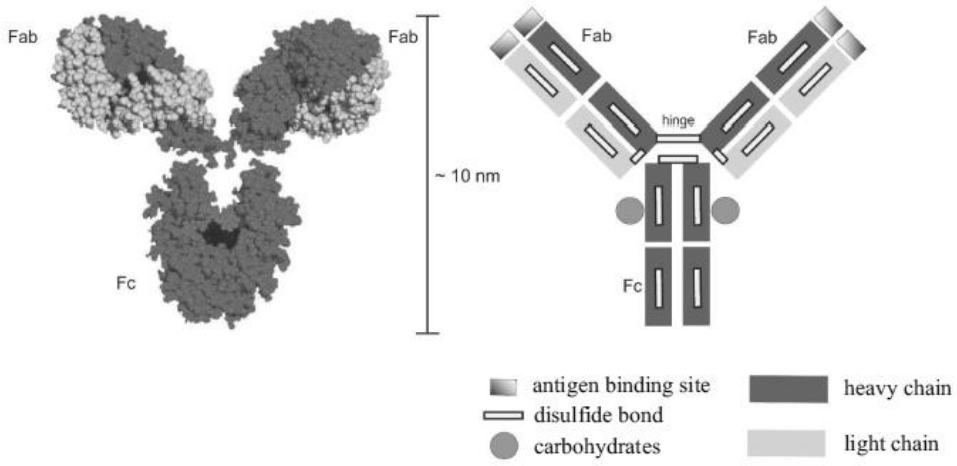

Figure 2. 13 Chemical structure of an antibody molecule according to [97](left), and schematic composition (right). The antibody consists of two identical light and heavy polypeptide chains connected via disulfide bonds. The binding sites for antigens are at the end of the Fab fragments

Characterization of the samples

2.13 Scanning electron microscope (SEM)

SEM is a type of electron microscope that images the sample surface by scanning it with a high energy beam of electrons; these electrons interact with the atoms that make up the sample producing signals that contain information about the sample's surface topography[98] as well as composition. Since microscopic resolution is limited by the wavelength of the illumination, magnification and resolving power of a SEM is much higher compared to an ordinary light microscope. Nowadays, SEMs are available which have a resolution of less than one nanometer.

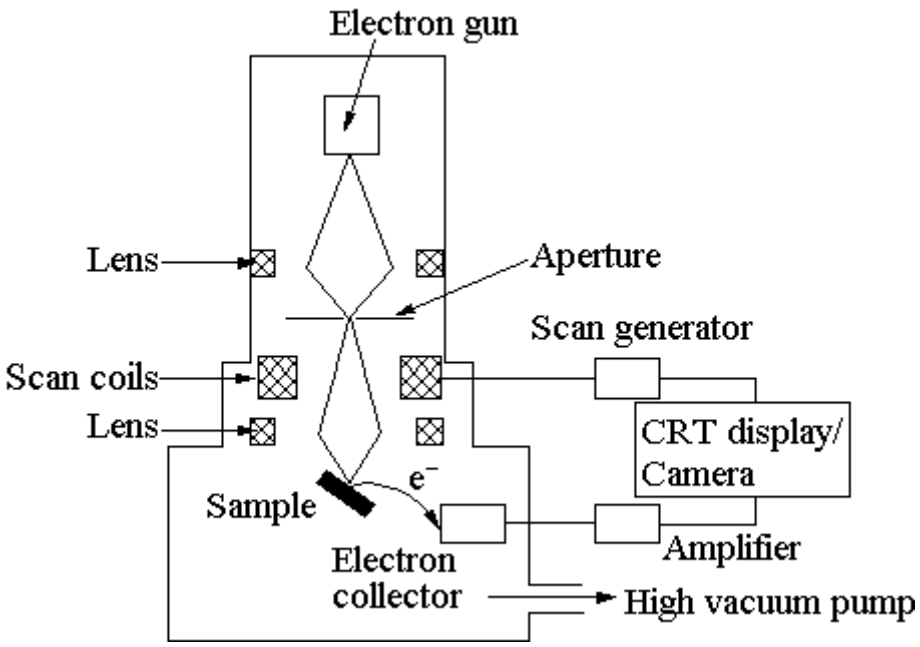

Figure 2.14 Schematic describing the operation of an SEM [99]

2.13.1 Physical Basis of Operation

In the SEM, a source of electrons is focused into a fine probe that is rastered over the surface of the specimen, Fig 2.14. As the electrons penetrate the surface, a number of interactions occur that can result in the emission of electrons or photons from (or through) the surface. A reasonable fraction of the electrons emitted can be collected by an appropriate detector, converted to a voltage, and amplified.

The amplified voltage is then applied to the grid of cathode ray tube (CRT) and modulates or changes the intensity of the spot of light on the surface; a large number of the emitted electron from the sample will be detected, causing a large voltage in the detector that result in bright spot on the surface of the CRT. If the beam of electrons then moves to a depression on the sample, fewer electrons will be detected and smaller voltage will develop result in a darker spot on the surface of the CRT: the SEM image consist of thousands of spots of varying intensity on the surface of the CRT that represent the topography of the sample. The image is digitally captured and displayed on a computer monitor.

2.13.2 Sample preparation

All samples measured by SEM must be of appropriate size to fit in the specimen champers and are generally mounted rigidly on the holder by specimen stub. For conventional imaging in the SEM specimens must be electrically conductive, at least at the surface, and electrically grounded to prevent the accumulation of electrostatic charge at the surface. Metal objects require little special preparation for SEM. Nonconductive specimens tend to charge when scanned by the electron beam, and especially in secondary electron imaging mode, this causes scanning faults and other image artifacts. They are therefore usually coated with an ultrathin coating of electrically-conducting material, commonly silver.

Two reasons for coating, even when there is enough specimen conductivity to prevent charging, are to increase signal and surface resolution, especially with samples of low atomic number (Z). The improvement in resolution arises because backscattering and secondary electron emission near the surface are enhanced and thus an image of the surface is formed.

2.13.3 Sample-beam interactions

When an incident-beam electron strikes the surface of a sample, it undergo as series of complex interactions with the nuclei and electrons of the atoms of the sample. Due to these interactions a verity of secondary products produces as electrons of different energy, x-rays, heat, and light. Where, many of these secondary products are used to produce the images of the sample. The interaction between incident electron and atoms of the sample may be elastic or inelastic.

Elastic interactions occur between incident electron and the nucleus of the atom of the sample and are characterized by large-angle of deflection of the incident electron and little energy loss by the incident electron (backscattered electrons).

Inelastic interactions occur between incident electrons and the orbital shell electrons of the atom of the sample and characterize by a small angle of deflection of the incident electron, as well as much energy loss by the incident electron (secondary electrons)

2.13.4 Detection of secondary electrons

Due to their low energy, these electrons originate within a few nanometers from the sample surface.[100] The electrons are detected by an Everhart-Thornley detector [101] which is a type of scintillator-photomultiplier system. The secondary electrons are first collected by attracting them towards an electrically-biased grid at about +400 V, and then further accelerated towards a phosphor or scintillator positively biased to about +2,000 V. The accelerated secondary electrons are now sufficiently energetic to cause the scintillator to emit flashes of light which are conducted to a photomultiplier outside the SEM column via a light pipe and a window in the wall of the specimen chamber. The amplified electrical signal output by the photomultiplier is displayed as a two-dimensional intensity distribution that can be viewed and saved as a digital image. This process relies on a raster-scanned primary beam. The brightness of the signal depends on the number of secondary electrons reaching the detector. If the beam enters the sample perpendicular to the surface, then the activated region is uniform about the axis of the beam and a certain number of electrons "escape" from within the sample

2.13.5 Detection of backscattered electrons

Backscattered electrons (BSE) consist of high-energy electrons originating in the electron beam; they are reflected or back-scattered out of the specimen interaction volume by elastic scattering interactions with specimen atoms. Since heavy elements (high atomic number) backscatter electrons more strongly than light elements (low atomic number), and thus appear brighter in the image, BSE are used to detect contrast between areas with different chemical compositions.[100]. The Everhart-Thornley detector, which is normally positioned to one side of the specimen, is inefficient for the detection of backscattered electrons because few such electrons are emitted in the solid angle subtended by the detector, and because the positively biased detection grid has little ability to attract the higher energy BSE electrons. Dedicated backscattered electron detectors are positioned above the sample in a "doughnut" type arrangement, concentric with the electron beam, maximizing the solid angle of collection. BSE detectors are usually either of scintillator or semiconductor types. When all parts of the detector are used to collect electrons symmetrically about the beam, atomic number contrast is produced. However, strong topographic contrast is produced by collecting back-scattered electrons from one side above the specimen using an asymmetrical, directional BSE detector; the resulting contrast appears as illumination of the topography from that side.

2.13.6 Resolution of the samples

The spatial resolution of the SEM depends on the size of the electron spot, which in turn depends on both the wavelength of the electrons and the electron-optical system which produces the scanning beam. The resolution is also limited by the size of the interaction volume, or the extent to which the material interacts with the electron beam. The spot size and the interaction volume are both large compared to the distances between atoms, so the resolution of the SEM is not high enough to image individual atoms, as is possible in the shorter wavelength (i.e. higher energy) transmission electron microscope (TEM). The SEM has compensating advantages, though, including the ability to image a comparatively large area of the specimen; the ability to image bulk materials (not just thin films or foils); and the variety of analytical models available for measuring the composition and properties of the specimen. Depending on the instrument, the resolution can fall somewhere between less than 1 nm and 20 nm.

The world's highest SEM resolution at high beam energies (0.4 nm at 30 kV) is obtained with the Hitachi S-5500. In this thesis, numerous SEM images were used to display the topography and the coverage of the surfaces.

2.14 Ellipsometry

Ellipsometry is an optical technique which can be used to measure the polarization changes occurring at oblique reflection from a surface. These polarization changes are very sensitive to the presence of a thin film or a layer of adsorbed molecules [102]. When polarized light is reflected from a surface coated with a thin film, the polarization and intensity of the light are changed due to the properties of the thin film, such as the optical constants (complex refractive index and dielectric function tensor) and film thickness. By detecting and analyzing the changes in polarization and intensity of the light, optical constants and film thickness can be determined.

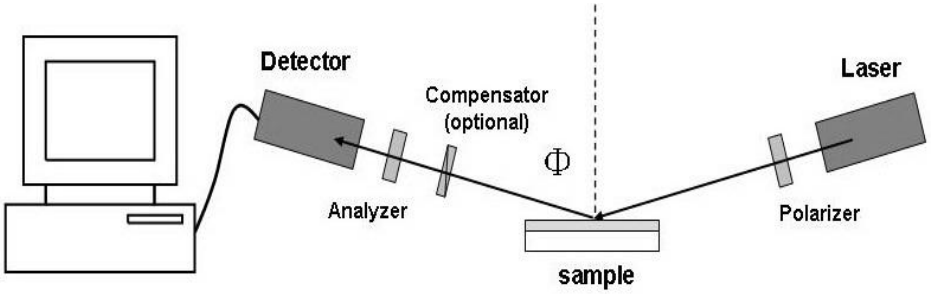

Figure 2. 15 Schematic experimental setup of ellipsometry technique [103-104]

Figure 2.15 shows a schematic setup for an ellipsometry experiment. Incident light from a source is linearly polarized to two polarization states by a polarizer.

If the electric field of the polarization state is perpendicular to the plane of incidence, it is called s-polarized. If the electric field of the polarization state is parallel to the plane of incidence, it is called polarized. Due to the absorption of the sample (thin film), the reflected wave is not linearly polarized but elliptically polarized [103].

The changes in polarization of the reflected light are analyzed and detected by an analyzer and a detector, and the signals are converted for analysis and calculation by the computer.

The parameters of the polarization ellipse are determined by the optical constants and the thickness of the thin film. We can calculate the thickness of a thin surface film providing that the optical properties of the substrate and the ambient are known, as well as the angle of incidence and the wavelength of the light. The amplitude of the wave changes after reflection from the sample surface. The Ellipsometry measures the ratio of the reflection coefficient (r_{1s} and r_{1p}) however this ratio is represented in terms of ellipsometric angles, ¥ and Δ as [105]

$$\rho = \frac{r_p}{r_s} = \tan ¥ \exp((i\Delta)$$

The ratio is a complex number, and contains phase information Δ that makes the measurement very sensitive [106]

The measured ¥ and Δ cannot be converted directly into the optical constant of the samples; a model analysis must be performed. This model considers the optical constant and thickness parameters of all individual layers of the sample. Using an iterative procedure (least squares minimization) unknown optical constants and/or thickness parameters are varied, and ¥ and Δ values are calculated using the Fresnel equations[106]. The calculated ¥ and Δ values which match the experimental data best provide the optical constants and thickness parameters of the sample. In ellipsometry, a spectroscopic measurement is more sensitive and also provides more information than a single wavelength measurement. Ellipsometry works best for film characterization when the film thickness is of the same order as the wavelength of the incident light [106]. Therefore, it is more sensitive to characterize a thin film in the short wavelength region or a thick film in the long wavelength region. The optical constants of a sample can be correlated to the wavelength of the incident light by some empirical equations (such as the Cauchy equation). In this case, the spectral dependent equations can be applied to analyze the experimental data acquired over a certain region. Surfaces with large roughness can cause non-specular scattering of the incident beam and depolarization of the specularly reflected beam [106] therefore they are not suitable for ellipsometry measurement.

The ellipsometry measurements were performed on a fixed-angle M-44(TM) ellipsometer (J.A.Woollam, USA).

The lamp housing and lamp power supply are integrated into one unit (LPS-400). The arc lamp, a high pressure Xe discharge point source lamp, serves as the light source. A fiber optic cable is used to couple the beam from the lamp housing to the input unit of the ellipsometer.

The input unit conditions the beam before it encounters the sample. The output unit consists of an analyzer and a detector that further condition the beam and converts it into electrical signals. The main computer operates the WVASE32(TM) data acquisition and analysis software. The main function of this computer is to communicate with the remote computer located within the EC-120 electronics control box. It also analyzes all data acquired from the embedded computer and displays the results on the screen.

2.14.1 Ellipsometry Measurements

After sequentially switching on the arc lamp, the EC-120 electronics control box, the computer, the hardware of the M-44(TM) system has to be initialized by the WVASE32(TM) software. Then a reference sample is placed on the sample stage for beam alignment. A good alignment can be achieved by adjusting the height and tilt of the sample stage to make sure that the reflection of the beam from the sample surface is centered on the detector aperture. After alignment, system calibration is performed with a standard sample (silicon wafer covered with 25 nm SiO2) at 500 nm wavelength and 75.05 angle of incidence. The sample is placed on the stage and the beam is properly aligned. Then experimental data is acquired and saved. Thereafter, a suitable model is established for the measured sample. The Cauchy model is usually applied for organic thin films.

The Cauchy equation is an empirical relationship between the refractive index n and the wavelength of light λ for a particular transparent material. The general form of the Cauchy equation is[107]

$$n(\lambda) = A + \frac{B}{\lambda^2} + \frac{C}{\lambda^4} + \cdots$$

where A, B, C, etc., are coefficients that can be determined for a material by fitting the equation to measured refractive indices at known wavelengths.

Usually, it is sufficient to use a two-term form of this equation

$$n(\lambda) = A + \frac{B}{\lambda^2} + \frac{C}{\lambda^4}$$To have reliable statistical results, usually the samples measured three times at different spots and the averages were calculated.

Chapter 3

3- Experimental Part

3.1- Chemicals

3.1 a- For samples preparation

Silica colloidal beads with a nominal diameter of 400 ± 40 nm (10 wt.% solution in water) were purchased from Polyscience Polyethylenimine (PEI) high molecular weight, water free Phosphate Buffered saline (PBS) tablets of pH 7.4, OH terminated solution silica particles, Sodium thioglycate powder (TG, 97%), Sodium citrate tribasicDihydrate, ACS reagent, >= 99.0%, Gold (III) chloride trihydrate, 99.9 silver nitrate 99.9, Sodium borhydride, 99% Hydroxylamine, formaldehyde MW 30.03, Poly (sodium 4-styrenesulfonate) (PSS) MW 70,000, polyallylamino-hydrochlorid (PAH) MW 60,000 from sigma-Aldrich. PL-latex plain from polymer lab, amine terminated SiO_2 (silica) particles with a diameter of ~ 510nm were purchased from Bangs Laboratories in form of a powder (10 wt. % solution). Sodium dodecyl sulfate solution, BioUltra (10% inH_2o), and TritonX-100, Ethanol were purchased from Sigma-Aldrich**.**

3.1 b- For sensitivity test

Fibrinogen from human plasma 35-65% protein (~95% of protein is clottable)**.**

3.1 c- For antibody–antigen experiment

12-Mercaptododecanoic acid (96%), *N*-Ethyl-*N*′-(3dimethylaminopropyl)carbodiimide (EDC) hydrochloride (98%), *N*-Hydroxysuccinimide (97%,NHS), and albumin from bovine serum (98% , BSA) were purchases from Sigma-Aldrich, affipure mouse anti-human immunoglobulin (IgG) (1.8 mg/ml), affipure goat anti-mouse immunoglobulin (IgG) (1.8 mg/ml) goat anti-rabbit (IgG) were obtained from Sigma Aldrich

3.2- Preparation of core-shell nanoparticle films

The samples shown in fig 3.1and fig 3.2consist of silica or polystyrene (PS) spheres in a size regime from 400 -500 nanometers covered with gold or silver colloid. Alternatively, thin metal films are deposited onto the spheres by thermal evaporation. An optional dielectric layer in between the substrate and the metalized dielectric spheres provides variable separation distance. The preparation procedure takes place in three steps: **first,** deposition of the dielectric layer of different thickness on the substrate, **second,** deposition of the dielectric spheres on the substrate, and **third,** metallization of dielectric spheres with metal by attachment of colloidal nanoparticles or evaporation of thin metal films by physical vapor deposition (PVD).

Schematic drawing for the preparation steps by seeding plating and by evaporating

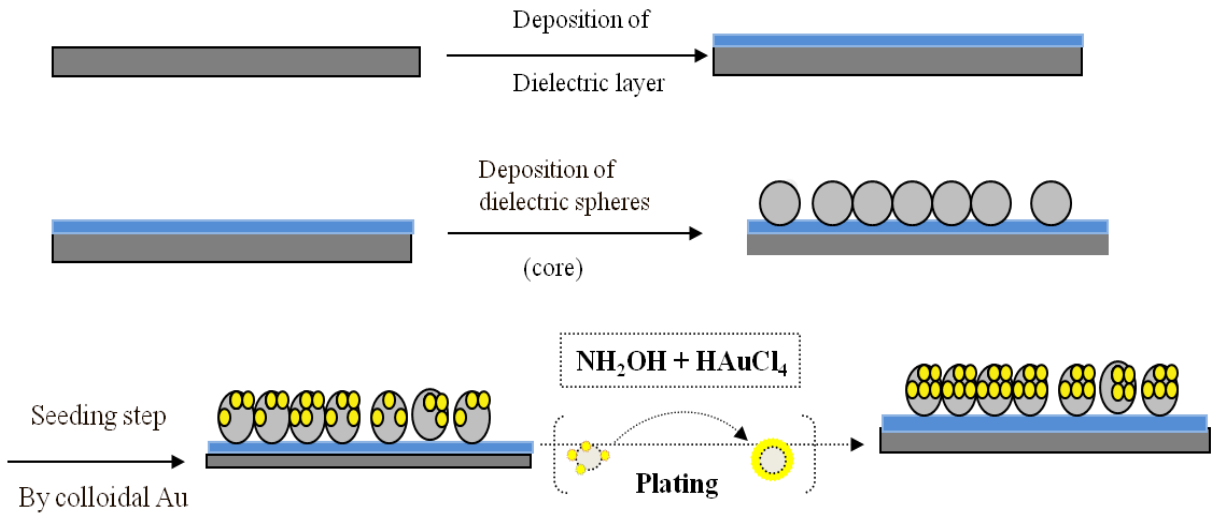

figure 3. 1 *Sample preparation(schematic): Deposition of the dielectric layer on a clean substrate, deposition of the dielectric spheres, and metallization of the spheres with gold colloid and plating step*

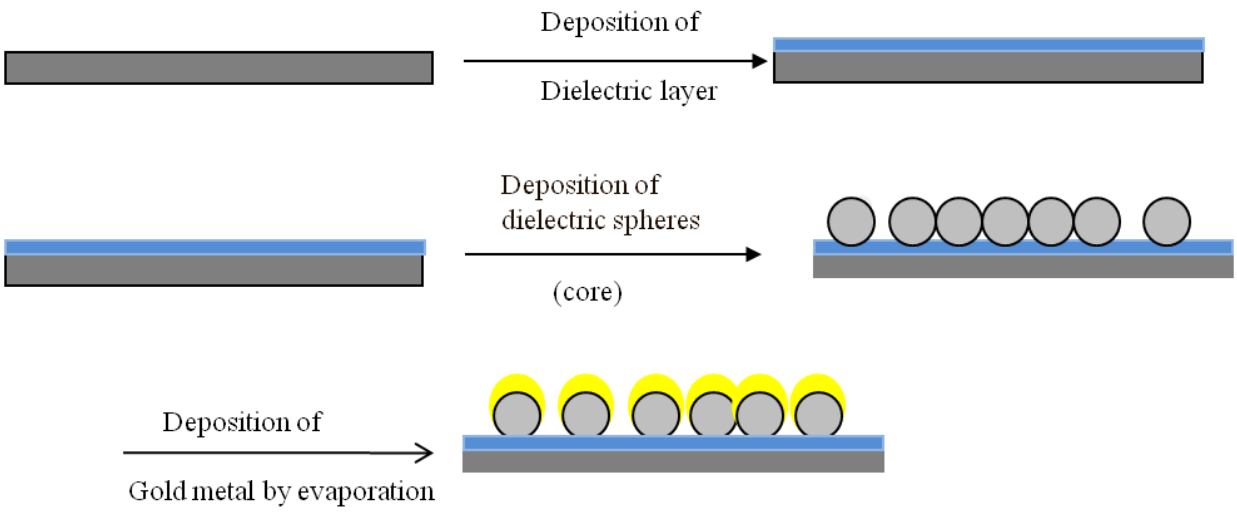

Figure 3. 2 Sample preparation (schematic): Deposition of the dielectric layer on a clean substrate, deposition of the dielectric spheres, and metallization by evaporating gold

3.3- Substrates preparation and cleaning

In these experiments silicon wafers were used as substrates. They were coated with gold by physical vapor deposition (PVD) with a titanium adhesion layer underneath the gold. That the substrates we use are silicon wafer and silicon wafer coated with gold. These substrates were then cut into smaller pieces with a cutter. Before the experiments, the substrates were cleaned by irradiating them with a UV lamp for 2 hours to get rid of organic adsorbates. Afterwards they were rinsed with ultrapure water and dried with nitrogen.

First step

3.4- Deposition of a dielectric layer on the substrate.

Two kinds of dielectric layers have been used to provide separation between the substrate and the metalized dielectric spheres: polyelectrolyte or silicon oxide layers.

3.4.1 The polyelectrolyte layer

The polyelectrolyte thin film was formed by sequential adsorption of polycation and polyanion layers, where layer-by-layer (LbL) deposition occurs by dipping the substrate into solutions of poly (sodium 4-styrenesulfonate) (PSS) and polyallylamino-hydrochlorid (PAH) containing 0.5 mM NaCl for 20 minutes. For each substrate we started with the deposition of polyethyleneimine (PEI) dissolved in water, which is not included in the figure as it only happened once for 20 minutes with 1mg in 1ml pure water at the beginning of the experiment.

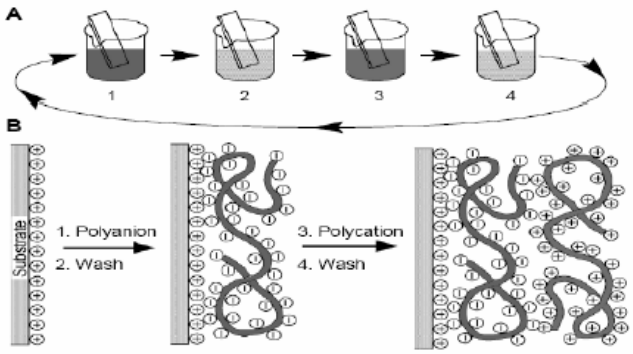

Figure 3. 3 Schematic illustration of the film deposition process using slides and beakers. Steps 1 and 3 represent the adsorption of a polyanion and polycation, respectively, and steps 2 and 4 are washing steps. The four steps are the basic buildup sequence for the simplest polyelectrolyte film [108]

Following the scheme in figure 3.3, a multilayered system PAH and PSS was build up on the PEI coated surface starting from a positively charged layer of PAH (step 1), then rinsing with water (step 2), deposition of PSS (step 3) and then rinsing again with water (step 4). Steps 1-4 are repeated to increase the number of layers in order to provide different separation distance between the substrate and the dielectric spheres. The increase of film thickness with the number of deposited layers is almost linear [109]. The thickness of the polyelectrolyte was measured by ellipsometery.

3.4.2 Silicon oxide/dioxide layer

Silicon oxide/dioxide layers were deposited by sputtering them onto the substrate. Sputtering is a mechanism by which atoms are dislodged from the surface of a material as a result of collision with high-energy particles. Thus, PVD by sputtering is a term used to refer to a physical vapor deposition (PVD) technique wherein atoms or molecules are ejected from a target material by high-energy particle bombardment so that the ejected atoms or molecules can condense on a substrate as a thin film. Sputtering has become one of the most widely used techniques for depositing various metallic films on wafers. In our case, silicon oxide was used as a target. After deposition of the silicon oxide layer, the sample left in air in order to further oxidize. Such fabricated silicon oxide/dioxide films were used as a dielectric separation layer. The thickness of silicon oxide/dioxide layer was measured by AFM

Second step:

3.5- Deposition of the silica or polystyrene spheres on plane, silicon dioxide coated and gold-coated silicon wafers

Different coating methods have been used to obtain close-packed monolayers of silica or polystyrene spheres on a substrate: electrostatic deposition, dip coating, spin coating and floating (fig. 3.4). The latter method is more reproducible than the others and shows a high level ordering in hexagonal structures. Here, we will explain in detail the best results we obtained for these different methods.

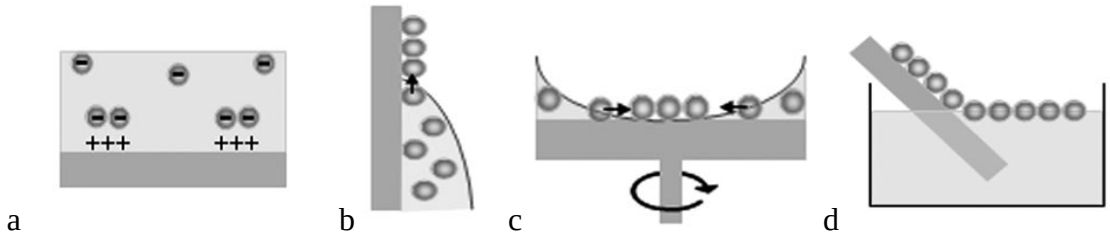

Figure 3.4 Self-assembly strategies for colloid deposition. a, electrostatic deposition of colloid. b, dip-coating. c, spin-coating. d, transfer of a floating particle array to a substrate.[110]

3.5.1 Electrostatic (ionic method) for deposition of silica spheres

Before a monolayer of colloidal particles made from PS or silica is formed on the surface, the corresponding particle suspensions are chemically modified. In case of silica particles deposited on gold-coated substrates, the gold film was covered with a COOH-terminated self-assembled alkane thiolate monolayer adsorbed from a1mM aqueous solution of TG [31]. The tail group deprotonates at neutral pH, thus yielding a negative surface charge. Next, the silica beads were coated with positively charged PEI [111] in order to generate attractive electrostatic forces between the particles and the surface. In case of polystyrene sphere deposition, the spheres were mixed with a proper amount of phosphate buffered 1-ethyl-3-(3-(dimethylamino) propylcarbodiimide (EDC) solution (typically 1–5 mM) at pH 7.4.

Details can be found in [112]**.** Next the substrate was incubated with the respective particle suspension for about 2 h. The suspension is then rinsed off with deionized water, and the surface dried in air, yielding a random close-packed monolayer of colloidal particles. The coverage is irreproducible and the distribution of the spheres random. Fig 3.5 shows low and high magnification SEM images for electrostatic coverage.

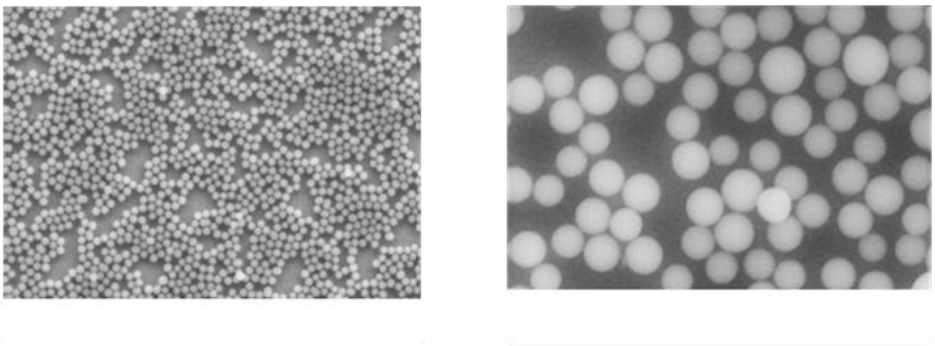

Figure 3.5 SEM picture for electrostatic deposition of silica spheres on a gold substrate.

From the figure random coverage of the dielectric spheres on the substrate is observed, and the interparticle distance is not constant from throughout the surface. This inhomogeneity will cause locally different optical properties of the samples, causing irreproducibility in sensing applications. Therefore, further optimization of the deposition process has been necessary.

3.5.2 Dip coating

In this method the polystyrene/silica sphere colloidal solution was mixed with ethanol in a ratio of 1:2 by volume. Then the substrate is slowly dipped into a beaker containing the solution, and afterwards withdrawn with constant velocity in order to obtain a uniform coating. By adjusting the speed of immersion and withdrawal of the substrate, the coverage of the substrate with spheres can be controlled.

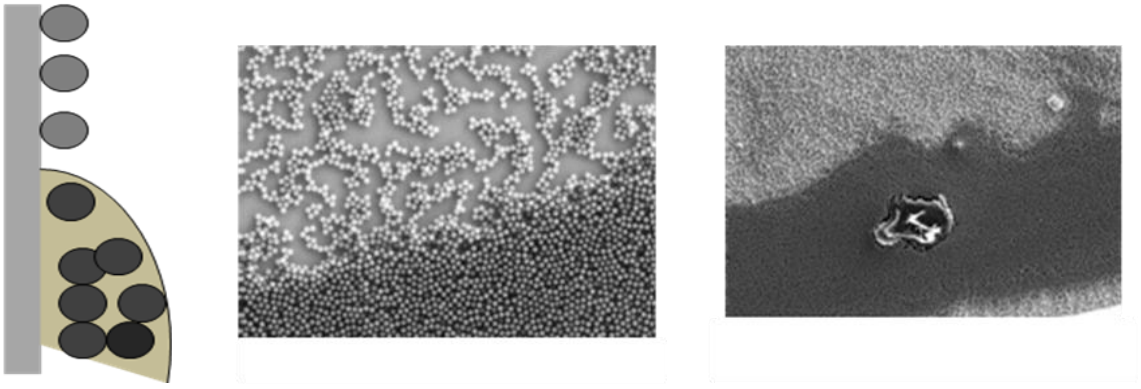

a b c

Figure 3. 6 a. Dip coating process (schematic), b, c SEM pictures for silica spheres deposited on a gold-coated substrate by the dip coating technique

The main disadvantage of this method is that as soon as the substrate is withdrawn, the upper part starts to dry first and the particles accumulate on the lower part of the substrate making it difficult to avoid this gradient-like coverage of the substrate [113]**.**

3.5.3 Spin coating

In the spin coating method an excess amount of colloidal solution is placed on the substrate. The substrate is then rotated at high speed in order to spread the fluid by centrifugal force. Rotation is continued for some time, with fluid being spun off at the edges of the substrate, until the desired film thickness is achieved. The solvent is usually volatile, providing for its simultaneous evaporation (fig 3.7).

Thus by controlling the speed and the concentration of the suspension, one can optimize the sphere coverage.

For the polystyrene spheres, the spin coating process took place as follows: 1 ml of the PS suspension was centrifuged at 2000 rpm for 4 minutes. Excess water was removed and replaced by ethanol p.a. to obtain the initial volume. This step was repeated three times and after the final turn, the colloid was dissolved in 0.2ml of ethanol.

The best coverage of the substrate was obtained by spotting 10 μl of the solution onto the substrate and rotating it with a speed of 4000 rpm for 2 min. However, a hexagonally packed monolayer is formed only in very small areas of the substrate (fig 3.7).

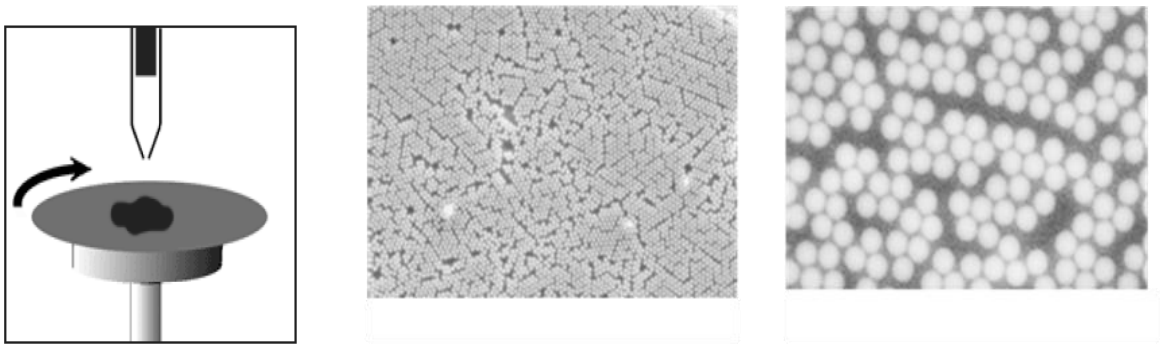

a b c

Figure 3. 7. Schematic setup for spin-coating, b, c SEM picture for polystyrene spheres spin-coated on a gold substrate (low and high magnification).

From the figure we can see high coverage of the substrate, but the distance between the spheres varies laterally which affect the results from place to place on the surface.

3.5.4 Floating method

The floating transfer technique [114-115] is a very simple method and can create compact hexagonal patterns of spheres over large areas on any surface. It has been described for polystyrene spheres and can also be applied to amino-terminated silica spheres. The monodisperse polystyrene or amino-terminated microspheres of 400-500 nm diameters were mixed with an equal amount of ethanol. 3-5 μl of the solution were applied to a glass substrate, that has been previously cleaned in a piranha solution (1:3 30% H_2O_2:H_2SO_4) for 1 hour and then washed with ethanol and milli-pore water to increase its hydrophilicity

The glass substrate was next slowly immersed in a vessel filled with milli-Q water. The particles started to form small islands on the water surface. To form larger islands, 3 μl of 2% dodecylsodiumsulfate solution and about 1μl of a triton-100x/methanol mixture (1:400) were added.

An extended monolayer of spheres with high order was obtained. Such monolayer were lifted off from the water surface using our clean substrate [114] Then the substrate left in air to dry (fig 3.8).

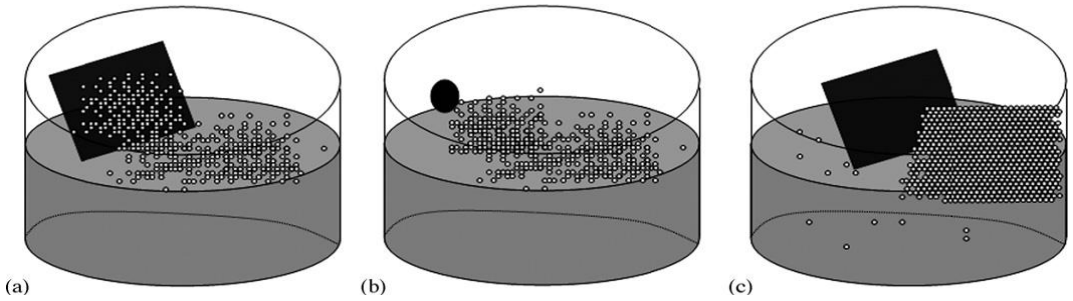

Figure 3.8 The preparation process for monolayer formation of PS spheres on a substrate: Transfer of the particles onto the water surface (a); addition of sodium dodecylsulfate solution to consolidate the particles (b); lift off of the ordered monolayer by the substrate (c).[116]

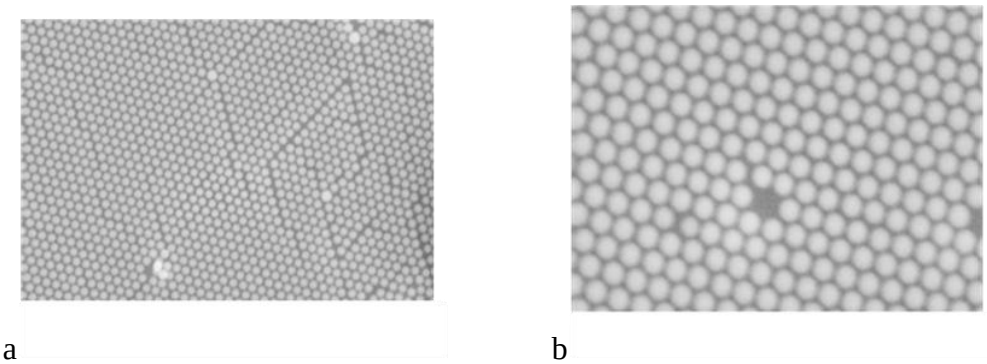

Figure 3.9 a, b SEM images of a self assembled monolayer of polystyrene spheres prepared by the floating method (low and high magnification).

Figure 3.9 a shows a low magnification SEM image, which covers a relatively large area of the self-assembled monolayer. The ordering is reasonably good although point defects and stacking faults are observed in some areas, which may be produced by a variation in sphere size. A closer examination presented in Figure 3.9b shows perfectly ordered arrays with dislocation of one or two spheres.

The same procedure can be performed for amino-terminated silica microspheres. The floating transfer method has been successfully applied in nanosphere lithography for the fabrication of highly regular, 2D arrays of metallic nanoparticles and nanostructures [114] [116]

Third step:

3.6 Metallization of the dielectric spheres

There are two methods to cover the dielectric core with metal, either by evaporation or by seeding and plating. For the seeding/plating approach, we start with the deposition of small metal colloid particles ("seed") and enlarge these particles in the plating step. It is not possible to control the shape of these particles in the plating step, so that spheres, hemispheres or droplet-like particles are generated as we increase their size [117].

For the evaporation method, thin films of metal of given thickness were deposited on the sphere surface by an evaporation process. The evaporator used is home-built and operates at a base pressure of $5 \cdot 10^{-7}$ mbar. Tungsten boats were used for the evaporation of the gold.

3.6.1 Seeding plating technique

3.6.1.1 Seeding of gold and silver

The sphere-coated substrates were kept at 4 °C in a nitrogen atmosphere and incubated for 12 h with a colloidal suspension of citrate-stabilized metal clusters of 3-5 nm diameters ("seeding"). Prior to seeding, the surface of the spheres was modified by PEI (2mg in 1 ml of 0.5M NaCl) for 30 minutes to generate positive charges on the surface. Metal nanoparticles were then dispersed as a monolayer on the PEI-modified substrate by absorption for 12 h. After removal of the solution, the seeding step was repeated**.**

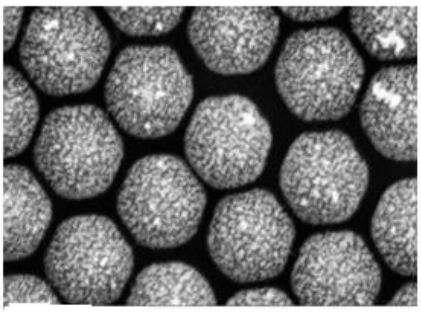

Figure 3.10 SEM image of gold-coated dielectric spheres prepared by applying the seeding technique

3.6.1.2 Plating (growth of the seeded nanoparticles)

Gold

To grow the adsorbed gold nanoparticle clusters into continues metal shell by electrolysis plating; the samples were subsequently exposed to an aqueous solution of 0.1% tetrachloroaurate and 0.04 M hydroxylamine [118-119]. After a few minutes, the substrates were rinsed with Millipore water and dried in a stream of nitrogen. The size of the gold nanoparticles increased with increasing time of plating.

Silver

To grow the adsorbed silver nanoparticle clusters into a continuous metal shell by electrolysis plating, the samples take place as follow the surface was first exposed to aqueous solution of $2x10^{-3}$M of $AgNO_3$ and 150 µl of 37 wt.% formaldehyde (CH_2O) for 10 minutes on a shaker. After 10 minutes the surface exposed to 200µl of 30 wt. % ammonia (NH_3) for 3 minutes and then washed with millipore water and dried in air.

The seeding/plating technique resulted in an incomplete rough metal film on the dielectric core, as seen in Fig 3.11.

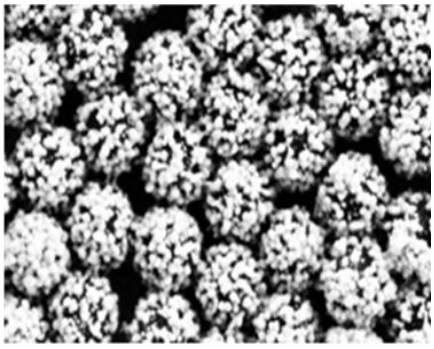

Figure 3.11 SEM image of gold-coated dielectric spheres prepared by the seeding/plating technique with a plating time of 10 minutes.

In this type of synthesis we can control the coverage and the size of the metal spheres by increasing the time of plating. As shown later this will affect the extinction spectra of the nanoparticle-coated substrates.

3.6.2 Evaporation of a thin metal film of different thickness on the dielectric cores

Thin gold films of different thickness were deposited on the spheres by physical vapor deposition (PVD). PVD is a vaporization coating technique, involving transfer of material on an atomic level. It is an alternative process to electroplating. The process is similar to chemical vapor deposition (CVD) except that the raw materials/precursors, i.e. the material that is going to be deposited, starts out in solid form, whereas in CVD, the precursors are introduced to the reaction chamber in the gaseous state.

PVD processes are carried out under vacuum conditions. The process involved four steps: evaporation, transportation, reaction, and deposition. We PVD used for deposition of gold thin films on dielectric spheres as one of the advantages of PVD is that we can deposit materials with improved properties (e.g. reduced metal layer roughness) independent of the morphology of the substrate. Prior to gold deposition, a titanium adhesion layer of 5 nm thickness was evaporated onto the spheres. For this approach, the metal coverage is complete and usually much smoother than in case of seeding/plating.

Fig 3.11 shows a 50 nm thick film of gold evaporated onto the dielectric spheres (fig. 3.12). Due to geometric shielding effects, the lower part of the spheres remains uncoated (cap-shaped metal shell structure).

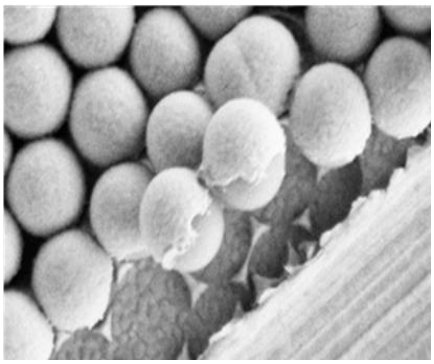

Figure 3.12 PVD of a thin gold film onto a substrate coated with dielectric spheres.

3.7 - Sensitivity test

The samples were tested for their sensitivity towards molecule adsorption by exposing them to a fibrinogen solution (1mg/ml in PBS buffer, pH 7.4). Sensitivity was determined by measuring the wavelength shift of the resonance peaks in response to adsorption of fibrinogen onto the surface. Fig 3.13 shows typical shifts of the resonance peaks upon adsorption to fibrinogen.

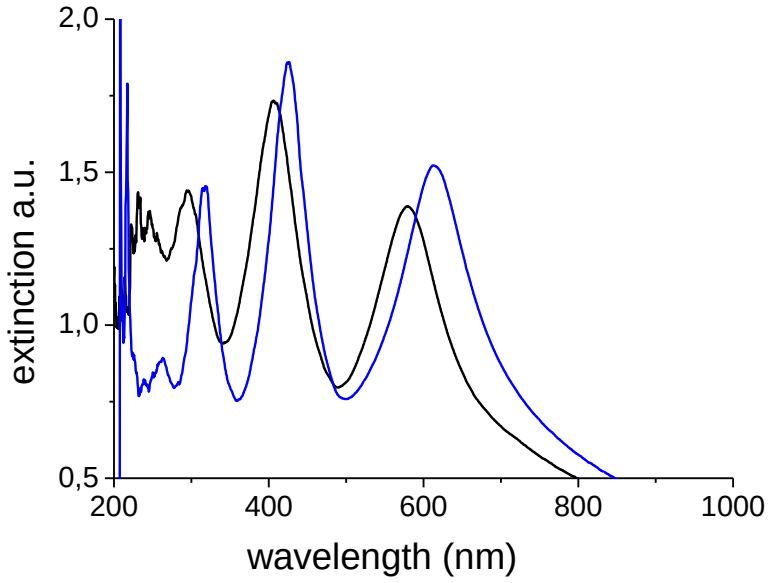

Figure 3.13 Typical shift in the resonance peaks upon adsorption of fibrinogen (black line: before protein adsorption, blue line: after protein adsorption)

From the figure it is observed that the resonance peaks red-shift upon adsorption of fibrinogen. The peak in the 400-550 nm regime shifts about 16 nm and the peak in the of 550-800 nm regime about 31 nm, which allows us to detect the analyte at two or more different wavelengths at the same time on the same spot.

3.8- Antibody-antigen interactions

As a biological application we tested our optically responsive surfaces for their potential in detecting antibody-antigen interactions. The experiments are performed as follows:

For activation the surface the sample was first exposed to a 0.5 mM 12-mercaptododecanoic acid solution in pure ethanol, overnight.

After the surface was rinsed with ethanol and dried in a stream of nitrogen it was activated by a mixture of 50 mM EDC and 10 mM NHS in 100 mM phosphate buffer of pH 6.0 (mixture of monopotassium phosphate and dipotassium phosphate pH 4.0 bring to pH 6.o with 1M NaoH) for 30 min. Finally, the substrates were washed with Millipore water.

For covalent coupling of IgG to the surface the sample was immediately incubated in 1 ml of buffer (pH 8.0) (mixture of monohydrogen phosphate pH 9.0 and hydrogen chloride) containing 20 μl of mouse anti-human immunoglobulin (IgG) overnight on a shaker. Then the sample was washed with a copious amount of water and then immersed in PBS on a shaker for 10 min.

These washing steps were repeated three times. In the experiments described in the following, the immobilized mouse anti-human IgG serves as the antigenic component.

For the study of specific antibody binding, the sample was first incubated for I hour in 3 ml of 10 mg/ml BSA in PBS to reduce non-specific IgG/surface interactions. Then 10 μl of goat anti-mouse immunoglobulin (IgG) were added to the solution and the sample was left overnight on a shaker. Finally, it was washed with a copious amount of water and immersed in PBS on a shaker for 10 min. The washing steps were repeated three times.

For the study of unspecific antibody binding we exposed another sample first to BSA and then to goat anti-rabbit (IgG) following the above procedure.

3.9 Equipments

The optical properties of the samples were investigated with UV-Vis spectroscopy and scanning electron microscopy.

3.9.1 Optical characterization

The surface was characterized by means of a fiber-optical set-up operated in reflection mode figure 3.14.

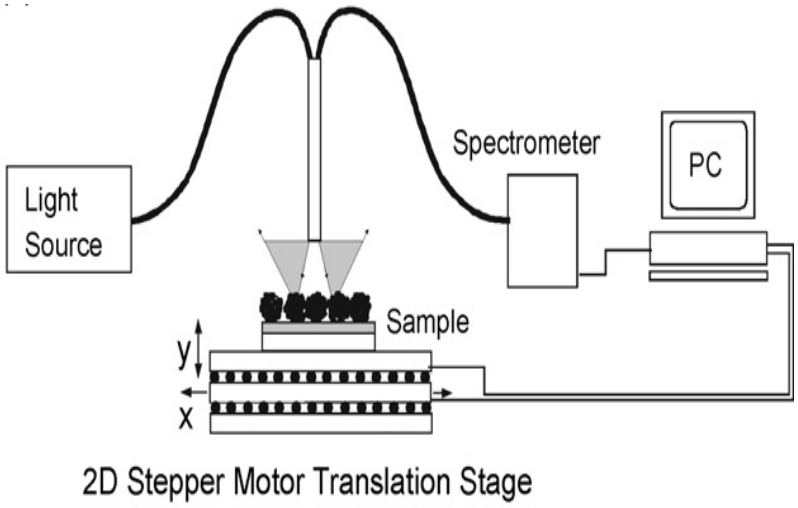

Figure3. 14 Set-up for automated spectrally resolved measurements, here showing the commercially available reflection probe with approximately 3 mm lateral resolution in combination with a home-built computerized translation stage [31]

The surfaces were illuminated by DH-2000 Deuterium Tungsten Halogen lamp (type, company) which combines the continuous spectrum of deuterium and tungsten halogen light sources in a single optical path. This lamp generates a bright, broad-range light spectrum. The light reflected from the surface was collected via a second optical fiber and analyzed with a miniature spectrometer (HR2000, Ocean Optics) equipped with a diode array and operating in a spectral range from 200 to 1100 nm. In these experiments a commercial fiber reflection probe (R200-7, Ocean Optics) with a spot diameter of about 3 mm was used.

3.9.2 SEM Characterization

SEM measurements were performed using a Zeiss Leo 1530 system for ex-situ measurements at room temperature and a pressure lower than 10^{-5}mbar. The electron beam was accelerated with a voltage of 10 kV. In this thesis, numerous SEM images were used to display the topography of the Samples after the deposition of the dielectric spheres as well as after the coverage of the gold or silver colloidal. All these images were recorded with a LEO1530 Gemini electron microscope using the secondary electron detector. The EHT (Electron High Tension), which is the accelerating voltage, was set to 3 kV. For working with SEM, the surface needs to be conductive to prevent charging of the sample due to electron irradiation. For this purpose, non-conductive substrates were coated with a conductive layer of carbon or a thin silver layer before use.

3.9.3 Ellipsometric measurements

Ellipsometry measurements were performed on the spectral ellipsometer M 44 (J. A. Wollam Co.) at a fixed angle of incidence of 75°. A xenon lamp which provides a wide range of wavelengths was used as a light source. In our work, we are more interested in the film thickness. The thickness of the thin film coated on substrate was obtained from the ellipsometry measurements. To have reliable statistical results, all the samples were measured three times at different spots and the averages were calculated

Chapter 4

4- Results and Discussion

4.1 Introduction

In this work we combine the effect of localized surface plasmon resonance with reflectometric interference to develop an improved label-free optical biosensor. The biosensing mechanism is based on changes in the absorption properties of such structures in response to biospecific interactions. As mentioned before, the nanoparticle-coated substrates show resonance peaks in different wavelength regimes yielding different sensitivity values for the same analyte measured at the same spot. This allowed us to demonstrate the effect of wavelength on the sensitivity of the sensor. We observed that the higher sensitivity of LSPR and interferometric responses to analytes was obtained for the 600- to 900-nm regime in agreement with [26]. The optical properties of these substrates prepared were investigated with UV-Vis spectroscopy and scanning electron microscopy to investigate the morphology of the samples. As no direct theory exists to explain the optical properties of such structures, the discussion will focus on experimental results and observations. However to study the optical properties of such combination was a challenge as the complexity of our system results in a lot of different factors that affect the position, broadening, and sensitivity response of the peaks. The most series problem we faced was the reproducibility of sample preparation. For example, if we want to study the effect of gold coverage we should be able to guarantee equal coverage of the substrates with dielectric spheres as their coverage will affect the result as well. That is why we spend some time to control the coverage of the dielectric spheres.

The most reproducible method we found was transferring the spheres by a floating method. However, we still observed small differences in the results from sample to sample, which may be due to dislocations or multilayer deposition of one or two spheres. This problem has been overcome by repetition of the experiments and averaging.

The second major problem we had was the deposition of gold nanoparticles not only on but also in between the dielectric spheres in the metallization step. Such gold nanoparticles will affect the results of the study as they contribute to the optical properties of the system.

However, we tried to overcome this problem by reducing the effect of the substrate [32, 120]. For this purpose, we deposited a thin dielectric film in between the substrate and the metalized spheres and obtained improved sensitivity for an optimum layer thickness.

In this thesis we first study the reflection spectra of dielectric spheres on the substrate before deposition of metal onto the spheres to impact on the presence of the reflected mode due to multibeam interference and to determine the effect of metal deposition on the peak position and sharpness. We start the metallization with spherical gold nanoparticles of small size (3-5 nm), then we grow these particles to investigate the effect of increasing the metal coverage of the nanoparticles and to obtain the optimum coverage for enhanced sensitivity as well as. Another goal of the study was to directly compare the effect of metal coating composition by comparing gold and silver nanoparticles.

The aim of the thesis was to develop a biosensor with high response to bimolecular adsorption using human fibrinogen as a model protein. We measured the sensitivity of the peaks in the wavelength range between 400-900 nm. In this regime two peaks exist, one between 400-600 nm and the other between 600-900 nm. In general we observed that the peak shift for the peak in range from 600-900 nm is higher indicating a higher sensitivity to adsorption of fibrinogen. This may be due to the fact that the gold nanoparticles have a larger negative dielectric function at higher wavelengths so that the sensitivity for gold-coated substrates is higher in the near IR.

4.2 The reflection interference spectra of the dielectric spheres on different substrate

Numerous methods for the production of colloid monolayer have been proposed in the literature, [121-123]. In case of our application, the 2D spheres arrays must be made into large, defect-free, perfect arrays with precise control of the symmetry and the interparticle distance as this will highly affect the results. The organization process should also be simple and fast, and the quality of the arrays must be reproducible. This is the case for the floating transfer technique as already detailed in chapter 3, the other preparation techniques tested yield lower quality surface in terms of coverage and homogeneity. As shown in fig 4.1

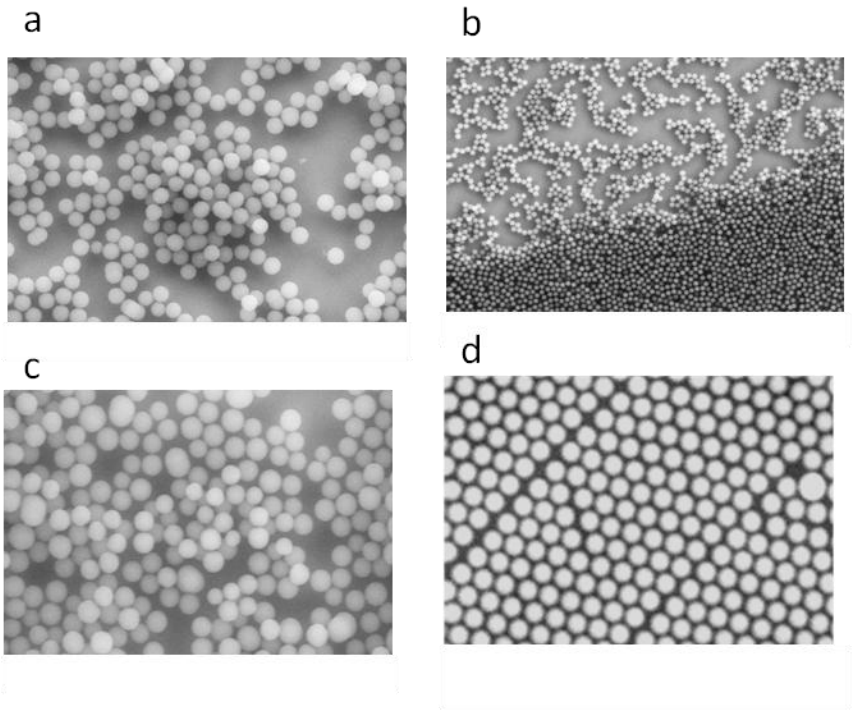

Figure 4. 1 Typical surface coverage for silica nanospheres deposited by a- electrostatic method b- dip method c- spin coating d- the floating-transfer method.

From the SEM image of the sphere-coated substrate with different method we found that the floating transfer method is the most reliable method for our study as it is the most reproducible method it is seen that the distance between the spheres are small enough to avoid scattering of light. We measure UV-Vis spectrum of the floating coverage on different substrate, the measurements for the samples were referenced to a sample, which is the same substrate but without the dielectric spheres

Fig 4.2 shows the reflection spectra of hexagonal monolayers of amino terminated silica particles deposited on a blank and gold-coated silicon (100) wafers. The diameter of the dielectric sphere is about 500 nm, and the metal layer thicknesses 30 nm, 100 nm, and 200 nm. As shown in the figure multiple resonance peaks are observed due to the interference of the beams multiply reflected between the substrate and the surface of the sphere. Where the coherence conditions are satisfied as the diameter of the spheres are about 500nm [25]

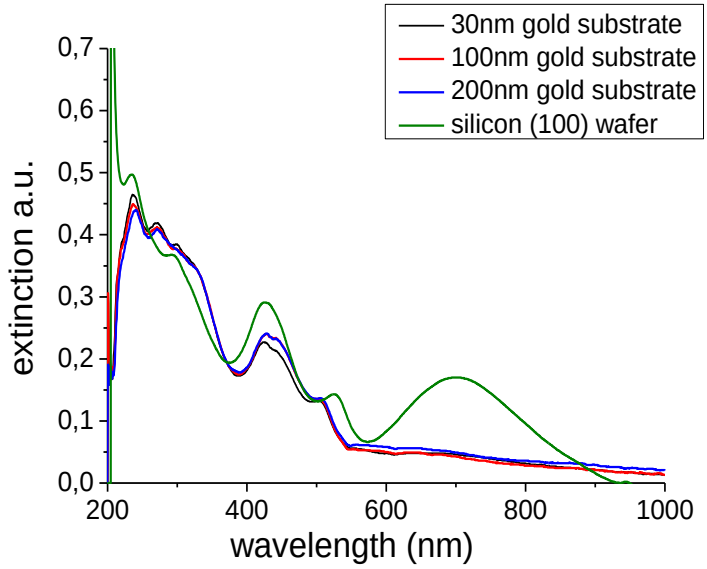

Figure 4.2 Reflection spectra of hexagonally packed dielectric spheres on different substrates

In case of metalized substrates the reflection spectra are almost the same for different thickness of the gold layer with higher intensity in case of 200 nm gold thickness, which is due to enhancement of the reflectivity at such higher thickness, the lower intensity in case of wavelength range 600-900 is due to the high reflectivity of gold substrate at high wavelength for the incident light. For the silicon substrate the interference peaks are more pronounced yielding higher intensity especially in the wavelength range of 600 – 900 nm. The dielectric spheres spectrum on silicon substrate was fitted before [124] for polystyrenes spheres by using finite-difference time domain (FDTD) method [124] with slightly different peak positions probably due to the non-perfect structure of the nanoparticle layer.

4.3 Metallization of the dielectric spheres

As mentioned before two methods have been used to metalize the dielectric spheres either by a seeding/plating technique or by evaporation of thin films of gold onto the dielectric spheres**.**

4.3.1 Seeding plating technique

4.3.1.1 Seeding

Polyethylenimine (PEI) was used to modify the surface of the substrate-bound dielectric spheres with positive charge to allow for electrostatic interaction between the spheres and the negatively charged metal nanoparticles (seeding process). Fig 4.3 shows the SEM images for dielectric spheres coated with gold nanoparticles of 3-5 nm in size.

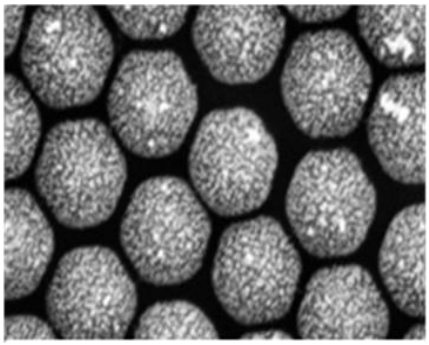

Figure 4.3 SEM image of substrate-bound dielectric spheres with small gold nanoparticles attached by the seeding technique. The size of the good nanoparticle is 3-5 nm, and the substrate was exposed to the gold colloidal solution for 48 hours

From the SEM images we found that the cores are not completely covered by gold nanoparticles, and some of the gold particles are deposited on the pores formed in between the spheres, which we believe it could reduce the sensitivity of the system. After deposition of the gold nanoparticles onto the dielectric spheres, the samples constructed of plasmonic gold nanoparticles and dielectric spheres deposited on a substrate presented interference plasmonic signals which are called interference localized surface plasmon resonance (iLSPR) [22-23].

Fig 4.4 shows the reflection spectra before and after deposition of gold nanoparticles.

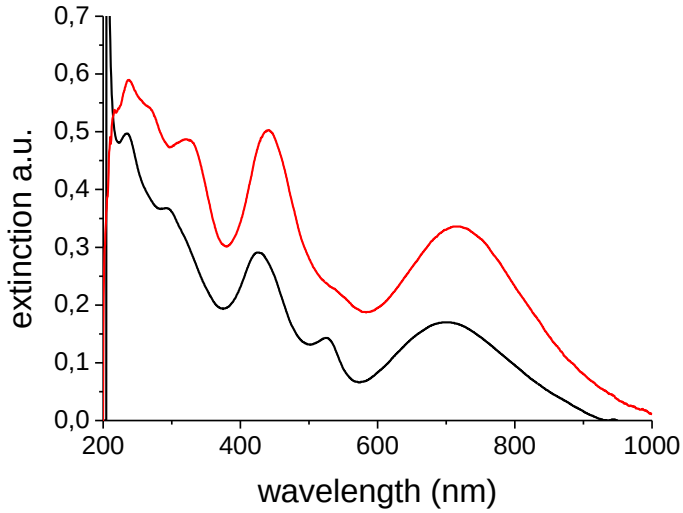

Figure 4. 4 Effect of small gold nanoparticles attached to the surface of the dielectric spheres deposited on a non-metalized silicon substrate (red line) compared to dielectric spheres on the same type of substrate without gold nanoparticles (black line).

From the figures it is observed that the gold nanoparticles increase the intensity of the peaks as well as narrowing them [23] in comparison to the case of dielectric spheres without gold nanoparticles. Actually, we expected the peaks to be even sharper but due to the inhomogeneity of the gold coating, the line bandwidths are broaden and the position of the peaks are slightly red shifted due to presence of gold nanoparticles that change the refractive index of the surface of the sphere and, thus, its reflectivity. The combination of metal nanoparticles and dielectric spheres with size satisfy the coherence condition [30-31] has proven to yield high wavelength shift upon analyte adsorption and enable such samples to be used as biosensors [19, 29-31].

4.3.1.2 Plating (growth of gold nanoparticles)

The technique for enlarging the gold nanoparticles is their growth in gold salt solutions using hydroxylamine. [125-128] thermodynamically, hydroxylamine (NH_2OH) is able to reduce Au^{3+}ions to metallic Au. However, this reaction is highly accelerated by the presence of gold surfaces. For example, when gold — in solution or immobilized on a surface — is exposed to an aqueous solution of Aucl_4 and hydroxylamine, the Au^{3+} ions get reduced by the hydroxylamine and the resulting metallic gold goes into the growth of the existing nanoparticles completely. Nucleation of new particles in solution does not take place. Applying this technique to gold nanoparticles on the surface of dielectric spheres, deposited on a substrate, will result in larger gold nanoparticles and, therefore, smaller gaps between the particles. As mentioned before, we attached small gold particles of nearly spherical shape with 3-5 nm diameters to PEI-treated dielectric spheres. These sites were then used as nuclei to induce shell growth. It should, therefore, be possible to control the shell thickness by changing the time of reaction. Thus, we can tune the metallization from an incomplete shell to a continuous coverage by increasing the time of plating.

The SEM images of fig 4.5 show the dielectric sphere coverage as a function of plating time. Starting with isolated small gold particles, these gold particles increase in size but are still isolated in the beginning. Later on, these particle grow in diameter, coalesce, and connect to each other forming a surface that can be described as a continous one.

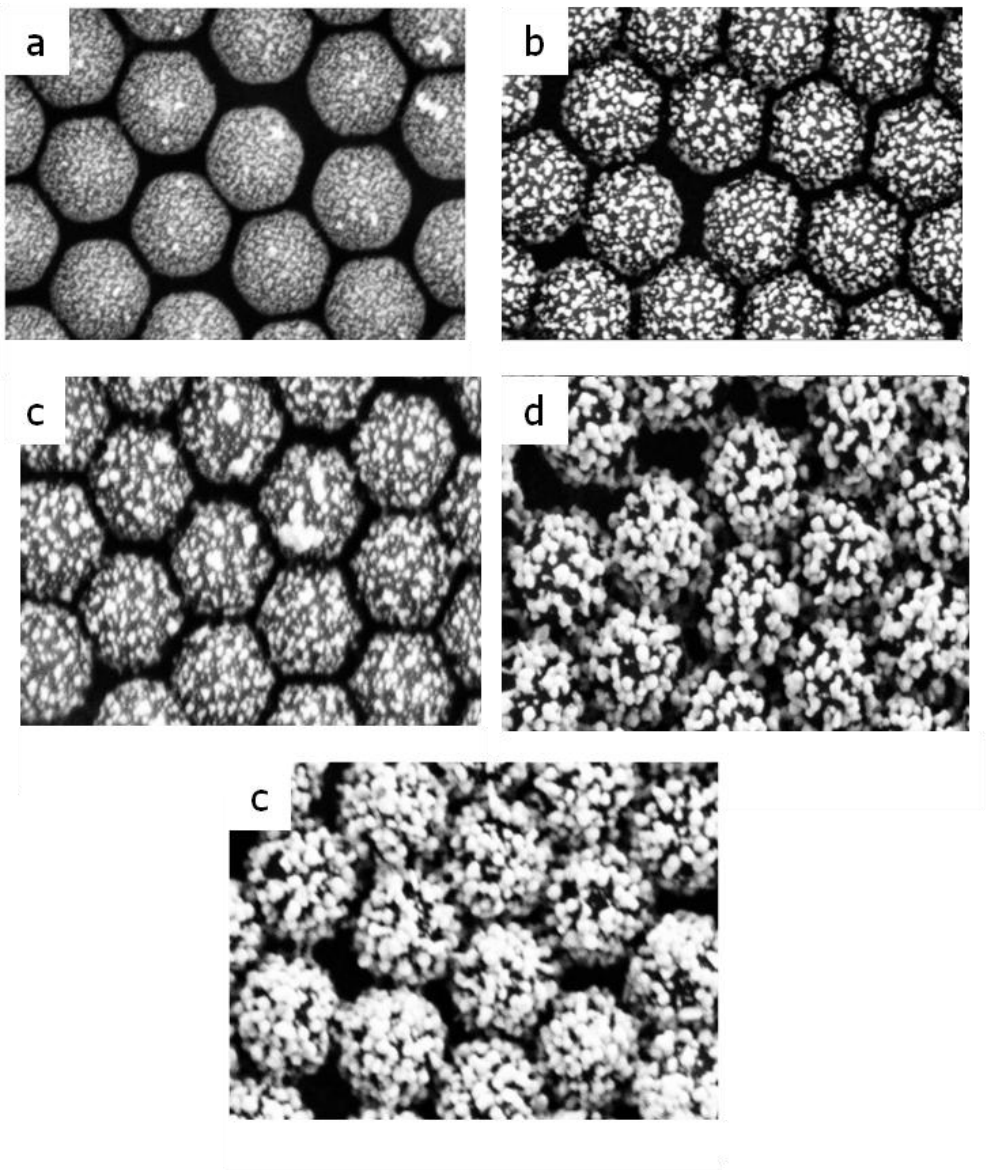

Figure 4. 5 *SEM images of gold nanoparticles grown on the PEI-treated dielectric spheres as function of plating time (0, 1, 3, 5, and 10 minutes as shown in a, b, c, d, and e, respectivily).*

The UV-Vis spectra for the samples are referenced to a substrate without the dielectric spheres. By increasing the time of plating we notice enhancement in the intensity of the peaks up to 10 minutes, as well as slightly red shift with increasing growth time of the plating as shown in fig. 4.6.

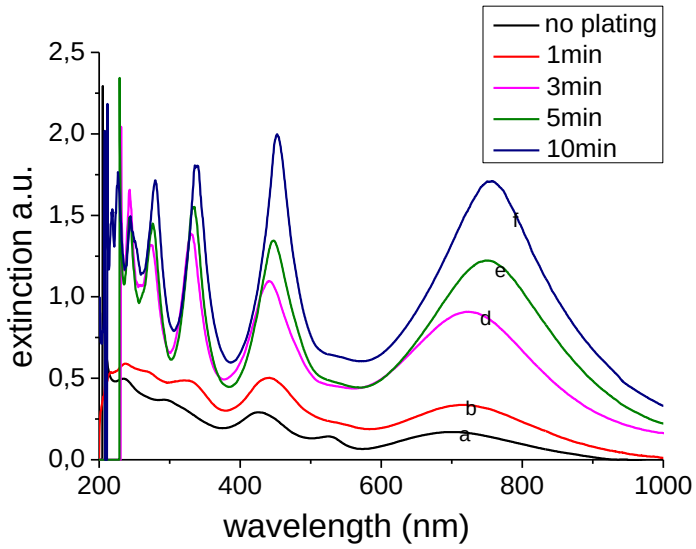

Figure 4. 6 the optical *effect of increasing the plating time on the reflection spectrum, where the samples were plated for 1, 2, 3, 5, and 10 min., after seeding)*

The general trend of Halas group study for metal nanoshell can be summarize as follow: when the metal shell thickness of the dielectric core increase a blue shift in the particle`s plasmon will occur. However this only true with two conditions:

First if uniform gold layer is present on the surface of the dielectric core [129] which is not our case as we have incomplete shell coverage.

Second in case of small diameter of the dielectric core in quasistatic limit or dipole limit with diameter 2r less than the wavelength of incident light as at such size only the dipole plasmon resonance is excited. Since all the electrons of the particle experience the same phase of the incident electromagnetic field, which is also not our case.

We have the diameter of the dielectric core comparable to the wavelength of the incident light, that the metal shell core in such mesoscopic size loss the tunibility property of the metal shell core that known for size less than wavelength of light[130], as the light unable to polarize the whole metal shell sphere at such size and they observed the excitation of higher-order multipolar Plasmon modes.

With the multipolar Plasmon modes appearing at shorter wavelengths than the dipole Plasmon feature in the particle's overall extinction spectrum. Since the excitation of higher-order modes occurs when the phase of the optical field varies across the spatial extent of the particle, they are also known as phase retardation effects. Phase retardation also gives rise to significant red-shifting and broadening of the dipole resonance.[131-132] In our study we found the existence of these multipeaks before deposition of the gold nanoparticles on the dielectric spheres where we consider it due to interference between reflected beams between lower and upper part of the dielectric spheres. With increasing the size of the gold nanoparticles on the surface of the dielectric spheres we didn't dedicate any increase of the multipeaks occur due to interference, however we observe increase in the intensity of the peaks along with slightly red shift in the peaks position as reported in [117] in this case we can treat metal shell as gold nanoparticles grow on substrate where three factor affect them change in shape from spherical to random shape and lateral and vertical increase in size randomly as well as decrease in the distance between the gold particles which increase the interaction between them[73] [117].

The fact that the metal particles grow in vertical as well as lateral direction will affect the spectra as the vertical thickness increase will decrease the inner and outer interaction in the metal shell, which will blue shift the resonance peaks [133] is not applicable anymore.

Thus, we have in this system coupling between small gold nanoparticles on dielectric spheres as well as coupling between covered spheres.

Therefore, the resulting spectrum is a complex superposition of the optical properties of the metalized dielectric spheres as whole, and effects of decreasing optical gap with increasing cluster size, in addition to the contribution to the gold nanoparticles that are deposited on the substrate in between the metalized spheres.

The peaks are getting sharper as there is a strong dependence of the plasmon bandwidth on the size of the metal particles[134] as in fig 4.6.

However we can describe it as follow: as the nanoparticle size is increased, the number of electrons increases in direct Proportion to the volume, as the extinction of the particle increases with volume as from equation

$$C_{ext} = \frac{24\pi^2 r^3 \varepsilon_d^{3/2}}{\Lambda(\varepsilon_d+2\varepsilon_m)^2+\varepsilon_i^2}$$

Where $C_{ext}$the extinction coefficient, r is the radius of the particles ε_i is the imaginary dielectric constant of the metal

The enhancement of the intensity of the peaks can be explained by the Drude-Sommerfeld model, where we have seen in chapter 2 that

$$\varepsilon = 1 - \frac{\omega_p^2}{\omega^2+i\gamma^2} \qquad 4.1$$

The plasmon frequency $\omega_p = \left(\frac{4\pi n_e e^2}{m^*}\right)^{\frac{1}{2}}$ depends on the electron density n_e and m_*, the electron effective mass, e is the electron charge and γ is the electron collision frequency or the phenomenological damping constant of the bulk material.

In the case of a perfectly free electron gas and in the limit of $\boldsymbol{\gamma \ll \omega}$ equation 4.1 become simpler

$$\varepsilon = 1 - \frac{\omega_p^2}{\omega^2} \qquad 4.2$$

For small nanoparticles we have a low electron density as the nanoparticle size is increased, the number of electrons increases in direct proportion to the volume, because of which the extinction of the particle increases from equation 4.2 and as we increase the size of the metal particles the enhanced electron density results in sharper peaks.

However, for larger particle size the density of the electrons increases further to polarize all the electrons homogenously leading to retardation and reduction instead of enhancement of the peaks.

In addition, as the particle size increases, there is increased radiative damping, i.e. emission of radiation by the plasmon oscillations, which results in an increase in the scattering contribution, but also reduces the plasmon lifetime (increased plasmon line width) [80, 135] as we see in case of increasing the plating time to 23 minutes (fig 4.7).

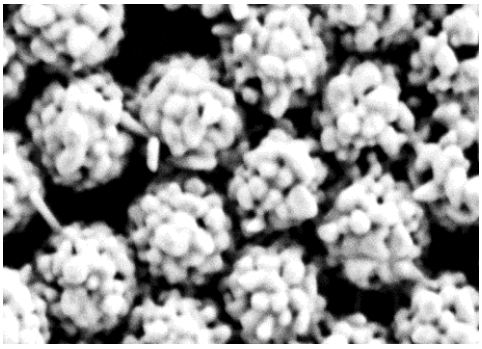

Figure 4. 7 SEM image of hydroxylamine grown AuNP on the PEI treated dielectric spheres the time of hydroxylamine growing is 23 minutes

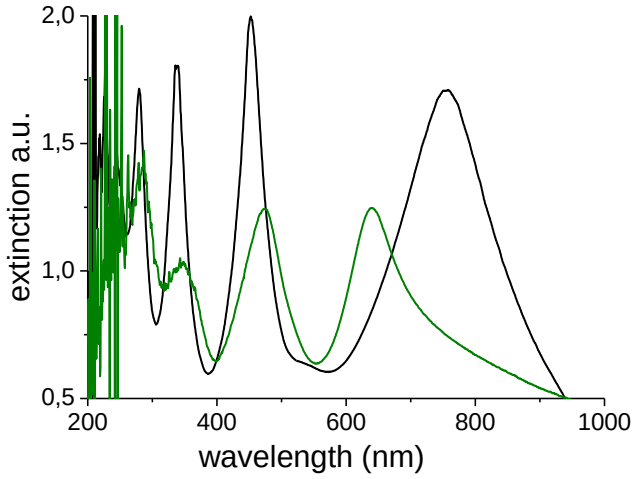

Figure 4.8 Uv Vis spectra for increase in plating time the intensity starts to drop again and the peaks blue shift for higher thickness of the metal shell with growth (green line) time 23 mins In comparison with shell growth of 10 mins (black line)

Fig 4.7 shows the SEM image of the gold coverage for a plating time of 23 min. The coverage can be referred to as continuous but still rough, as seen in the SEM image the gold nanoparticles grow and form a rough continuous coating on the dielectric spheres.

The increased thickness of the metal particles decreases interaction as the particles get very close to each other [73] [136]. In addition to the retardation effect (due to the increased number of electrons that are not polarized), which affects the distance between the peaks, also the distance between the metal shells is decreased and the pores between the dielectric spheres are partially closed. All these effects result in a blue shift of the peak position in the wavelength range 600-900nm and red shift for the peak in range 400-600 nm which mean that the distance between the two peaks in the wavelength range change with high thickness of the metal shell and a drop in the intensity of the spectra, which affects the sensitivity as we will see later. In general, the field enhancement or reduction depends strongly on the surface morphology and precise shape of the roughness features at the metal surface.

4.3.2 Sensitivity measurements

We checked the sensitivity of the plasmonic interference substrate for different size of the gold nanoparticles as generated the plating method. In the experiments we found that the sensitivity of the peaks in the range from 400 - 900 nm towards molecule adsorption decreases with increasing nanoparticle size. Figures 4.9 and 4.10 show the peak shift for substrates coated with small gold particles of 3-5 nm in size which corresponds to seeding without plating, and the sensitivity decrease nearly exponentially with increasing the time of plating where this result remind us with the case where we have in case of quasistatic metal shell limit observe an exponential decrease in the field enhancement with increasing the shell thickness as reported by El sayed group. They prove that such exponential decay in the field enhancement are the universal for the shell increasing thickness as well as increasing the gap distance between two metal particles. Such decay is independent on the size or the shape of the two particles; however it has proven recently that for very close distance between the particles we have reduction in the field rather than enhancement.

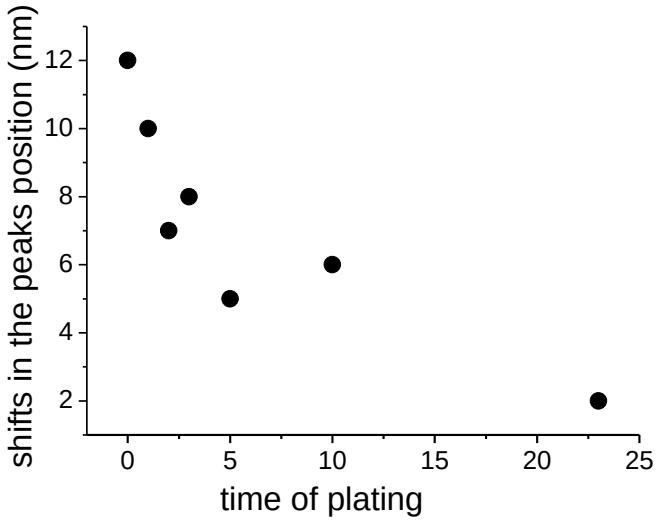

Figure 4.9- Shift of the peak position in the wavelength range from 400-600 nm upon fibrinogen adsorption for different times of plating

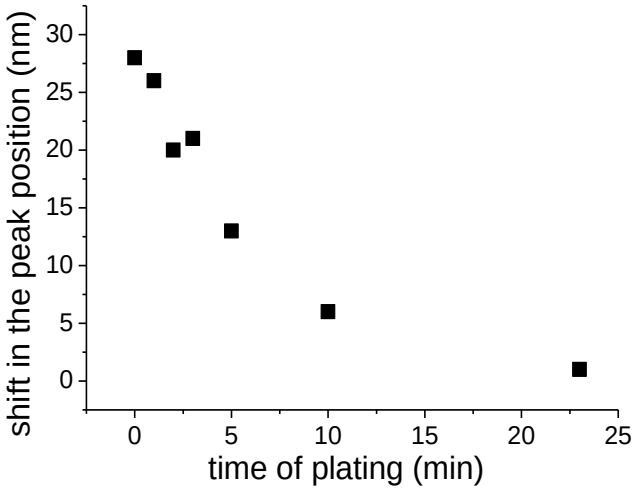

Figure 4.10- Shift of the peak position in the wavelength range from 600-900 nm upon fibrinogen adsorption for different times of plating

We will now discuss the observed effect from different points of view. It is clear that by increasing time of plating the gold nanoparticles grow and approach each other. Also, the distance between the metal shells is reduced and the interparticle plasmon coupling in the nanoshell arrays produces intense near-field enhancements at the junctions between neighboring nanoshells, and creates uniform periodic densities of hot spots for surface-enhanced spectroscopes, means that we have an enhancement in the electric field in between the spheres.

At the same time we grow the particles vertically, which increases the shell thickness and, thus, decreases the interaction between the inner and outer shell. In addition, there is one more effect to consider: By increasing the gold particle size on the two-dimensional array of dielectric spheres, the hot spots between the dielectric spheres are blocked[137]. It has shown that high surface area porous materials, especially those with resonant spectral features such as porous silicon waveguides, provide increased sensitivity compared to conventional sensor platforms with limited surface area [138]. All these effects determine the optical response of our samples and as a whole decrease the sensitivity with increasing size of the gold nanoparticles coverage on the dielectric spheres.

The arguments are completed by [28] where the authors introduce a new term, which is the hotspot volume defined as the volume inside which the electromagnetic field enhancements are large. A large hotspot volume means that a larger number of molecules can be probed and the hotspot volume usually depends on the shape of the particles. Fig 4.11 [28] shows the increase of hotspot volume with increasing ratio of gold nanoparticle distance (d) to the size or the diameter of the nanoparticles (D) which can describe our results qualitatively.

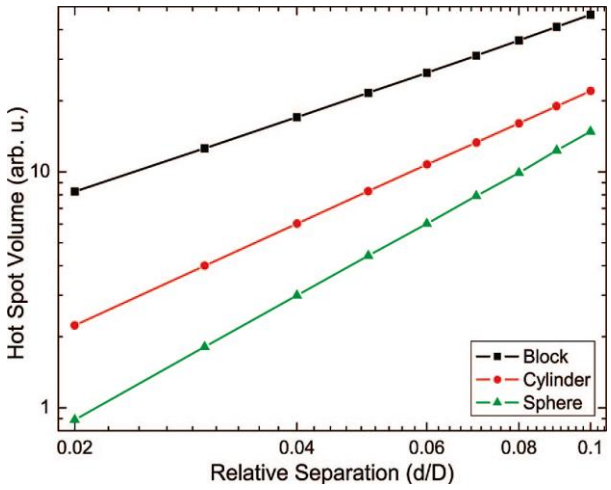

Figure 4.11 Hotspot volume V_H as a function of relative separation d/D for 2D square arrays of block-, cylinder-, and sphere-shaped particles [28]

Fig 4.11 shows that the hot spot volumes for block array are larger and less dependent on relative separation than that of sphere arrays with cylinder arrays in between [28]. Where from figure 2.9 the field enhancement decrease exponentially with d/D .

The previous definition of the sensing volume give us the feeling that our result is not unreasonable as we see enhancement in the intensity with increase the gold nanoparticles size till 10 minutes plating and at the same time we notice decrease in the sensitivity.

4.4 Effect of changing the interparticle distance between the dielectric spheres

Although the peak positions of interference plasmons are not changed much by increasing the size of the gold nanoparticles on the dielectric spheres, we found that we can tune these peaks by change the coverage from hexagonally closed-packed to random coverage. Fig 4.13 shows SEM images of dielectric polystyrene spheres on a gold-coated substrate covered with gold nanoparticles. The plating time was 3 minutes to yield a reasonable profile. In general, polystyrene sphere layers are more connected and the average distance between the dielectric spheres is small compared to silica sphere films.

Fig 4.12 schematically shows the coverage with gold nanoparticles in case of hexagonally close packed and randomly adsorbed dielectric spheres. In case of random adsorption the amount of gold nanoparticles deposited directly on the substrate is higher than that in case of close packed coverage.

Figure 4.12 Sketch of the nanoparticle coverage for the case of hexagonally close-packed and randomly adsorbed dielectric spheres

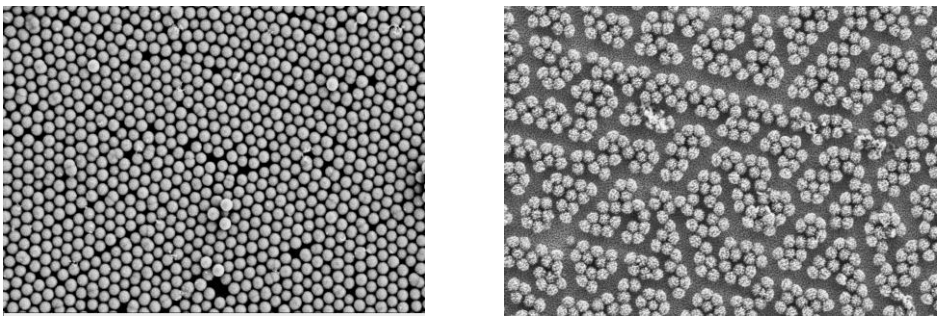

Figure 4.13 SEM images of hexagonally close-packed and randomly adsorbed polystyrene spheres of 400 nm diameter deposited on a gold-coated substrate

From the UV-Vis spectra (fig 4.14) for these two kinds of coverage we found that when the distance between the metalized spheres is random and, thus, on average increased the peak positions blue shift and broaden.

This is due to the fact that the field enhancement drops when increasing the distance between the metal shells [139]. However, a detailed interpretation of the spectral shifts observed is more complicated as a higher number of gold nanoparticles are directly deposited on the substrate for random sphere adsorption because the mean distance between the metalized spheres increases (see figure 4.12). This may also affect the position of the peaks, as the gold nanoparticles aggregate, interact with the substrate and, therefore, contribute to the resonance peak - usually inducing a red shift.

Also the interaction of such gold nanoparticles on the substrate depends on the type of the substrate used, as it expected to be different for silicon substrate as the interaction between metal nanoparticles on metal substrate are different on that of nonmetal one.

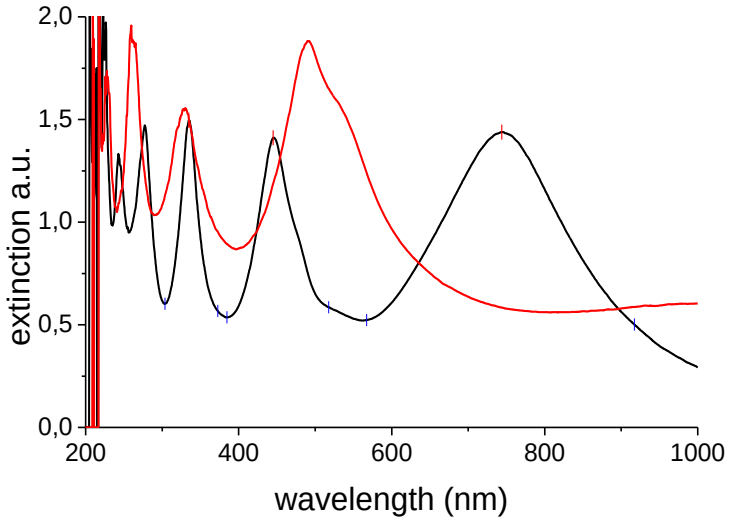

Figure 4.14 UV-Vis spectra for closely packed films (black line) and random coverage (red line) of metalized polystyrene spheres on gold-coated substrates.

4.4.1 Sensitivity measurements

As we have seen, the effect of increasing the mean distance between the metalized spheres results in a blue shift and slight broadening of the peaks [140]. As the distance between coupled metal shell increases however, still have gold nanoparticles on the plane substrate in between the metalized dielectric spheres that contribute to the resonance. The sensitivity of the samples listed in table 4.1

Condition	Wavelength shift for peak 400-600 nm	Wavelength shift for peak 600-900 nm
Random adsorption of the dielectric spheres	6-8 nm	13-15 nm
Closely-packed dielectric spheres	12 nm	29 nm

Table 4. 1 *Wavelength shift for closely-packed d back dielectric coverage and random coverage*

From table 4.1 we found that there is a drop in sensitivity in case of random coverage i.e. increased distance between the metalized dielectric spheres. This due to presence of an enhanced number of gold nanoparticles on substrates with random sphere adsorption, which will decrease the sensitivity as reported in literature [32, 120].

In general the sensitivity of the metal shell is higher than that of metal nanoparticles directly deposited on the substrate [141]. In this case, the higher shell area in case of closely-packed spheres would be the cause of enhanced sensitivity (refer to the comparison of core/shell nanoparticles and simple metal nanoparticles later)

4.5 Substrate effects

As mentioned before we also studied substrate effects on the reflection spectra using silica spheres of 500 nm diameter on both silicon substrates and gold-coated substrates of different metal film thickness (30, 100, and 200 nm). It was found that for the non -metalized spheres the peak positions do not change much, neither for the gold-coated surfaces of different metal film thickness nor for the silicon wafer substrate. However, for the silicon substrate the intensity of the peak at 600-900 nm is higher than for the gold-coated substrate due to the constant value of the refractive index of the silicon substrate in the UV-Vis range. After metallization step we found out that due to the pores between dielectric spheres, gold nanoparticles fill these pores which make difference between metal substrate and silicon wafer substrate, cause a red shift in the peaks in case of gold substrate. As an electromagnetic interaction occur between the metal nanoparticles and the metal substrate. According to electromagnetic theories of a spherical particle placed close to a metal surface, there exists a special type of electromagnetic normal modes, called 'gap modes', which are strongly localized in the space between the metal sphere and the metal surface. They cause a significant red shift of the resonance peak of the metal nanoparticles on metal substrates[142].

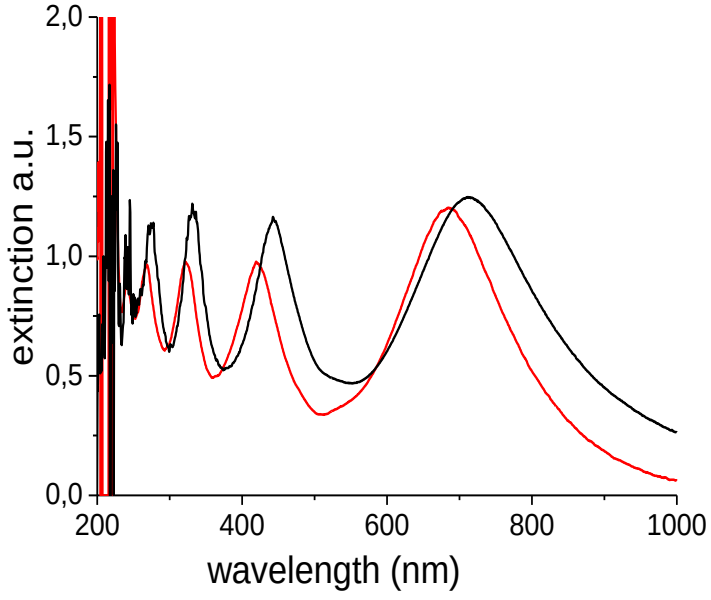

Figure 4.15 Comparison of the extinction spectra of metalized silica spheres (seeding + 3 min. plating)deposited on a metal-coated substrate (black line) and on a blank silicon wafer (red line). For the metal-coated substrate the peaks are shifted.

Fig. 4.15 show a comparison between the optical spectra of metalized spheres deposited on gold-coated substrates and a blank silicon wafer. A red shift is observed in case of the gold-coated substrate due to interaction between localized surface plasmons (excited in the metal nanoparticles) and propagating plasmon (excited in the metal film). This interaction will also affect the intensity of the peaks. In case of gold-coated substrates with different layer thickness, there was no significant change in the peak positions as seen in figure 4.16.

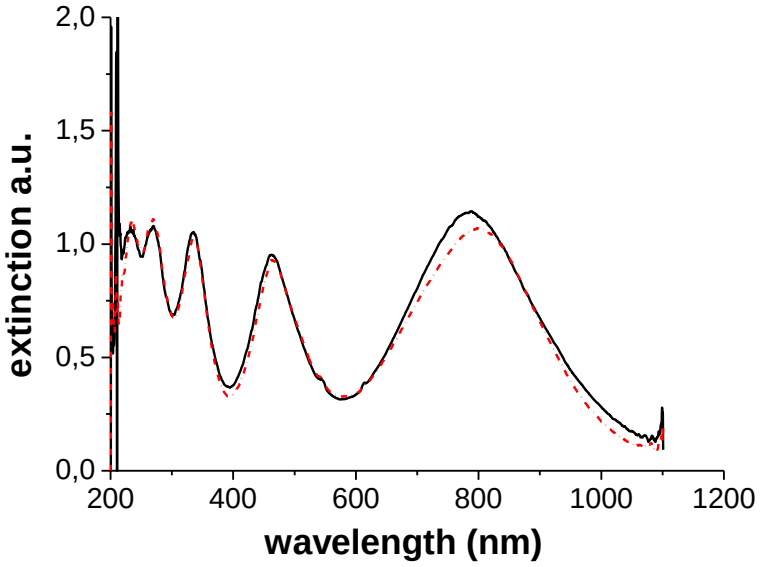

Figure 4.16 UV-Vis spectra for metalized silica sphere on a 30 nm gold-coated substrate (red line) and a 100 nm gold-coated substrate (black line)

From the fig there is slightly red in the position of the peaks for the case of 100 nm gold substrate.

4.5.1 Sensitivity measurements

We measured the sensitivity of metalized spheres (seeding + 3 min. plating) on metal-coated substrates of different film thickness and a blank silicon wafer substrate. The results are summarized in table 4.2.

Material	Wavelength shift for peak at 400-600 nm	Wavelength shift for peak at 600-900 nm
30 nm gold	12 nm	29 nm
100 nm gold	11 nm	31 nm
200 nm gold	13 nm	26 nm
Silicon wafer	16 nm	33 nm

Table 4.2 Wavelength shifts upon fibrinogen adsorption for metal-coated silica spheres on different substrates: gold-coated substrates of different film thickness and a blank silicon wafer

From the table we observe that in case of the silicon wafer the sensitivity is higher than in case of the gold-coated substrates, although the peak intensities are higher for the gold coated substrates. The sensitivity for different thickness of the gold thin film is almost the same.

The only slight increase in sensitivity in case of the silicon indicates that the sensitivity of our system is not significantly affected much by kind of substrate used whether metal or not. In case of the metal-coated substrates the gold nanoparticles that exist in the pores in between the dielectric sphere give chance to direct coupling between the localized surface plasmons (in gold nanoparticles) and the surface plasmon on the metalized substrate. The overlap between the fields may reduce the sensitivity [32, 120]. However, in our case the effect is limited as the amount of gold nanoparticles in the pores is comparatively small due to the fact that the dielectric spheres are closely packed.

4.6 The effect of metal shell composition (silver and gold)

Despite that gold and silver have the same bulk plasmon frequency due to their similar electronic densities as seen in chapter 2, spectral region with sharper band than gold nanoparticles. We, therefore, replaced gold nanoparticles on the dielectric spheres by silver. For almost the same coverage of the of the dielectric spheres with gold and silver nanoparticles, figure 4.17 shows an increase in the intensity of the peak in the wavelength region 380-500 nm for a silver metal shell. The bandwidth of the peak is small and its position coincides with the absorption band for silver nanoparticles in solution [54]. Also, a significant red shift and enhanced intensity is observed for the peak in the wavelength range from 600-900.

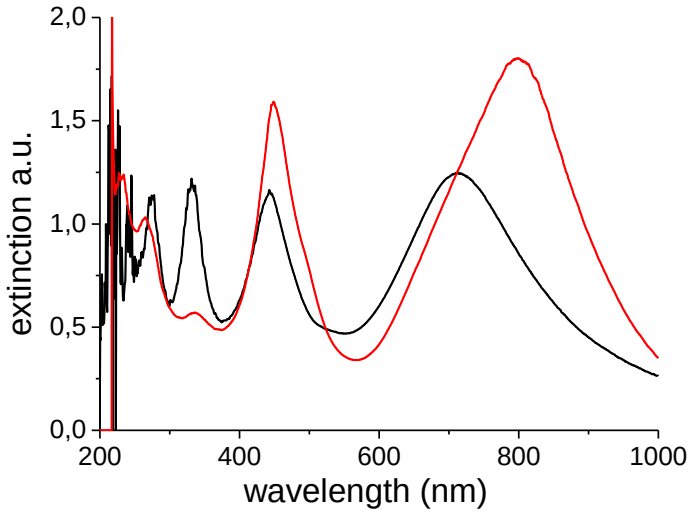

Figure 4. 17 UV-Vis spectra for silica spheres on a gold-coated substrate covered with gold (black line) and silver (red line) nanoparticles (seeding + 3 min. plating in both cases)

4.6.1 Sensitivity measurements

As shown in table 4.3 the sensitivity of the silver-coated substrates is very high for the wavelength range from 400-600 nm compared to that of substrates coated with gold-nanoparticles. In the wavelength regime from 600-900 nm the differences are comparatively small.

Material	Wavelength shift for peak 400-600 nm	Wavelength shift for peak 600-900 nm
Gold substrate/gold nanoparticles	12 nm	29 nm
Gold substrate/silver nanoparticles	48 nm	34 nm

Table 4. 3 Sensitivity of silica spheres deposited on gold-coated substrate and covered with gold and silver nanoparticles (seeding + 3 min plating) both the coverage of the substrate with dielectric cores and the coverage of the cores with metal nanoparticles is almost identical.

From the viewpoint of materials selection, the dispersion of the real part of the metal dielectric function plays a key role in the response of the SPR peak position to the refractive index change of the surroundings. In contrast, the imaginary part of the dielectric function of the metal has a dominant effect on the relative contribution of optical scattering and absorption to the total extinction. Thus, the fact that the silver real dielectric constant in the wavelength range of 400-600 nm has higher negative values than that of gold yields a higher sensitivity for silver in that regime.

4.7 Effect of material of the dielectric core

In this experiment we made a direct comparison between the silica and polystyrene spheres. A problem in the experiments is that the there is about 30 nm difference in the diameter of silica (540nm) and polystyrene (510nm) spheres which are commercially available. This will limit the accuracy of the comparison.

However, as a general observation, the coverage of the substrate with polystyrene spheres is always higher than in case of silica spheres (85% vs. 75%).

Also, in case of polystyrene the spheres are more connected to each other so that the amount of gold nanoparticles that exist in between the pores are less than the case of silica spheres in addition to the effect of the dielectric constants that are different for polystyrene and silica spheres. Fig 4.15 show a comparison between polystyrene spheres and silica spheres coated with gold nanoparticles on a silicon wafer substrate.

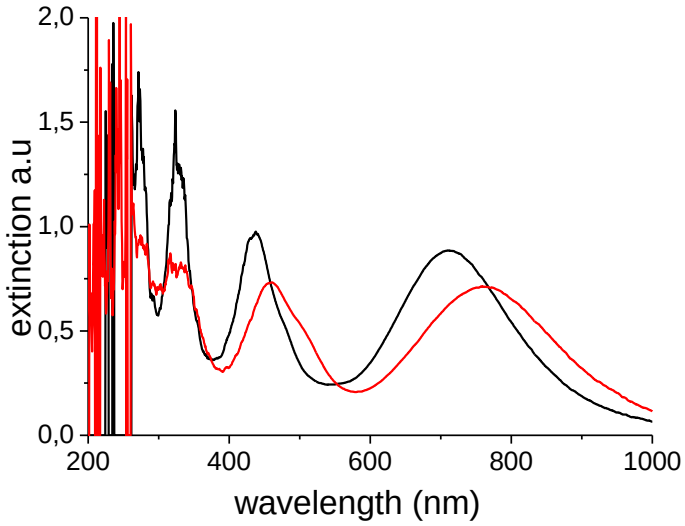

Figure 4.18 UV-Vis spectra for polystyrene spheres of diameter 510nm (black line) and silica spheres of diameter 540nm (red line) both coated with gold nanoparticles.

As there are many different aspects to consider, it is difficult to interpret the differences in the spectra in detail. However, as a general result we observe that the peaks for polystyrene are always sharper than that for silica. The blue shift in case of polystyrene spheres may be due to the size of the spheres which 30 nm smaller than the silica spheres.

4.7.1 Sensitivity measurements

The sensitivity difference for silica and polystyrene spheres shown in table 4.4

Core material	Wavelength shift for peak 400-600 nm	Wavelength shift for peak 600-900 nm
Silica spheres of 540 nm diameter	12 nm	29 nm
Polystyrene spheres of 570 nm diameter	11 nm	32 nm

Table 4. 4 Sensitivity of silica and polystyrene sphere coated substrates with the same gold nanoparticle coverage

From the table we observe only a slight difference in sensitivity for the peak wavelength range from 600-900 nm.

4.8 Onion structures

The structure we examine here are silica spheres deposited on a gold-covered substrate and multiply coated with alternating sequences of dielectric and metallic layers ("onion structure"). The dielectric layers were formed by polyelectrolyte deposition (PEI, 2mg in 1ml of a 0.5M NaCl solution), the metallic layers were prepared by seeding gold nanoparticles onto the spheres. The polyelectrolyte thickness measured on flat surface is about 1 nm. Up to 4 pairs of dielectric/metallic layers were prepared onto the cores.

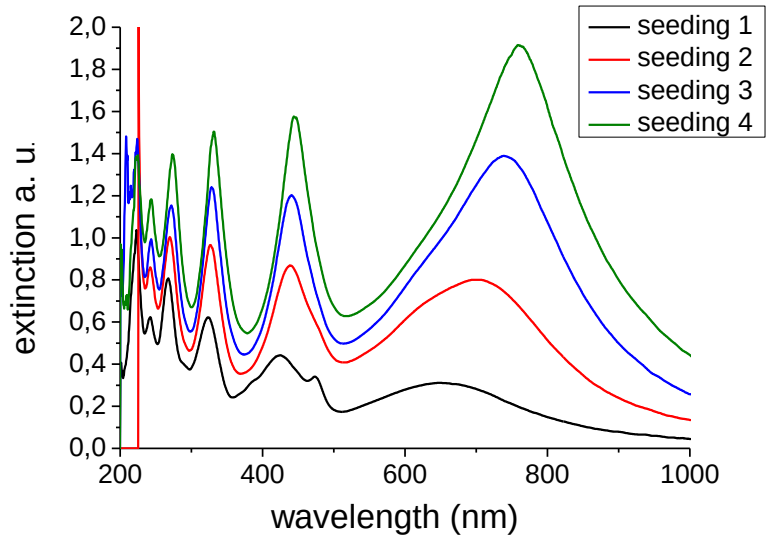

Figure 4.19 UV- Vis spectra for surface-bound silica spheres coated with sequences of metallic and dielectric layers ("onion structure")

From fig 4.19 we see that the intensity of the peaks increases and that the peaks red shift upon increasing the number of layers. In comparison to the case of growth of gold on the surface of the spheres, we have in case of onion structures a smoother coverage of the dielectric spheres only for seeding Moreover, the presence of dielectric layers in between the gold particles reduces the symmetry of the metalized spheres which show a red shift with respect to the case of symmetric nanoshells [143].

The red shift for these seeded samples is larger than for the case of grown gold nanoparticles (plating). This may be due to the fact that for conventional samples (i.e. without multiple dielectric/metallic layers) pinhole structures are generated in between the gold particles in the seeding process and by plating these holes increase in thickness and decrease in diameter. In case of onion structure we effectively cover the whole surface. Fig. 4.20 shows the SEM pictures for onion-type structures after 1x seeding and the last seeding. For comparison, fig. 4.21 shows the case of seeding and 5 min. plating for conventional samples.

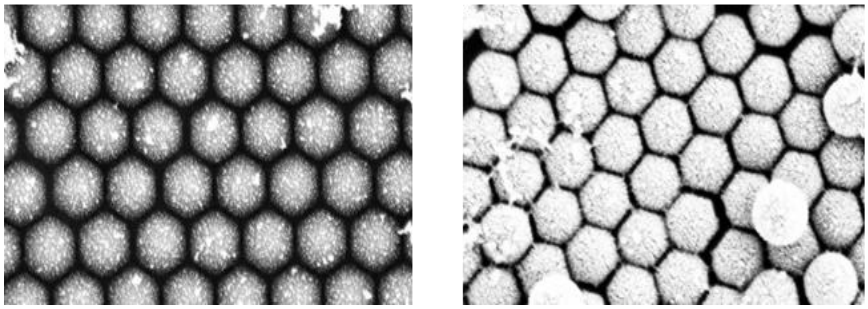

Figure 4.20 SEM images of onion-type structures after 1x seeding for 12 hours (left) and after 4 seeding steps with PEI deposition in between each seeding step.

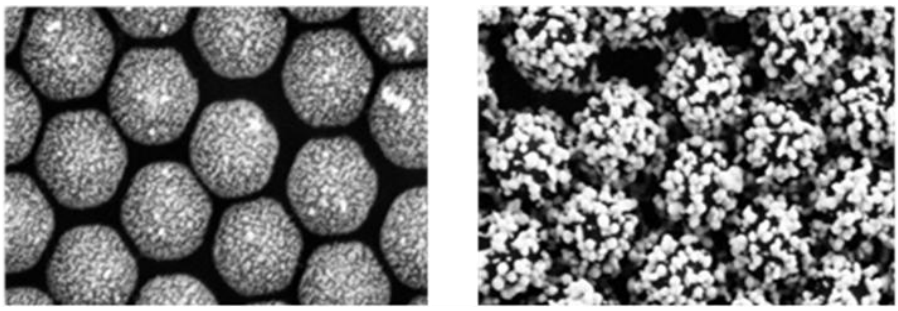

Figure 4.21 SEM images of conventional core/shell structures after seeding (left) and 5 min. plating (right).

From the figures the rougher structure and existence of pinholes in case of conventional samples compared to the case onion structures becomes evident

4.8.1 Sensitivity measurements

Table 4.5 shows the sensitivity for onion-type structures after the fourth seeding process with PEI layers in between the gold nanoparticles. The sensitivity is decreased compared to conventional samples.

Conditions	Wavelength shift for peak 400-600 nm	Wavelength shift for peak 600-900 nm
After the fourth coverage	4 nm shift	*5 nm shift*

Table 4.5 Sensitivity for the onion-type structures after deposition of the fourth dielectric/metallic layer.

4.9 Core-shell nanoparticles vs. colloidal nanoparticles

We also studied the difference between the interference resonance of substrates coated with planar thin films and dielectric sphere monolayers. The thickness of the thin films was selected close to the diameter of the dielectric spheres in order to be able to compare the optical response of the two configurations. In this experiment we used a 350 nm silicon oxide/dioxide layer which is the maximum thickness we can deposition on gold substrate. Afterwards, we deposited gold nanoparticles on the silicon oxide/dioxide layer by seeding and 3 min. plating, and compared the interference resonance with that of substrates coated with commercially available polystyrene spheres of 390 nm diameter using the same metallization procedure. Fig 4.22 shows SEM images of the gold nanoparticle coverage on plane and sphere-coated (i.e. curved) substrates

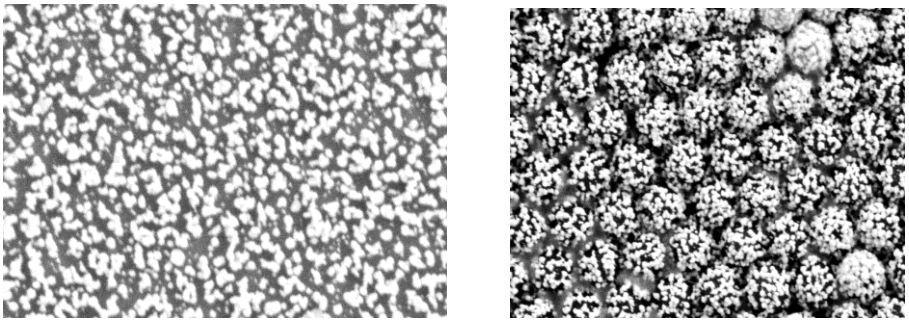

a b

Figure 4.22 SEM image of gold nanoparticle coverage for planar thin dielectric layers of 350nm thickness (a) and dielectric polystyrene spheres of 390 nm diameter (b).

From the UV/Vis spectra (fig 4.23) we observe that in case of planar thin dielectric films the peaks are sharper and more pronounced than for the case of dielectric sphere monolayers. A higher number of peaks is observed in case of dielectric spheres, which may be attributed to the fact the diameter of the spheres is about 40 nm larger than the thickness of the planar silicon oxide/dioxide layer. In general, the number of resonance peaks increases with increasing the thickness of the dielectric layer or the diameter of the dielectric spheres.

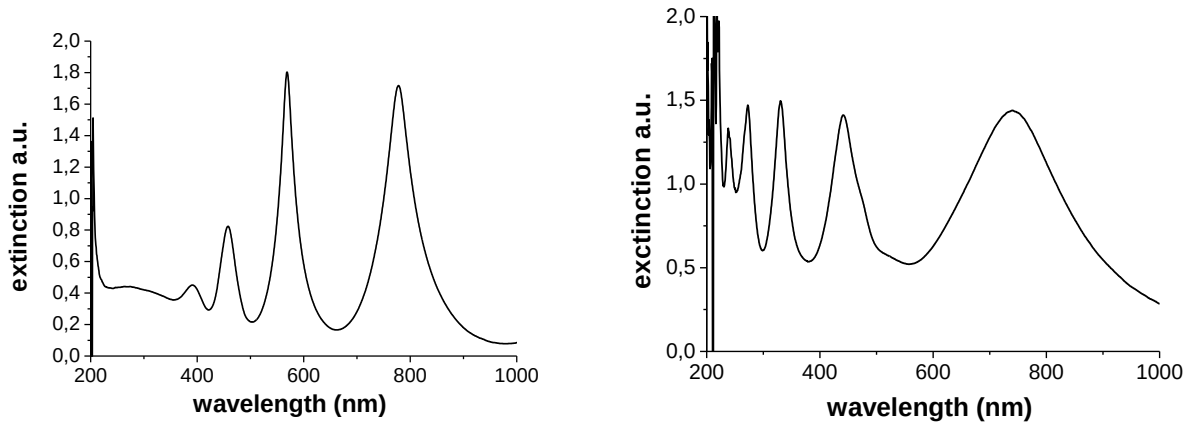

Figure 4.23 UV/Vis spectra for planar dielectric films and dielectric sphere monolyers coated with gold nanoparticles.

4.9.1 Sensitivity measurements

It is known that in general the sensitivity of metal shell structures is higher than the of metal nanoparticles citations!. In our case we compare two plasmonic interference systems. The results show that the sensitivity of the metalized dielectric spheres is higher than that of metal nanoparticles on planar dielectric layers despite the fact that in the latter case there are no gold particles directly deposited on the gold-coated substrate. However, the results match with [144] where it is shown that high surface area porous materials provide increased sensitivity compared to conventional sensor platforms with limited surface area

Conditions: Gold nanoparticles on	Wavelength shift for peak 400-600 nm	Wavelength shift for peak 600-900 nm
Polystyrene spheres with 390 nm diameter	10 nm	26 nm
Silicon dioxide film of 350nm thickness	3 nm	7 nm

Table 4. 6 Sensitivity of planar dielectric films and dielectric sphere monolayers coated with gold nanoparticles.

From the table we find a drop in the sensitivity in case of planar dielectric films compared to spherical core which may be attributed to the fact that in case of dielectric spheres we have high field concentration in between the spheres, and that the sensitivity of metal shells on dielectric spheres is higher than that of gold nanoparticle on planar substrate in general.

4.10 Effect of introducing dielectric layer in between metal substrate and metalized silica spheres.

In this part we study the effect of introducing a planar dielectric layer in between the metal substrate and the metalized spheres to minimize the effect of the substrate and to increase the reflectivity of the substrate. However a lot of study have been made to obtain a maximum coupling between metal substrate and gold nanoparticles by introducing a dielectric spacer between them we get this effect in case of our metal dielectric spheres with an optimum thickness of dielectric spacer even we get same response on nonmetallic substrate which means that this maximum coupling at such optimum thickness due to field modulation caused by the dielectric spacer itself and independent on whether the substrate are metal or nonmetal and also whether we have metal nanoparticles or metal shell.

The goal was to identify an optimum thickness to improve the sample response. Surface-supported particles suffer an intrinsic drawback compared to particles in solution, as the fixed refractive index of the supporting substrate will reduce the overall refractive index sensitivity of the particles[46].

The effect of the underlying substrate on the sensing capabilities has been a recurrent subject in recent nanoplasmonic sensing studies [80, 120, 145-146] and found to decrease the response of the nanoparticles to the change in the dielectric environment [147]. In our studies, two kinds of dielectric separation have been tested: polyelectrolyte and silicon oxide/dioxide layers.

4.10.1- Polyelectrolyte layers

Self-assembled polyelectrolyte films were formed by alternating adsorption of polycations and polyanions in aqueous solution on a silicon wafer substrate. The number of layers was varied in order to provide different separation distance between the substrate and the dielectric spheres. Samples composed of 1, 3, 5, 7, 9, 11, and 13 layers were prepared.

The layers had the structure PEI$(PSS-PAH)_1$, $PEI(PSS-PAH)_3$ and so on, i.e. PEI$(PSS-PAH)_n$. n is an odd number as we start with PEI deposition as mentioned in chapter 3.

Fig 4.24 shows the relation between the number of layers and the thickness of the polyelectrolyte film, where the thickness of the layers was measured by ellipsometry

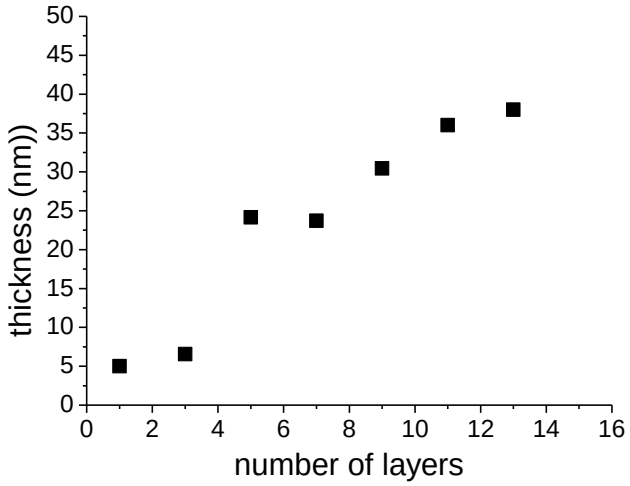

Figure 4.24 Relation between the number of layers and the thickness of the polyelectrolyte.

From the figure we find that the there is an almost linear increase in the thickness with increasing number of layers [148-149].

Some deviations from linearity are observed which we attribute to the fact that in ellipsometry measurements there is relation between thickness and refractive index of the films that may be a source of error in the measurements.

These layer thicknesses have measured several times with only small variation in the results. The aim of this experiment is to increase the reflectivity of the substrate and to reduce the metal substrate effect for those gold nanoparticles that fill in the pores between the dielectric spheres. We tested the polyelectrolyte intermediate layers on silicon wafer in order to be able to prepare films of different, well-defined thickness.

To measure the thickness of the polyelectrolyte film by ellipsometry, we repeated the deposition experiment on gold-coated substrates and consider the relation between number of layers and the thickness and estimate the thickness of the layers on gold substrate as it is difficult to measure the polyelectrolyte layer thickness directly on gold substrate. The resulting spectra, however, were highly irreproducible and showed significant variation both within one sample and from sample to sample for the same number of polyelectrolyte layers.

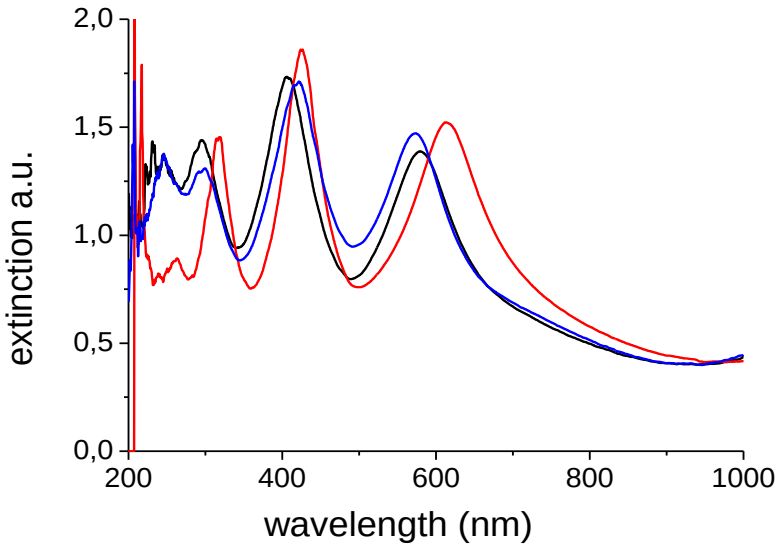

Figure 4.25 UV/Vis-spectra of gold-coated substrates with five double layers of polyelectrolyte in between the substrate and the metalized spheres for 3 different spots on the same sample. Although being prepared following the same procedure, a significant variation on the peak positions is observed.

Fig 4.25 shows the reflection peak of metalized dielectric spheres deposited on a gold-coated substrate and an intermediate layer of $PEI(PSS-PAH)_5$ with a thickness of approximately 25nm. There is a significant variation on the peak positions for one sample at different spots that prevent the use of the substrate for accurate sensitivity measurements.

Due to the apparent inhomogeneity of the polyelectrolyte layers in our experiments, which we attribute to polyelectrolyte/solvent interactions [150] as we test the sensitivity of such surface with thiol where we need to dissolve the thiol in ethanol.

We replaced it by a silicon oxide thin film. Here, the thickness and the properties of the samples can be properly controlled, and the interlayer material does not interact with the solvent.

4.10.1.1 Sensitivity measurements

As expected from the previous results, the sensitivity of samples with polyelectrolyte interlayers between the metalized spheres and a gold-coated substrate were not reproducible for the same polyelectrolyte thickness. In addition, negative blue shift upon fibrinogen adsorption was observed in some parts of the sample. That led to the decision to replace it with a silicon oxide layer as mentioned before.

Fig 4.26 shows sensitivity measurements for fibrinogen adsorption in case of 3 intermediate layers of polyelectrolyte in between, where we found a blue shift of the extinction peaks.

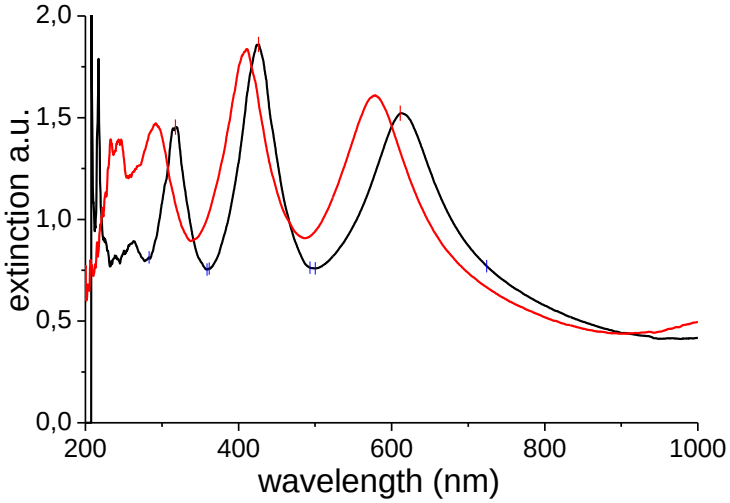

Figure 4. 26 Blue shift for fibrinogen adsorption for samples with 3 intermediate polyelectrolyte interlayer. Spectra are shown before (black line) and after adsorption of fibrinogen .

4.10.2- Silicon oxide/dioxide interlayer

We know from the previous section that the polyelectrolyte layer separation have drawback in the results as the thickness of the polyelectrolyte is difficult to control and appears to be inhomogeneous. In addition we found that in case of polyelectrolyte layer the change in the dielectric constant of the solvent medium, for sensitivity measurements, however change the strength of electrostatic interactions between the polyelectrolyte chains [150]. For these reasons we replaced the polyelectrolyte spacer by silicon oxide. Here, silicon oxide layers of different thickness were deposited on substrates coated with a 5 nm titanium adhesion layer and 30 nm of gold these silicon oxide layers were left in air to oxidize to silicon dioxide. We do not expect the whole layer to be completely oxidized; the interlayer will probably contain both silicon oxide and dioxide. The thicknesses of these layers were measured after fabrication by AFM and then by ellipsometry. Deviations in the results of the two techniques were in range of 10 to 15 %. Fig 4.23 shows the relation between the position of the resonance peak and the thickness of silicon oxide/dioxide intermediate layer.

The dielectric spheres were coated by seeding and plating. 3 min. of plating time were chosen as this provides peaks of sufficiently high intensity and narrow bandwidth.

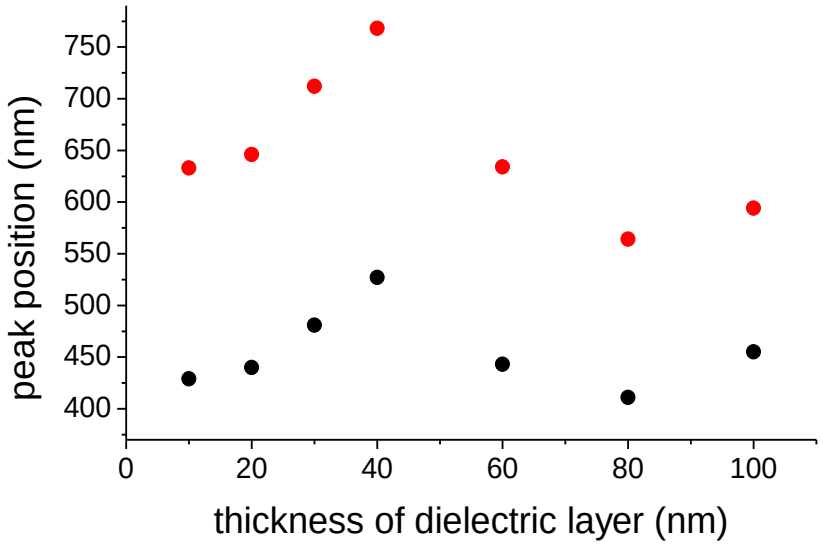

Figure 4.27 change in the position of the extinction peaks with increasing thickness of the silicon oxide/dioxide interlayer. Where the (red dots) are the shift for the peak in wave length range 600-900 and (black dots) are for the wavelength range 400-600

From figure we observe that the peak positions red shift for both wavelength regimes (400-600 nm and 600-900 nm) upon increasing the dielectric layer up to 40 nm thickness. Afterwards, they start to blue shift until 80 nm thickness and then red shift again for high thicknesses of the dielectric layer. The observed trend is the same as for the reflectivity of thin films [25] so that we can interpret the spectrum as a result of interference due to multireflection in the dielectric spheres and the thin dielectric layer. It looks as if there is a maximum coupling strength at a certain thickness of the dielectric, above which the peak shifts to blue and below which the peak shifts to red. We also notice that the peaks become sharper for the same time of plating as the thickness of the dielectric layer increases and minimizes the scattering due to defects in the coverage of the dielectric spheres or compensates for the scattering of the dielectric spheres as for high thickness we found that the peak position does not change much and the band width is not affected by the coverage of the metalized spheres.

We can also explain the higher shift in peak position for 40 nm silicon oxide layer thickness on gold-coated substrate by to the increase in the reflectivity of the metalized substrate upon deposition of a thin dielectric film also due to the modulated field intensity by the silicon oxide/dioxide layer [33] [151]

4.10.2.1 Sensitivity measurement

Figure 4.28 shows the sensitivity measurement for fibrinogen adsorption when changing the thickness of silicon oxide/dioxide layer in between the metalized spheres and the gold-coated substrate.

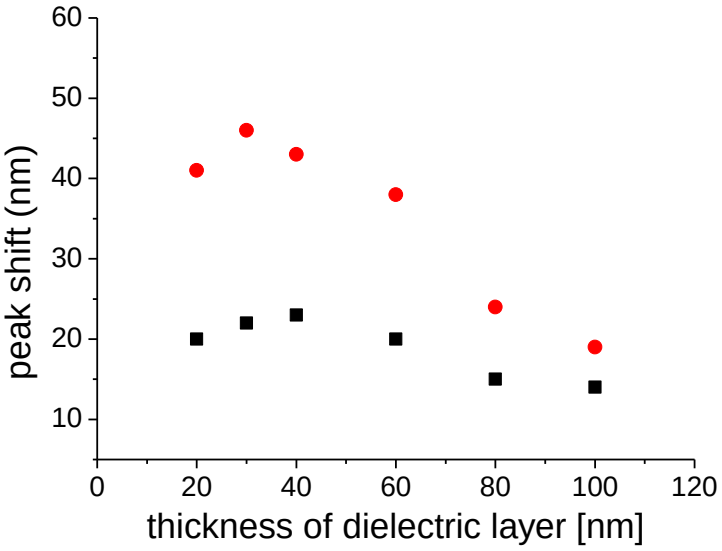

Figure 4.28 Peak shift due to adsorption of fibrinogen for increasing the thickness of the silicon oxide/dioxide layer between the metalized spheres and gold-coated substrate.

From figure 4.28 we observe the same trend for the sensitivity as for the peak positions (*cf.* fig 4.27). The sensitivity increases with increasing dielectric layer thickness reaching maximum value at a thickness of 40 nm silicon oxide/dioxide. Then the sensitivity decreases upon further increase in the layer thickness until a plateau is reached showing lowest sensitivity for very high thickness. These results can be explained as follows: From figure 4.28 we can see that the peaks red shift with increasing layer thickness up to 40 nm thickness which means that the reflectivity of the gold substrate increase with deposition thin films of a dielectric (silicon oxide/dioxide) layer and reach maximum reflectivity at the thickness of 40 nm.

In parallel, the sensitivity increases with increasing reflectivity as the refractive index of the supporting dielectric increase. Then the reflectivity drops again with increase the thickness of the dielectric [33] above 40 nm where the sensitivity also decreases. For higher thicknesses above 80 nm the peaks start to red shift again, but the sensitivity still decreases until a low value plateau is reached.

This may be due to the fact that the thicker planar dielectric layer starts to contribute to the interference phenomena in the spheres as we can see that the peaks become more intense and sharper. Such optimum dielectric thicknesses also occur for nonmetallic substrate. As well as we observe such sensitivity enhancement at such thickness in case of metal nanoparticles on substrate which could give us the idea that at such thickness the field intensity modulated at such thickness and this not depend on the kind of the substrate or the shape of the metal particles on the substrate

4.11 Metallization by physical vapor deposition (PVD)

The second method used for metallization of the dielectric spheres was evaporation of thin films of gold of different thickness onto the surface of the dielectric spheres. In this approach, the thin gold films cover the surface of spheres with a continuous and smooth film, which is only deposited onto the upper half sphere of the core particles ("cap-shape coverage"). The high degree of curvature present at the surface of a metal sphere with diameter comparable to the incident wavelength allows us to excite the plasmon directly as the surface is periodically corrugated. Fig 4.22 shows the SEM image of thin films of gold evaporated onto dielectric spheres of 500 nm diameter. The spheres are separated until the gold coating reaches a thickness of 100 nm. For this configuration, one should emphasize that the surface morphology of the fabricated metallic films is quite complex due to the superposition of the half-shells and truncated tetrahedral that are formed in the spaces between the spheres. These are geometrically different and give their own optical response. Moreover, the scattering makes it difficult to accurate analyse the overall optical response of these nanostructure films.

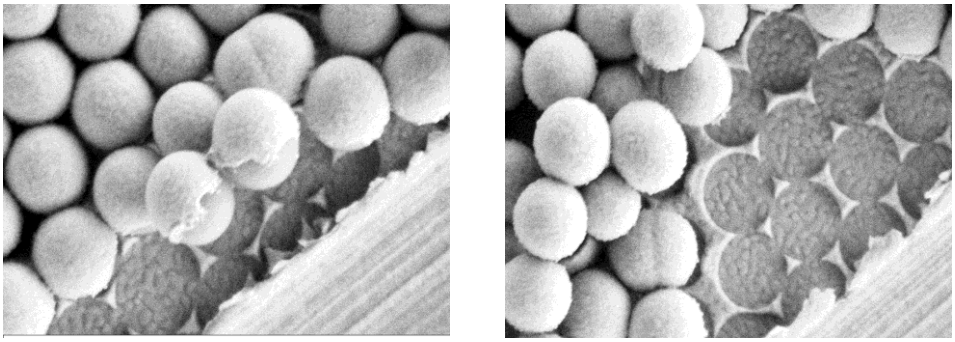

Figure 4.29 SEM images of thin films of evaporated of gold on dielectric spheres of 500 nm diameter. Where the spheres have been removed from the surface truncated tetrahedral structures of evaporated gold are seen, which have been deposited on the flat substrate.

Fig 4.30 shows the UV-Vis spectra of different samples, where dielectric spheres of 500 nm size have been covered with thin film of gold of 10, 20, 30, 50 and 70 nm thickness.
From the figure we see that the reflectance spectra between 400 and 600 nm decrease in intensity and red shift with increasing metal thickness from 10 to 50 nm as the reflectivity of cap-shaped gold metal thin film increases with increasing thickness [152]. Thus, the transmittance of the incident beam into the sample decreases, reducing the intensity of the reflected beam and the interference beam as well.
For the peak between 600 and 900 nm the intensity of the peak does not change much upon variation of thin film thickness. A slight blue shift is observed as the thickness increases from 10 nm to 30 nm and then a red shift for further increase in the thickness to 70 nm.

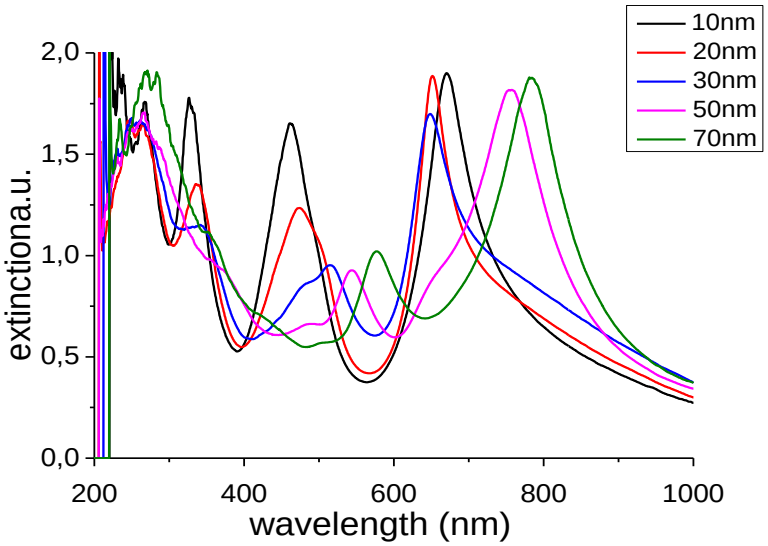

Figure 4.30 The reflection spectra of dielectric sphere monolayers covered with thin gold films of different thickness (10, 20, 30, 50, and 70 nm)

From fig 4.30 we find that by increasing the thickness of the metal film on the dielectric spheres the number of resonance peaks decreases and the intensity of the peak in range from 400-600 nm wavelength decreases and red shifts. The result that the number of resonance peaks decreases is not surprising as with increasing the thickness of the gold layer on the dielectric spheres make the metal layer more opaque so that the incident light will not be able to penetrate to the dielectric spheres for interference resonance. However, the intensity of the peak in the wavelength range from 600-900 nm is not changed. For further increase in gold thickness to 100nm thick, we found only one resonance peak shown in fig 4.31

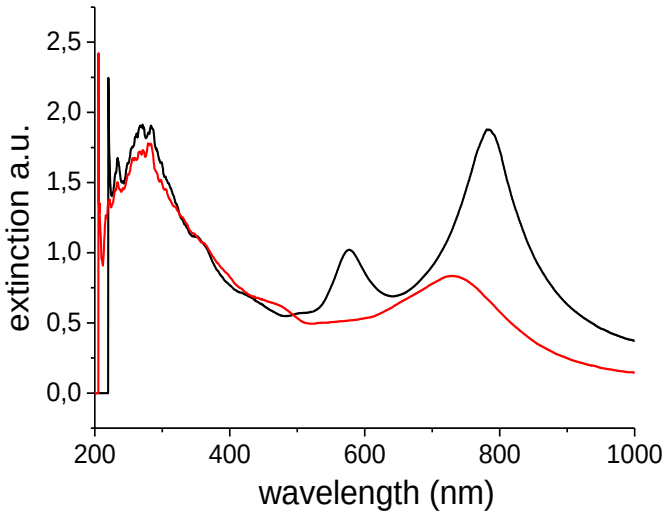

Figure 4.31 Reflection spectra of dielectric sphere monolayer covered with thin gold films of 70 (black line)and 100 nm(red line) thickness.

Again, the existence of two metallic gratings, one arising from the obvious half-shells and the other one from less obvious truncated tetrahedral, which are geometrically different and generate their own optical response, makes the accurate analysis of the overall optical response of such nanostructures difficult. Moreover, also the effect of increasing the metal thickness on the reflectivity and the transmission of the incident beam has to be taken into account.

4.11.1 Sensitivity measurements

The sensitivity measurements for dielectric sphere monolayers covered with thin gold films of different thickness show increasing sensitivity for gold thicknesses up to 50nm. For higher thicknesses sensitivity drops again (fig 4.32).

Which give the optimum thickness for the highest sensitivity as the lateral distance between the two covered metal spheres has high field enhancement [153]

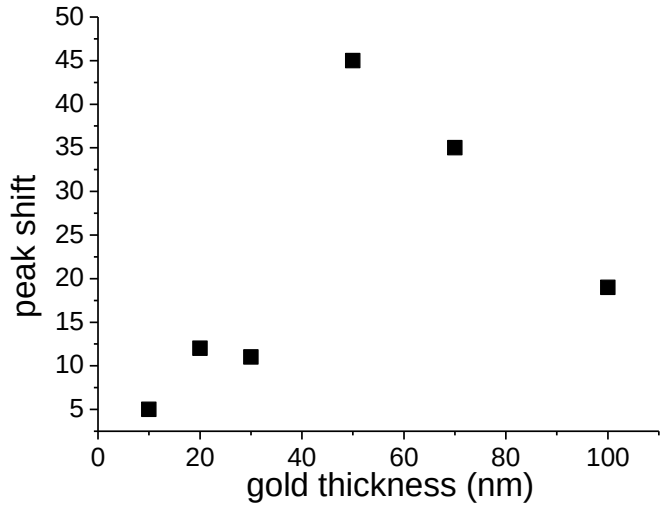

Figure 4.32 Sensitivity measurements for silica sphere monolayers coated with thin gold films of different thickness measured for the peak at 600-900 nm.

The drop in sensitivity for higher thickness of gold can be explain due to the fact that at such high gold film thickness the coupling between the interference peaks and the Plasmon resonance no longer exists as we can see from the single peak that only exists in case of 100 nm gold coating (fig 4.31).

4.12 Antibody –antigen interaction

Inspired by the improvement of the sensitivity in the presence of a dielectric layer in between the substrate and the core-shell nanopatricle layer, we prepared a substrate with a 40 nm silicon oxide/dioxide layer on top of a 30 nm gold film. Afterwards we deposited dielectric spheres of 500 nm diameter on the substrate via floating and metalized the spheres by seeding and 3 min. plating. Finally, these samples were tested for their biosensing capacity in antibody-antigen interactions.

For this experiment we used two samples with immobilized mouse anti-human IgG: following the procedure detailed above, one sample was exposed to goat anti-rabbit IgG to test for non-specific IgG adsorption.

The other sample was exposed to goat anti-mouse IgG, which will specifically interact with immobilized mouse anti-human IgG. The results are shown in figure 4, 33 and summarized in table 4.7

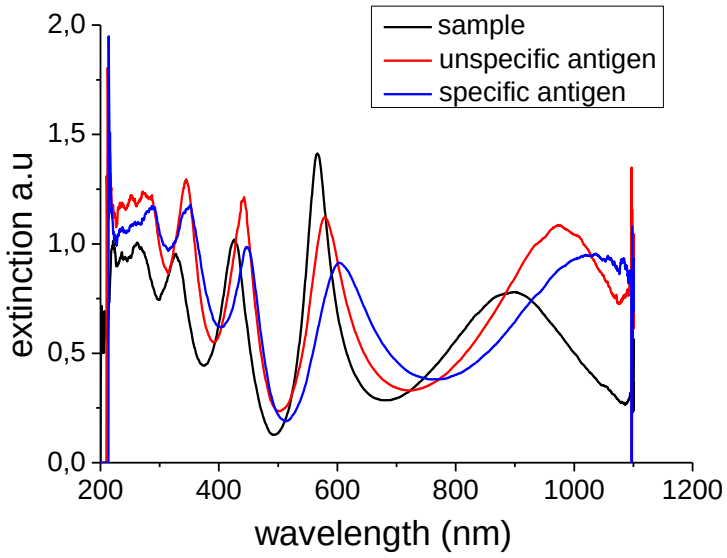

Figure 4. 33 *Extinction spectra for the nanoparticle-coated surface (black), the nanoparticle-coated surface after antigen immobilization and unspecific IgG interaction (red), and the nanoparticle coated surface after antigen immobilization and specific IgG interaction (blue line).*

The wavelength shift between the red and the black curve is caused by the immobilization of mouse anti-human IgG plus BSA and non-specific IgG adsorption. The shift between the black and the red curve is due to the immobilization of mouse anti-human IgG plus BSA and specific IgG adsorption. Thus, the difference between the blue and the red curve accounts for the contribution of specific antigen-antibody interactions to the overall response.
The results are summarized in table 4.7

conditions	Wavelength shift for peak at 400-600 nm	Wavelength shift for peak at 600-900 nm
Unspecific binding	16 nm	85 nm
Specific binding	40 nm	136 nm

Table 4. 7 *sensitivity shiftdue specific and unspecific interaction*

Chapter 5

Summary and conclusion

In this thesis we constructed a label-free biosensor which is based on a combination of surface plasmon resonance and reflectometric interference. Both techniques have been utilized for label-free biosensing for more than two decades as the corresponding extinction spectra undergo a wavelength shift upon molecule binding. Thus we believed that an appropriate combination of the two techniques would facilitate the development of an optical biosensor with improved sensitivity towards molecule adsorption.

The samples were prepared by deposition of dielectric spheres of 400-500 nm in diameter onto a solid substrate in order to optimize for the interference conditions. From the different deposition techniques tested, the floating transfer method, in which the dielectric spheres are first floated on a liquid subphase and then transferred to the solid support in a Langmuir-Blodgett like approach. Although this method, which provided hexagonally packed spheres over large surface areas, still needs to be optimized for stronger attachment of the spheres to the surfaces, it yielded significantly improved reproducibility compared to particle deposition via random adsorption or spin-coating, which is an important prerequisite to optimize sensor response and improve sensitivity. In a second step, the substrate was metalized using two different methods: (i) deposition metal nanoparticles from solution (seeding) followed by an enlargement of the nanoparticles in gold salt solutions (plating), and (ii) evaporation of a thin metal film on the top of the spheres by physical vapor deposition (PVD). The resulting optical response and morphology were characterized by UV-Vis spectroscopy and scanning electron microscopy (SEM).

For metal deposition from gold salt solutions we varied the plating time and studied the impact of gold metal coverage on the optical response and sensitivity towards molecule adsorption for each type of sample, also the resulting morphology was checked by SEM.
Up to a plating time of about 10 min, the sharpness and intensity of the peaks increased followed by a subsequent decrease in peak height. We also noticed that with increasing plating time (i.e. thickness of the metal shell) the peaks slightly red shift which means that at such mesoscopic size of the metalized cores we lose the wavelength tunibility in accord with Halas group[154]

They explain this effect by the inability of light to polarize the whole metal shell core in this size regime, which leads to excitation of higher order modes. However, we could prove that the multipeaks already exist prior to the metallization process and are due to the interference of the reflected beams from the spheres. The role of the metal coating was to increase the intensity and slightly red shift the extinction peak position due to increasing the size of the gold nanoparticles.

The SEM images show both a lateral and vertical growth of the gold nanoparticles associated with an increasingly random morphology. Sensitivity, however, was found to decrease with increasing plating time and is highest for purely seeded surfaces. However, as the peaks are broader, small wavelength shifts are more difficult to detect.

In a comparison of close packed and randomly adsorbed layers of metalized dielectric spheres we found in case of random coverage a significant blue shift in the peaks position along with decrease in sensitivity in comparison to the close packed films.
We also studied the effect of an underlying thin metal film, deposited in between the substrate and the dielectric spheres, on the optical properties and sensitivity of the samples. A red shift was observed for the metal coated substrate, whereas the sensitivity measurements showed slightly higher sensitivity for the non metal coated substrate.

We reduced the symmetry of the adsorbed core-shell nanoparticles by multiply coating the dielectric core with a sequence of dielectric and metallic layers. In this case, we observed a significant red shift for the peak in range of 600-900 nm, while the other peak in range of 400-600 nm was not affected. The sensitivity measured after depositing the fourth dielectric/metallic layer was very low.

In order to discriminate the impact of metal shell thickness and metal shell roughness on the sensitivity, metal films of various thicknesses have also been deposited on top of the spheres by PVD.

In contrast to the plated layers these films have a smooth topography. When depositing metal thicknesses of 10, 20, 30, 50, 70, and 100 nm on the spheres by PVD, we found well-defined multiple resonance peaks for small gold thickness.

The number of these resonance peaks decreased as we increased the thickness up to 100 nm. The fact, that for 100 nm metal coating only one resonance peak was left, gave additional evidence that the origin of such peaks are the interference of reflected beams. Such structure yielded the highest sensitivity at 50 nm of gold film thickness. It may, thus, be concluded that for the seeded and plated layers effects of surface morphology are more important with respect to sensitivity than layer thickness.

We also investigated the difference between the optical properties of substrates coated with planar thin dielectric films and dielectric sphere monolayer, respectively. The thickness of the thin films was selected close to the diameter of the dielectric spheres. We found out that the resonance peaks are qualitatively the same but much narrower in case of thin film. Yet, a higher sensitivity for the dielectric spheres.

We also studied the effect of an intermediate dielectric layer in between the substrate and the metalized spheres in order to improve the reflectivity of the samples and the sensitivity of extinction peak positions towards molecule adsorption. For SiO_2 interlayers an optimum thickness of 40 nm was found for sensitivity enhancement. Such optimum thickness turned out to be independent of the particle coverage as well as of the kind of substrate used (gold-coated or plain silicon wafer). The enhancement could be explained by modulated field intensity in the silicon dioxide layer. We can conclude from this result that it would be very useful to use different dielectric layers with different reflective indices as this will change the field intensity and affect the enhancement of the field.

To investigate the effect of different metals, we replaced the coating of the dielectric spheres by silver nanoparticles

For similar metal coverage we found a significantly higher sensitivity in case of the silver coating for the extinction peak in the wavelength regime from 400-600 nm, while the sensitivity of the 600-900 nm peak was almost the same for both metals.

As a final application we investigated the performance of the optimized biosensor in the label-free detection of antibody –antigen reactions and the study of non-specific protein adsorption.

In conclusion we found optimum conditions to improve the sensitivity towards molecule adsorption for label-free biosensing. We could combine surface plasmon resonance and reflectometric interference sensors by using dielectric spheres of 400-500 nm size and coating them with metal. Using this structure we found that the sensitivity is affected by the coverage of surface with dielectric spheres showing higher sensitivity for closely packed layers. Also we could achieve higher sensitivity for silver than for gold nanoparticle coatings for the peak in the 400-600 nm wavelength regimes, while the same sensitivity was obtained for the peak in the range of 600-900 nm.

We also improve the sensitivity by introducing a thin dielectric layer of optimum thickness in between the metalized spheres and the substrate. The thickness of such layer was found to be independent on the kind of substrate used (metalized or not). For gold films deposited by PVD we found an optimum gold thin film thickness of 50 nm to provide higher sensitivity.

Future work should focus on the use of different metals or alloys in the seeding and plating step as the choice of the coating material seems to significantly affect sensitivity. Surface morphology of the metal shell is another important point that needs to be properly controlled and optimized. Additional potential lies in optimizing the interparticle distance and introducing additional dielectric layers with suitable dielectric function in between the metalized spheres and the substrate to optimize beam interference and optical resonance. For all these optimization strategies, a close collaboration with a research group that can model the optical response of the various surface structures would be very helpful and stimulating.

Abbreviations

SPR surface plasmon resonance

LSPR localized surface plasmon resonance

RIFS reflectometric interference spectroscopy

EM electromagnetic

TM transverse-magnetic

PEI Polyethylenimine

PSS Poly (sodium 4-styrenesulfonate)

PBS phosphate Buffered saline

PAH polyallylamino-hydrochlorid

PVD physical vapor deposition

AFM atomic force microscope

Ig immunoglobulin (antibody)

SAM self assembling monolayer

SEM scanning electron microscopy

UV ultraviolet

VIS visual

NSL nanosphere lithography

List of Figures

List of tables

Bibliography

1. Bernard, A. and H.R. Bosshard, *Real-Time Monitoring of Antigen-Antibody Recognition on a Metal-Oxide Surface by an Optical Grating Coupler Sensor*. European Journal of Biochemistry, 1995. **230**(2): p. 416-423.
2. Polzius, R., et al., *Real-time observation of affinity reactions using grating couplers: Determination of the detection limit and calculation of kinetic rate constants.* Analytical Biochemistry, 1997. **248**(2): p. 269-276.
3. Piehler, J., et al., *Label-free monitoring of DNA-ligand interactions.* Analytical Biochemistry, 1997. **249**(1): p. 94-102.
4. Brecht, A., G. Gauglitz, and W. Nahm, *Interferometric Measurements Used in Chemical and Biochemical Sensors.* Analusis, 1992. **20**(3): p. 135-140.
5. Abel, A.P., et al., *Fiber-optic evanescent wave biosensor for the detection of oligonucleotides.* Analytical Chemistry, 1996. **68**(17): p. 2905-2912.
6. Hutchinson, A.M., *Evanescent-Wave Biosensors - Real-Time Analysis of Biomolecular Interactions.* Molecular Biotechnology, 1995. **3**(1): p. 47-54.
7. Homola, J., S.S. Yee, and G. Gauglitz, *Surface plasmon resonance sensors: review.* Sensors and Actuators B-Chemical, 1999. **54**(1-2): p. 3-15.
8. Nikitin, P.I., et al., *Surface plasmon resonance interferometry for biological and chemical sensing.* Sensors and Actuators B-Chemical, 1999. **54**(1-2): p. 43-50.
9. Lyon, L.A., M.D. Musick, and M.J. Natan, *Colloidal Au-enhanced surface plasmon resonance immunosensing.* Analytical Chemistry, 1998. **70**(24): p. 5177-5183.
10. Cunningham, B.T., *Label-Free Biosensors: Techniques and Applications*, ed. E.b.M.A. Cooper. 2009: Cambridge University Press.
11. Homola, J., I. Koudela, and S.S. Yee, *Surface plasmon resonance sensors based on diffraction gratings and prism couplers: sensitivity comparison.* Sensors and Actuators B-Chemical, 1999. **54**(1-2): p. 16-24.
12. Piliarik, M. and J. Homola, *Surface plasmon resonance (SPR) sensors: approaching their limits?* Optics Express, 2009. **17**(19): p. 16505-16517.
13. Haes, A.J. and R.P. Van Duyne, *A nanoscale optical blosensor: Sensitivity and selectivity of an approach based on the localized surface plasmon resonance spectroscopy of triangular silver nanoparticles.* Journal of the American Chemical Society, 2002. **124**(35): p. 10596-10604.

14. Lee, K.S. and M.A. El-Sayed, *Gold and silver nanoparticles in sensing and imaging: Sensitivity of plasmon response to size, shape, and metal composition.* Journal of Physical Chemistry B, 2006. **110**(39): p. 19220-19225.
15. Brecht, A., J. Ingenhoff, and G. Gauglitz, *Direct Monitoring of Antigen-Antibody Interactions by Spectral Interferometry.* Sensors and Actuators B-Chemical, 1992. **6**(1-3): p. 96-100.
16. Gauglitz, G., et al., *Chemical and Biochemical Sensors Based on Interferometry at Thin (Multi-)Layers.* Sensors and Actuators B-Chemical, 1993. **11**(1-3): p. 21-27.
17. Collins, B.E., et al., *Determining protein size using an electrochemically machined pore gradient in silicon.* Advanced Functional Materials, 2002. **12**(3): p. 187-191.
18. Piehler, J., A. Brecht, and G. Gauglitz, *Affinity detection of low molecular weight analytes.* Analytical Chemistry, 1996. **68**(1): p. 139-143.
19. Hiep, H.M., H. Yoshikawa, and E. Tamiya, *Interference Localized Surface Plasmon Resonance Nanosensor Tailored for the Detection of Specific Biomolecular Interactions.* Analytical Chemistry, 2010. **82**(4): p. 1221-1227.
20. Gauglitz, G., et al., *Spectral Interference Refractometry by Diode-Array Spectrometry.* Analytical Chemistry, 1988. **60**(23): p. 2609-2612.
21. Birkert, O., et al., *A streptavidin surface on planar glass substrates for the detection of biomolecular interaction.* Analytical Biochemistry, 2000. **282**(2): p. 200-208.
22. Hiep, H.M., et al., *An Interference Localized Surface Plasmon Resonance Biosensor Based on the Photonic Structure of Au Nanoparticles and SiO2/Si Multilayers.* Acs Nano, 2009. **3**(2): p. 446-452.
23. Hiep, H.M., et al., *Immobilization of Gold Nanoparticles on Aluminum Oxide Nanoporous Structure for Highly Sensitive Plasmonic Sensing.* Japanese Journal of Applied Physics, 2010. **49**(6): p. -.
24. Maehashi, K., et al., *Label-free protein biosensor based on aptamer-modified carbon nanotube field-effect transistors.* Analytical Chemistry, 2007. **79**(2): p. 782-787.
25. Chopra, K., *thin film phenomena*. 1969.
26. Kneipp, K., et al., *Single molecule detection using surface-enhanced Raman scattering (SERS).* Physical Review Letters, 1997. **78**(9): p. 1667-1670.
27. Michaels, A.M., M. Nirmal, and L.E. Brus, *Surface enhanced Raman spectroscopy of individual rhodamine 6G molecules on large Ag nanocrystals.* Journal of the American Chemical Society, 1999. **121**(43): p. 9932-9939.
28. Le, F., et al., *Metallic nanoparticle arrays: A common substrate for both surface-enhanced Raman scattering and surface-enhanced infrared absorption.* Acs Nano, 2008. **2**(4): p. 707-718.
29. Kim, D.K., et al., *Label-free DNA biosensor based on localized surface plasmon resonance coupled with interferometry.* Analytical Chemistry, 2007. **79**(5): p. 1855-1864.

30. Buecker, P., et al., *Label-free biosensors based on optically responsive nanocomposite layers: Sensitivity and dynamic range.* Langmuir, 2008. **24**(15): p. 8229-8239.
31. Dahint, R., et al., *Optically responsive nanoparticle layers for the label-free analysis of biospecific interactions in array formats.* Biosensors & Bioelectronics, 2007. **22**(12): p. 3174-3181.
32. Dmitriev, A., et al., *Enhanced Nanoplasmonic Optical Sensors with Reduced Substrate Effect.* Nano Letters, 2008. **8**(11): p. 3893-3898.
33. Chopra, K.L., *Thin film phenomena*. 1979, Huntington, N.Y.: R. E. Krieger Pub. Co. xx, 844 p.
34. Heavens, O.S., *optical properties of thin film.* Reports on progress in physics, 1960. **23**(1).
35. Bergmann, L., C. Schaefer, and H. Niedrig, *Optics of waves and particles*. 1999, Berlin ; New York: W. de Gruyter. xviii, 1256 p., 4 p. of plates.
36. Brecht, A. and G. Gauglitz, *Optimized Layer Systems for Immunosensors Based on the Rifs Transducer.* Fresenius Journal of Analytical Chemistry, 1994. **349**(5): p. 360-366.
37. Rasooly, A., Herold, K. E., *Biosensor and detection methods and protocols*, ed. J.M. Walker. Vol. 503. 2009.
38. Endo, T., et al., *Localized surface plasmon resonance based optical biosensor using surface modified nanoparticle layer for label-free monitoring of antigen-antibody reaction.* Science and Technology of Advanced Materials, 2005. **6**(5): p. 491-500.
39. Endo, T., et al., *Label-free detection of peptide nucleic acid-DNA hybridization using localized surface plasmon resonance based optical biosensor.* Analytical Chemistry, 2005. **77**(21): p. 6976-6984.
40. Raether, H., *Surface-Plasmons on Smooth and Rough Surfaces and on Gratings.* Springer Tracts in Modern Physics, 1988. **111**: p. 1-133.
41. Maier, S., *Fundamentals and Applications.* . 2007, Springer.
42. Maier, S., *Plasmonic: Fundamentals and applications*, ed. N.Y. Springer. 2007.
43. Hutley, M.C., *Diffraction gratings*. Techniques of physics,. 1982, London ; New York: Academic Press. ix, 330 p.
44. Schatz, C.K., L. K., *The Optical Properties of Metal Nanoparticles: The Influence of Size, Shape, and Dielectric Environment.* J. Phys. Chem. B, 2003. **107**.
45. Homola, J., *surface plasmon resonance based sensors*. 2006: Springer: Berlin, Germany.
46. Miller, M.M. and A.A. Lazarides, *Sensitivity of metal nanoparticle surface plasmon resonance to the dielectric environment.* Journal of Physical Chemistry B, 2005. **109**(46): p. 21556-21565.
47. Maier, S.A. and H.A. Atwater, *Plasmonics: Localization and guiding of electromagnetic energy in metal/dielectric structures.* Journal of Applied Physics, 2005. **98**(1): p. -.

48. Jain, P.K., W.Y. Huang, and M.A. El-Sayed, *On the universal scaling behavior of the distance decay of plasmon coupling in metal nanoparticle pairs: A plasmon ruler equation.* Nano Letters, 2007. **7**(7): p. 2080-2088.
49. Kreibig, U. and M. Vollmer, *Optical properties of metal clusters*. Springer series in materials science. 1995, Berlin ; New York: Springer. xx, 532 p.
50. Alvarez, M.M., et al., *Optical absorption spectra of nanocrystal gold molecules.* Journal of Physical Chemistry B, 1997. **101**(19): p. 3706-3712.
51. Christy, R.W., *Optical constants of the noble metals.* .Phys.Rev. B,, 1972. **6**: p. 4370–4379.
52. R., H.W., *Handbook of Optical Constants of Solids*, ed. E.D. Palik. 1985: Academic Press.
53. Mie, G., Ann. phys., 1908. **25**: p. 329.
54. Jain, P.K. and M.A. El-Sayed, *Plasmonic coupling in noble metal nanostructures.* Chemical Physics Letters, 2010. **487**(4-6): p. 153-164.
55. Jain, P.K., I.H. El-Sayed, and M.A. El-Sayed, *Au nanopartices target cancer (vol 2, pg 18, 2007).* Nano Today, 2007. **2**(2): p. 16-16.
56. Wokaun, A., Liao, P.F., *Radiation Damping in surface- enhanced raman scattering.* Phys. Rev. Lett., 1982. **48**.
57. Jain, P.K. and M.A. El-Sayed, *Universal scaling of plasmon coupling in metal nanostructures: Extension from particle pairs to nanoshells.* Nano Letters, 2007. **7**(9): p. 2854-2858.
58. Prodan, E., et al., *A hybridization model for the plasmon response of complex nanostructures.* Science, 2003. **302**(5644): p. 419-422.
59. Rechberger, W., et al., *Optical properties of two interacting gold nanoparticles.* Optics Communications, 2003. **220**(1-3): p. 137-141.
60. Haynes, C.L., et al., *Nanoparticle optics: The importance of radiative dipole coupling in two-dimensional nanoparticle arrays.* Journal of Physical Chemistry B, 2003. **107**(30): p. 7337-7342.
61. Gunnarsson, L., et al., *Confined plasmons in nanofabricated single silver particle pairs: Experimental observations of strong interparticle interactions.* Journal of Physical Chemistry B, 2005. **109**(3): p. 1079-1087.
62. Maier, S.A., P.G. Kik, and H.A. Atwater, *Observation of coupled plasmon-polariton modes in Au nanoparticle chain waveguides of different lengths: Estimation of waveguide loss.* Applied Physics Letters, 2002. **81**(9): p. 1714-1716.
63. Wei, Q.H., et al., *Plasmon resonance of finite one-dimensional Au nanoparticle chains.* Nano Letters, 2004. **4**(6): p. 1067-1071.
64. Motte, L., et al., *Self-organization into 2D and 3D superlattices of nanosized particles differing by their size.* Journal of Physical Chemistry B, 1997. **101**(2): p. 138-144.
65. Lamprecht, B., et al., *Metal nanoparticle gratings: Influence of dipolar particle interaction on the plasmon resonance.* Physical Review Letters, 2000. **84**(20): p. 4721-4724.

66. Maier, S.A., et al., *Observation of near-field coupling in metal nanoparticle chains using far-field polarization spectroscopy.* Physical Review B, 2002. **65**(19): p. -.
67. Huang, X.H., et al., *Determination of the minimum temperature required for selective photothermal destruction of cancer cells with the use of immunotargeted gold nanoparticles.* Photochemistry and Photobiology, 2006. **82**(2): p. 412-417.
68. Sweatlock, L.A., et al., *Highly confined electromagnetic fields in arrays of strongly coupled Ag nanoparticles.* Physical Review B, 2005. **71**(23): p. -.
69. Krenn, J.R., et al., *Squeezing the optical near-field zone by plasmon coupling of metallic nanoparticles.* Physical Review Letters, 1999. **82**(12): p. 2590-2593.
70. Schuck, P.J., et al., *Improving the mismatch between light and nanoscale objects with gold bowtie nanoantennas.* Physical Review Letters, 2005. **94**(1): p. -.
71. Aizpurua, J., et al., *Optical properties of coupled metallic nanorods for field-enhanced spectroscopy.* Physical Review B, 2005. **71**(23): p. -.
72. Kneipp, K., et al., *Surface-enhanced Raman scattering and biophysics.* Journal of Physics-Condensed Matter, 2002. **14**(18): p. R597-R624.
73. Su, K.H., et al., *Interparticle coupling effects on plasmon resonances of nanogold particles.* Nano Letters, 2003. **3**(8): p. 1087-1090.
74. Mock, J.J., D.R. Smith, and S. Schultz, *Local refractive index dependence of plasmon resonance spectra from individual nanoparticles.* Nano Letters, 2003. **3**(4): p. 485-491.
75. Tam, F., C. Moran, and N.J. Halas, *Geometrical parameters controlling sensitivity of nanoshell plasmon resonances to changes in dielectric environment.* Journal of Physical Chemistry B, 2004. **108**(45): p. 17290-17294.
76. Nelson, B.P., et al., *Near-infrared surface plasmon resonance measurements of ultrathin films. 1. Angle shift and SPR imaging experiments.* Analytical Chemistry, 1999. **71**(18): p. 3928-3934.
77. Malinsky, M.D., et al., *Chain length dependence and sensing capabilities of the localized surface plasmon resonance of silver nanoparticles chemically modified with alkanethiol self-assembled monolayers.* Journal of the American Chemical Society, 2001. **123**(7): p. 1471-1482.
78. McFarland, A.D. and R.P. Van Duyne, *Single silver nanoparticles as real-time optical sensors with zeptomole sensitivity.* Nano Letters, 2003. **3**(8): p. 1057-1062.
79. Mulvaney, P., *Surface plasmon spectroscopy of nanosized metal particles.* Langmuir, 1996. **12**(3): p. 788-800.
80. Kelly, K.L., et al., *The optical properties of metal nanoparticles: The influence of size, shape, and dielectric environment.* Journal of Physical Chemistry B, 2003. **107**(3): p. 668-677.
81. Mock, J.J., et al., *Shape effects in plasmon resonance of individual colloidal silver nanoparticles.* Journal of Chemical Physics, 2002. **116**(15): p. 6755-6759.

82. Hulteen, J.C., *Nanosphere lithography: A materials general fabrication process for periodic particle array surfaces.* Vac Sci Technol A, 1995. **13**: p. 1553.
83. Haes, A.J. and R.P. Van Duyne, *Nanosensors enable portable detectors for environmental and medical applications.* Laser Focus World, 2003. **39**(5): p. 153-156.
84. Oldenburg, S.J., et al., *Nanoengineering of optical resonances.* Chemical Physics Letters, 1998. **288**(2-4): p. 243-247.
85. Oldenburg, S.J., et al., *Infrared extinction properties of gold nanoshells.* Applied Physics Letters, 1999. **75**(19): p. 2897-2899.
86. Kreibig, U., M. Quinten, and D. Schoenauer, *Optical-Properties of Many-Particle Systems.* Physica Scripta, 1986. **T13**: p. 84-92.
87. Kreibig, U., M. Quinten, and D. Schoenauer, *Many-Particle Systems - Models of Inhomogeneous Matter.* Physica A, 1989. **157**(1): p. 244-261.
88. Quinten, M., D. Schonauer, and U. Kreibig, *Electronic Excitations in Many-Particle Systems - a Quantitative-Analysis.* Zeitschrift Fur Physik D-Atoms Molecules and Clusters, 1989. **12**(1-4): p. 521-525.
89. Foss, C.A., M.J. Tierney, and C.R. Martin, *Template Synthesis of Infrared-Transparent Metal Microcylinders - Comparison of Optical-Properties with the Predictions of Effective Medium Theory.* Journal of Physical Chemistry, 1992. **96**(22): p. 9001-9007.
90. Foss, C.A., et al., *Template-Synthesized Nanoscopic Gold Particles - Optical-Spectra and the Effects of Particle-Size and Shape.* Journal of Physical Chemistry, 1994. **98**(11): p. 2963-2971.
91. Enders, D., *Surface Enhanced Infrared Absorption on Au Nanoparticle Films for Optical Biosensing*. 2005, Heidelberg, Germany.
92. Singham, S.B. and C.F. Bohren, *Light-Scattering by an Arbitrary Particle - a Physical Reformulation of the Coupled Dipole Method.* Optics Letters, 1987. **12**(1): p. 10-12.
93. Yoshida, S., *ptical properties of aggregated silver films.* J. Opt. Soc. Am., 1971. **61**: p. 62–69.
94. Vial, A., et al., *Improved analytical fit of gold dispersion: Application to the modeling of extinction spectra with a finite-difference time-domain method.* Physical Review B, 2005. **71**(8): p. -.
95. Berg, J.M., Tymoczko, J. L., *Biochemistry. 5th edition, ed*. 2002: Freeman, New York,.
96. Berg, J.M., Tymoczko, J. L., *Biochemistry.* 5th edition, ed. 2002: Freeman, New York,.
97. M., C., *Antibody engineering IgG effector mechanisms.* Chem. Immum, 1997. **110**: p. 65-88.
98. flegler, S.L., Heckman, J. W., *Scanning and Transmission electron microscope; an introduction*. 1993.
99. Brundle, C.R., *Encyclopedia of Materiah Characterization*, ed. J. C. Richard Brundle and Charles A. Evans. I992CUSA) Inc.

100. Goldstein, G.I.N., D. E.; Echlin, P.; Joy, D. C.; Fiori, C.; Lifshin, E., *Scanning electron microscopy and x-ray microanalysis*. 1981: New York: Plenum Press.
101. Everhart, T.E.T., R. F. M. , *Wide-band detector for micro-microampere low-energy electron currents.* Journal of Scientific Instruments 1960. **37**: p. 246-248.
102. Azzam, R.M.A., *Ellipsomety and Polarized Light;*. Vol. 0720406943 1977: North Holland; New york.
103. Rubahn, V.G.B.a.H.-G., *Optics and Spectroscopy at Surfaces and Interfaces.*, ed. WiLey-VCH. 2005.
104. Cao, X., *Antifouling Properties of Smooth and Structured Polyelectrolyte Thin Films*, University of Heidelberg.
105. Koelsch, P., *Static and dynamic properties of soluble surfactants at the air/water interface*. 2005, Universitaet Potsdam.
106. J. A. Woollam Co., I., *Guide to Using WVASE32: Software for VASE and M-44 Ellipsometers.*
107. Jenkins, F.A., White, H. E., *Fundamentals of Optics.* 1981: McGraw-Hill, Inc.,.
108. Decher, G., *Fuzzy nanoassemblies: Toward layered polymeric multicomposites.* Science, 1997. **277**(5330): p. 1232-1237.
109. Decher, G., *in Templating, Self-Assembly and Self-Organization*. Vol. 9. 1996: Pergamon, Oxford.
110. Yang, S.M., et al., *Nanomachining by colloidal lithography.* Small, 2006. **2**(4): p. 458-475.
111. Caruso, F., et al., *Investigation of electrostatic interactions in polyelectrolyte multilayer films: Binding of anionic fluorescent probes to layers assembled onto colloids.* Macromolecules, 1999. **32**(7): p. 2317-2328.
112. Himmelhaus, M. and H. Takei, *Self-assembly of polystyrene nano particles into patterns of random-close-packed monolayers via chemically induced adsorption.* Physical Chemistry Chemical Physics, 2002. **4**(3): p. 496-506.
113. Hanarp, P., et al., *Control of nanoparticle film structure for colloidal lithography.* Colloids and Surfaces a-Physicochemical and Engineering Aspects, 2003. **214**(1-3): p. 23-36.
114. Rybczynski, J., U. Ebels, and M. Giersig, *Large-scale, 2D arrays of magnetic nanoparticles.* Colloids and Surfaces a-Physicochemical and Engineering Aspects, 2003. **219**(1-3): p. 1-6.
115. Wang, X., Summers, C. J., *Large-Scale Hexagonal-PatternedGrowth of Aligned ZnO Nanorods for Nano-optoelectronics and Nanosensor Arrays.* Nano Letters, 2004. **4**(3): p. 423-426.
116. Zhang, Y.J., W. Li, and K.J. Chen, *Application of two-dimensional polystyrene arrays in the fabrication of ordered silicon pillars.* Journal of Alloys and Compounds, 2008. **450**(1-2): p. 512-516.
117. Preston, T.C. and R. Signorell, *Growth and Optical Properties of Gold Nanoshells Prior to the Formation of a Continuous Metallic Layer.* Acs Nano, 2009. **3**(11): p. 3696-3706.

118. Brown, K.R. and M.J. Natan, *Hydroxylamine seeding of colloidal Au nanoparticles in solution and on surfaces.* Langmuir, 1998. **14**(4): p. 726-728.
119. Brown, K.R., et al., *Hydroxylamine seeding of colloidal au nanoparticles. 3. Controlled formation of conductive Au films.* Chemistry of Materials, 2000. **12**(2): p. 314-323.
120. Larsson, E.M., et al., *Sensing characteristics of NIR localized surface plasmon resonances in gold nanorings for application as ultrasensitive biosensors.* Nano Letters, 2007. **7**(5): p. 1256-1263.
121. Trau, M., D.A. Saville, and I.A. Aksay, *Field-induced layering of colloidal crystals.* Science, 1996. **272**(5262): p. 706-709.
122. Deckmann, H.W., *Natural lithography.* applied phys. lett., 1982. **41**(4): p. 379.
123. Burmeister, F., et al., *From mesoscopic to nanoscopic surface structures: Lithography with colloid monolayers.* Advanced Materials, 1998. **10**(6): p. 495-+.
124. Vinteler, E., *Disorder effects in reflectance spectra of colloida photonic crystals.* Nuclear Instruments & Methods in Physics Research Section B : beam interactions with materials and atoms, 2008. **267**(2): p. 393-396.
125. Danial, M.C., *Gold nanoparticles: Assembly, supramolecular chemistry, quantum-size-related properties, and applications toward biology, catalysis, and nanotechnology.* Chem. Rev., 2004. **104**: p. 293-346.
126. Brown, K.R., Natan, M. J., *Hydroxylamine seeding of colloidal Au nanoparticles in solution and on surfaces.* Langmuir,, 1998. **14**: p. 726-728.
127. Brown, K.R., Natan, M. J., *Seeding of colloidal Au nanoparticle solutions. 2. Improved control of particle size and shape.* Chem. Mater., 2000. **12**(306-313).
128. Meltzer, S., Will, P. , *Fabrication of nanostructures by hydroxylamine seeding of gold nanoparticles templates.* Langmuir,, 2001. **17**(1713-1718).
129. Wang, H., et al., *Controlled texturing modifies the surface topography and plasmonic properties of Au nanoshells.* Journal of Physical Chemistry B, 2005. **109**(22): p. 11083-7.
130. Tam, F., et al., *Mesoscopic nanoshells: geometry-dependent plasmon resonances beyond the quasistatic limit.* Journal of Chemical Physics, 2007. **127**(20): p. 204703.
131. Oldenburg, S.J., et al., *Light scattering from dipole and quadrupole nanoshell antennas.* Applied Physics Letters, 1999. **75**(8): p. 1063-1065.
132. Wang, H., et al., *Controlled texturing modifies the surface topography and plasmonic properties of au nanoshells.* Journal of Physical Chemistry B, 2005. **109**(22): p. 11083-11087.
133. Penninkhof, J.J., et al., *Optical cavity modes in gold shell colloids.* Journal of Applied Physics, 2008. **103**(12): p. -.
134. Kreibig, U., *optical absorption of small metallic particles.* surf. sci., 1985. **156**: p. 678.
135. Link, S. and M.A. El-Sayed, *Size and temperature dependence of the plasmon absorption of colloidal gold nanoparticles.* Journal of Physical Chemistry B, 1999. **103**(21): p. 4212-4217.

136. Mahmoud, M.A. and M.A. El-Sayed, *Aggregation of Gold Nanoframes Reduces, Rather Than Enhances, SERS Efficiency Due to the Trade-Off of the Inter- and Intraparticle Plasmonic Fields.* Nano Letters, 2009. **9**(8): p. 3025-3031.
137. Kang, C., Weiss, S. M., *Photonic Crystal Defects with Increased Surface Area for Improved Refractive Index Sensing.* Optical Society of America, 2010.
138. Weiss, S.M., Rong, G., *Nanoscale porous silicon waveguides for label-free DNA sensing.* Biosens. Bioelectron, 2008. **23**: p. 1572.
139. Wang, H., J. Kundu, and N.J. Halas, *Plasmonic nanoshell arrays combine surface-enhanced vibrational spectroscopies on a single substrate.* Angewandte Chemie-International Edition, 2007. **46**(47): p. 9040-9044.
140. Fromm, D.P., et al., *Gap-dependent optical coupling of single "Bowtie" nanoantennas resonant in the visible.* Nano Letters, 2004. **4**(5): p. 957-961.
141. SUN, Y., Xia, Y., *increased sensitivity of surface plasmon resonance of gold nanoshells compared to that of gold solid colloids in responce to enviromental changes.* Anal.Chem., 2002. **74**(20).
142. Hayashi, S., *spectroscopy of gap modes in metal particle-surface systems*, in *Near field optics and surface plasmon polaritons*, S. Kawata, Editor. 2001, springer-Verlag Berlin
143. Hao, E., G.C. Schatz, and J.T. Hupp, *Synthesis and optical properties of anisotropic metal nanoparticles.* Journal of Fluorescence, 2004. **14**(4): p. 331-341.
144. Rong, G., et al., *Nanoscale porous silicon waveguide for label-free DNA sensing.* Biosensors & Bioelectronics, 2008. **23**(10): p. 1572-1576.
145. Malinsky, M.D., et al., *Nanosphere lithography: Effect of substrate on the localized surface plasmon resonance spectrum of silver nanoparticles.* Journal of Physical Chemistry B, 2001. **105**(12): p. 2343-2350.
146. Novo, C., et al., *Influence of the medium refractive index on the optical properties of single gold triangular prisms on a substrate.* Journal of Physical Chemistry C, 2008. **112**(1): p. 3-7.
147. Ringe, E., et al., *Unraveling the Effects of Size, Composition, and Substrate on the Localized Surface Plasmon Resonance Frequencies of Gold and Silver Nanocubes: A Systematic Single-Particle Approach.* Journal of Physical Chemistry C, 2010. **114**(29): p. 12511-12516.
148. Decher, G., J.D. Hong, and J. Schmitt, *Buildup of Ultrathin Multilayer Films by a Self-Assembly Process .3. Consecutively Alternating Adsorption of Anionic and Cationic Polyelectrolytes on Charged Surfaces.* Thin Solid Films, 1992. **210**(1-2): p. 831-835.
149. Halthur, T.J. and U.M. Elofsson, *Multilayers of charged polypeptides as studied by in situ ellipsometry and quartz crystal microbalance with dissipation.* Langmuir, 2004. **20**(5): p. 1739-1745.
150. Dong, W.F., et al., *Controlled permeability in polyelectrolyte films via solvent treatment.* Chemistry of Materials, 2005. **17**(20): p. 4992-4999.

151. Keating, D.C., He, L., *the distance-dependence of colloidal Au-Amplified surface plasmon Resonance.* J. Phys. Chem. B, 2004. **108**: p. 10973-10980.
152. Oloomi, S.A.A., A. Saboonchi, and A. Sedaghat, *Effects of thin film thickness on emittance, reflectance and transmittance of nano scale multilayers.* International Journal of the Physical Sciences, 2010. **5**(5): p. 465-469.
153. Yu, X.L., et al., *A surface plasmon resonance imaging interferometry for protein micro-array detection.* Sensors and Actuators B-Chemical, 2005. **108**(1-2): p. 765-771.
154. Tam, F., et al., *Mesoscopic nanoshells: Geometry-dependent plasmon resonances beyond the quasistatic limit.* Journal of Chemical Physics, 2007. **127**(20): p. -.

Ich erkläre hiermit, daß ich die vorliegende Dissertation selbst verfasst und mich dabei keiner anderen als der von mir bezeichneten Quellen und Hilfsmittel bedient habe. Ich habe an keiner anderen Stelle ein Prüfungsverfahren beantragt bzw. die Dissertation in dieser oder anderer Form bereits anderweitig als Prüfungsarbeit verwendet oder einer anderen Fakultät als Dissertation vorgelegt.

Heidelberg , im Dezember